

PRODUCTION AND DECAY OF  $W_R$  GAUGE BOSONS IN  
LEFT-RIGHT SYMMETRIC MODELS AT THE  
TEVATRON AND THE LHC

ALPER HAYRETER

A THESIS  
IN  
THE DEPARTMENT  
OF  
PHYSICS

PRESENTED IN PARTIAL FULFILLMENT OF THE REQUIREMENTS  
FOR THE DEGREE OF DOCTOR OF PHILOSOPHY  
CONCORDIA UNIVERSITY  
MONTRÉAL, QUÉBEC, CANADA

DECEMBER 2011

© ALPER HAYRETER, 2012

**CONCORDIA UNIVERSITY  
SCHOOL OF GRADUATE STUDIES**

This is to certify that the thesis prepared

By: **Mr. Alper Hayreter**  
Entitled: **Production and Decay of  $W_R$  Gauge Bosons in Left-Right  
Symmetric Models at the Tevatron and the LHC**

and submitted in partial fulfillment of the requirements for the degree of

**DOCTOR OF PHILOSOPHY (Physics)**

complies with the regulations of the University and meets the accepted standards  
with respect to originality and quality.

Signed by the final examining committee:

_____	Chair
Dr. N. Howe	
_____	External Examiner
Dr. R.N. Mohapatra	
_____	External to Program
Dr. D. Korotkin	
_____	Examiner
Dr. S.K. Misra	
_____	Examiner
Dr. P. Vasilopoulos	
_____	Thesis Supervisor
Dr. M. Frank	

Approved by \_\_\_\_\_  
Dr. E. Diamantoudi, Graduate Program Director

December 2, 2011

\_\_\_\_\_  
Dr. B. Lewis, Dean, Faculty of Arts & Science

# Abstract

Production and Decay of  $W_R$  Gauge Bosons in Left-Right Symmetric Models at the Tevatron and the LHC

Alper Hayreter, Ph.D.

Concordia University, 2012

In this thesis we study the production and decays of  $W_R$  gauge bosons in several left-right symmetric models. We first use experimental constraints on the branching ratios of  $b \rightarrow s\gamma$ ,  $b \rightarrow ce\bar{\nu}_e$ , and  $B_{d,s}^0 - \bar{B}_{d,s}^0$  mixing to restrict the parameter space of the model. We then analyze the branching ratios of  $W_R$  and look for signals in  $pp \rightarrow W_R t \rightarrow t$  (*dijet*) and show that the LHC could find a significant resonance for new gauge bosons. Finally, we analyze the top pair production and forward-backward asymmetry, and show that while the cross section at the Tevatron and the LHC are in agreement with the predictions of the model, the asymmetry observed at the Tevatron is inconsistent with LR model predictions, while the small asymmetry observed at the LHC is compatible with the model.

to my wife İpek Hayreter,  
to my son (who has not a name yet),  
to my brother Özgür Hayreter,  
and to my parents Dilek and Engin Hayreter ...

# Acknowledgments

This Ph.D thesis is the result of three and a half years of hard working and studying under the inspiring supervision of Professor Mariana Frank at the Physics Department in Concordia University. I am extremely grateful to her for her understanding, kindness, support, patience and guidance during my Ph.D. Her brilliant supervision and continuous support helped me to finish my work on time. She was always more than a supervisor, there is a lot to say about her but in short she will always remain as a very special person in rest of my career and life.

I also would like to thank Assistant Professor İsmail Turan whom I was collaborating with during my Ph.D. I was inspired with his knowledge and enthusiasm in physics. Our discussions about physics were always fruitful and exciting. I have learned a lot from him about the computational aspects of our field. Besides being collaborators, I believe, I will always enjoy his friendship till the end of our lives.

All the faculty and staff members and my graduate friends at the Physics Department in Concordia University deserve many thanks too. I would like to thank all of them individually for providing a very friendly and effective research environment. I will always remember their welcoming and warm friendship.

Finally, I would like to express my gratitude to my lovely wife, to my brave brother, and to my loving parents for all their constant, endless moral support and love.

# Contents

<b>List of Figures</b>	<b>viii</b>
<b>List of Tables</b>	<b>xiii</b>
<b>List of Abbreviations</b>	<b>xiv</b>
<b>1 STANDARD MODEL</b>	<b>1</b>
1.1 Introduction . . . . .	1
1.2 Model Description . . . . .	2
1.3 Spontaneous Symmetry Breaking . . . . .	6
1.3.1 Mass Generation of Gauge Bosons . . . . .	8
1.3.2 Mass Generation of Fermions . . . . .	10
1.4 Electroweak Interactions . . . . .	12
1.4.1 Electromagnetic Interactions . . . . .	13
1.4.2 Neutral Current Weak Interactions . . . . .	14
1.4.3 Charged Current Weak Interactions . . . . .	15
1.5 Challenges in the Standard Model . . . . .	16
<b>2 LEFT-RIGHT SYMMETRIC MODEL</b>	<b>20</b>
2.1 Model Description . . . . .	20
2.2 Spontaneous Symmetry Breaking in the LRSM . . . . .	24
2.2.1 Generation of Gauge Boson Masses in the LRSM . . . . .	25
2.2.2 Generation of Fermion Masses in the LRSM . . . . .	29
2.3 Electroweak Interactions in the LRSM . . . . .	30
2.3.1 Electromagnetic Interactions in the LRSM . . . . .	30
2.3.2 Neutral Current Interactions in the LRSM . . . . .	31

2.3.3	Charged Current Interactions in the LRSM . . . . .	33
2.3.4	Right CKM Quark Mixing Matrix . . . . .	35
2.4	Higgs Sector in the LRSM . . . . .	36
<b>3</b>	<b>B DECAYS IN THE LRSM</b>	<b>38</b>
3.1	$b \rightarrow s\gamma$ Decay . . . . .	42
3.2	$B_{d,s}^0 - \bar{B}_{d,s}^0$ Mixing . . . . .	49
3.3	Summary . . . . .	58
<b>4</b>	<b>PRODUCTION AND DECAY OF <math>W_R</math> BOSON AT THE LHC</b>	<b>60</b>
4.1	Production and Decays . . . . .	62
4.2	Signal and Background for $W_R$ Production at the LHC . . . . .	68
4.3	Summary . . . . .	72
<b>5</b>	<b>TOP QUARK PAIR PRODUCTION AND ASYMMETRIES AT THE TEVATRON AND THE LHC IN THE LRSM</b>	<b>75</b>
5.1	$t\bar{t}$ Cross Section and Forward-Backward Asymmetries at the Tevatron	79
5.2	$t\bar{t}$ Cross Section and Forward-Central Charge Asymmetries at the LHC	87
5.3	Summary . . . . .	95
<b>6</b>	<b>CONCLUSION AND OUTLOOK</b>	<b>99</b>
<b>A</b>	<b>Notations and Conventions</b>	<b>102</b>
A-1	Spinors and Dirac Algebra . . . . .	102
A-2	Bidoublet-Triplet Conventions And Covariant Derivative . . . . .	104
<b>B</b>	<b>Feynman Rules in LRSM</b>	<b>106</b>
B-1	Fermion-Fermion-Gauge (FFV) . . . . .	106
B-2	Fermion-Fermion-Scalar (FFS) . . . . .	108
B-3	Gauge-Scalar-Scalar (VSS) . . . . .	109
B-4	Gauge-Gauge-Scalar (VVS) . . . . .	111
<b>C</b>	<b>QCD Correction Factors for <math>B_{d,s}^0 - \bar{B}_{d,s}^0</math> Mixing</b>	<b>113</b>
<b>D</b>	<b>4-point Passarino-Veltman Integrals</b>	<b>114</b>
	<b>Bibliography</b>	<b>120</b>

# List of Figures

1	Energy configuration of Higgs field on real-imaginary plane. . . . .	7
2	Feynman diagram of electromagnetic interactions in the SM. . . . .	13
3	Feynman diagram of neutral current interactions in the SM. . . . .	14
4	Feynman diagram of leptons charged current interactions in the SM. . . . .	15
5	Feynman diagram of quarks charged current interactions in the SM. . . . .	16
6	Feynman diagram of electromagnetic interactions in the LRSM. . . . .	31
7	Feynman diagrams of neutral current interactions in the LRSM. . . . .	33
8	Feynman diagrams of leptons charged current interactions in the LRSM. . . . .	34
9	Feynman diagrams of quarks charged current interactions in the LRSM. . . . .	35
10	Triangle and self-energy diagrams contributing to the $b \rightarrow s\gamma$ transition. . . . .	43
11	Contour plot of the $M_{W_2}$ vs $\sin \alpha$ constraint in the $U_A$ parametrization, from $b \rightarrow s\gamma$ . We fix the $\text{BR}(b \rightarrow s\gamma)$ to be in the interval $(3.20 - 3.85) \times 10^{-4}$ , and vary $g_{RL}$ and $\tan \beta$ , as indicated in the panels. We take $M_{H^\pm} = 10$ TeV. Black-shaded regions represent areas excluded by the $W_R - W_L$ mixing angle $\xi \leq 3 \times 10^{-3}$ . Regions highlighted in yellow represent allowed parameter spaces. . . . .	45
12	$\text{BR}(b \rightarrow s\gamma)$ as a function of the $W_2$ mass in the MLRSM, $V_{CKM}^R = V_{CKM}^L$ . We take $\tan \beta = 10$ in the left panel and $\tan \beta = 60$ in the right panel. The curves in red, green and blue correspond to, respectively $M_{H^\pm} = 1, 5$ and $50$ TeV. Yellow highlighted regions represent allowed spaces; the black shaded region is excluded by the $W_L - W_R$ mixing angle. . . . .	47



- 13 Contour plot of the  $M_{H^\pm}$  vs  $\tan\beta$  constraint in the  $U_A$  parametrization, for  $b \rightarrow s\gamma$ . We fix the branching ratio to be in the interval  $(3.20 - 3.85) \times 10^{-4}$ , and vary  $g_{RL}$  and  $\sin\alpha$ , as indicated in the panels. We take  $M_{W_2} = 500$  GeV. Shaded regions represent areas excluded by the  $W_R - W_L$  mixing angle  $\xi \leq 3 \times 10^{-3}$ . Regions highlighted in yellow represent allowed parameter spaces. . . . . 48
- 14 Box diagrams contributing to  $B^0 - \bar{B}^0$  transition. Here  $q = d$  for  $B_d^0 - \bar{B}_d^0$  and  $q = s$  for  $B_s^0 - \bar{B}_s^0$  mixing;  $u_{m,n}$  represent up-type quarks and are summed over. . . . . 52
- 15 Contour plot of the  $M_{W_2}$  vs  $\sin\alpha$  constraint in the  $U_B$  parametrization, for the  $B_d^0 - \bar{B}_d^0$  mass difference. We fix  $\Delta M_d$  mass difference to be in the interval  $(0.43 - 0.58) ps^{-1}$  (represented by blue and red curves, respectively) and vary  $g_{RL}$ , as indicated in the panels. We take  $M_{H^\pm} = 10$  TeV in upper panels and  $M_{H^\pm} = 20$  TeV in lower panels and  $\tan\beta = 10$ . Regions shaded are restricted by the  $W_L - W_R$  mixing angle  $\xi \leq 3 \times 10^{-3}$ . Regions highlighted in yellow represent the allowed parameter spaces. . . . . 53
- 16 Contour plot of the  $M_{W_2}$  vs  $\sin\alpha$  constraint in the  $U_A$  parametrization, for the  $B_s^0 - \bar{B}_s^0$  mass difference. We fix  $\Delta m_s$  mass difference to be in the interval  $(15 - 20) ps^{-1}$  (represented by blue and red curves, respectively) and vary  $g_{RL}$ , as indicated in the panels. We take  $M_{H^\pm} = 10$  TeV in upper panels and  $M_{H^\pm} = 20$  TeV in lower panels, and  $\tan\beta = 10$  throughout. Regions shaded are restricted by the  $W_L - W_R$  mixing angle  $\xi \leq 3 \times 10^{-3}$ . Regions highlighted in yellow represent the allowed parameter spaces. . . . . 55
- 17  $\Delta M_{d,s}$  dependence on the charged Higgs mass  $M_{H^\pm}$ . We fix  $\tan\beta = 10$  and show curves for negative and positive values of  $\sin\alpha$ , in red and blue respectively, chosen in each panel to fit within the experimental range. The yellow highlighted regions represent allowed parameter regions between  $\Delta M_d = (0.43 - 0.58) ps^{-1}$  and  $\Delta M_s = (15 - 20) ps^{-1}$ . 56

18	$\Delta M_{d,s}$ dependence on the $W_2$ mass in MLRSM for $M_{H^\pm} = 0.5, 1, 5$ and 50 TeV. We show $\Delta M_d$ in the upper panels, and $\Delta M_s$ in the lower ones. The left row corresponds to $\tan\beta = 10$ , the right one to $\tan\beta = 60$ . Regions shaded are restricted by the $W_L - W_R$ mixing angle $\xi \leq 3 \times 10^{-3}$ . Regions highlighted in yellow represent the allowed parameter spaces. . . . .	57
19	Feynman diagrams of the $W_R$ -top associated production at the LHC.	63
20	$W_R$ production cross-section as a function of the $W_R$ mass (upper panels) and RCKM matrix parameter $\sin\alpha$ (lower panels), for the three models described in the text ( $U_A$ , $U_B$ and MLRSM). . . . .	63
21	Contour plot of $M_{W_R}$ vs $\sin\alpha$ . The upper row is for the $U_A$ parametrization in which the $W_R$ production cross-sections are constrained by both $b \rightarrow s\gamma$ and $B_s^0 - \bar{B}_s^0$ processes. Dark-gray shaded regions are excluded from $b \rightarrow s\gamma$ and light-gray shaded regions from $B_s^0 - \bar{B}_s^0$ . Black shaded region indicates the exclusion by L-R mixing angle violation ( $\xi < 3 \times 10^{-3}$ ). The lower row is for the $U_B$ parametrization where only $B_d^0 - \bar{B}_d^0$ mixing constrains the production cross-section. In both parametrizations we take $M_{H^+} = 20$ TeV and $\tan\beta = 30$ . . . . .	65
22	Branching ratios of $W_R$ decays as functions of $\sin\alpha$ (upper panels) and $W_R$ mass (lower panels). The $W_R$ mass is fixed at 750 GeV in the top left and 1500 GeV in the top right panel, while $\sin\alpha$ is fixed to 0.1 in the bottom left panel and 0.9 in right one. . . . .	66
23	Branching ratios of $W_R$ decays as functions of the $W_R$ mass in the MLRSM. . . . .	67
24	Differential cross section for the <i>dijet</i> mass spectrum for $W_R$ decays in the $U_A$ , $U_B$ parametrizations and in the MLRSM, compared to the SM background and the CDF data. It is possible to show that the SM curve agrees very well with the CDF Run II data after including NLO perturbative QCD corrections. Our SM curve should be taken as a rough estimation. . . . .	69
25	The signal $pp \rightarrow t W_R \rightarrow t(\text{jet jet})$ . . . . .	69

26	<p><math>W_R</math> signal as a resonance in <i>dijet</i> mass distribution at the LHC (<math>\sqrt{s} = 14</math> TeV) with <math>U_A</math> (left column) and <math>U_B</math> (right column) RCKM parametrizations. The signal is observed in <math>p, p \rightarrow t, dijet</math> process where only the light quarks are counted as jets. We choose <math>binsize = 20</math> GeV for intermediate <math>M_{W_R} = 1500</math> GeV and <math>binsize = 10</math> GeV for light <math>M_{W_R} = 750</math> GeV. . . . .</p>	71
27	<p>The resonance <math>W_R</math> signal in the LHC (<math>\sqrt{s} = 14</math> TeV) with Manifest model. The intermediate <math>W_R</math> (on left panel) and light <math>W_R</math> (on right panel) signals are presented. Again the same <math>binsize</math> choice with Figure 26. . . . .</p>	72
28	<p><math>t\bar{t}</math> invariant mass distribution of differential cross section in Manifest LR model (upper panel), Model A (lower left panel) and Model B (lower right panel) in comparison with CDF II <math>5.3 \text{ fb}^{-1}</math> data. The parameter sets (Set I, Set II and Unconstrained Set) for each model are given in Table 4. . . . .</p>	82
29	<p><math>t\bar{t}</math> production and decay topology in hadronic and semileptonic events. <math>V_\mu^0</math> represents neutral gauge bosons <math>\gamma, g, Z, Z_R</math> and <math>V_\mu^\pm</math> the charged ones, <math>W_L^\pm, W_R^\pm</math>. The diagram with the top quark decaying hadronically is shown but both possibilities are included. . . . .</p>	83
30	<p><math>\Delta_y</math>(upper row) and <math>y_t</math>(lower row) distributions in Manifest LR model (left panel), Model A (middle panel) and Model B (right panel) at the Tevatron. Parameter sets (Set I, Set II and Unconstrained) for each model are given in the Table 4. . . . .</p>	86
31	<p><math>t\bar{t}</math> invariant mass distributions at the Tevatron in Manifest LR model (left panel), Model A (middle panel) and Model B (right panel) in comparison with the SM. Parameter sets (Set I, Set II and Unconstrained) of each model are given in the Table 4. . . . .</p>	87
32	<p>Events in the <math>t\bar{t}</math> invariant mass distributions at LHC in MLRSM (left panel), Model A (middle panel) and Model B (right panel) in comparison with the SM. Top row shows the distribution for <math>\sqrt{s} = 7</math> TeV, the bottom row is for <math>\sqrt{s} = 14</math> TeV. Parameter sets (Set I, Set II and Unconstrained) for each model are given in the Table 4. . . . .</p>	91

33	Top (upper row) and anti-top (lower row) rapidity distributions in Manifest LR model (left panel), Model A (middle panel) and Model B (right panel) at LHC ( $\sqrt{s} = 7$ TeV). The parameter sets (Set I, Set II and Unconstrained) for each model are given in Table 4. . . . .	94
34	Top (upper row) and anti-top (lower row) rapidity distributions in Manifest LR model (left panel), Model A (middle panel) and Model B (right panel) at LHC ( $\sqrt{s} = 14$ TeV). The parameter sets (Set I, Set II and Unconstrained) for each model are given in Table 4. . . . .	95
35	Momentum and mass conventions used in the Passarino-Veltman for evaluating the box diagrams. . . . .	114

# List of Tables

1	Field content of the Standard Model and respective quantum numbers in $SU(3)_C \times SU(2)_L \times U(1)_Y$ gauge structure. . . . .	4
2	Field content of the LRSM and respective quantum numbers in $SU(2)_L \times SU(2)_R \times U(1)_{B-L}$ gauge structure. . . . .	21
3	Bag-parameter values taken from lattice-improved calculations in the RI-MOM renormalization scheme [1], with the running quark masses $M_b(M_b) = 4.5$ GeV and $M_d(M_b) = 5.4$ MeV. Notice that we took $B_6 = 1$ for both cases since the bag parameters for the relevant operator is not known yet. . . . .	51
4	Benchmark points Set I, Set II and Unconstrained for left-right symmetric models: Manifest, Model A, and Model B, used throughout the analysis. Note that $M_{Z_R}$ is fixed when a value for $M_{W_R}$ is chosen but the $M_{Z_R}$ values are included for reference. . . . .	79
5	The NNLO $t\bar{t}$ production cross-sections at the Tevatron ( $\sqrt{s} = 1.96$ TeV) for the SM, and Left-Right models: Manifest, Model A and Model B, for the benchmark points chosen. . . . .	80
6	The Forward-Backward Asymmetry at the Tevatron in the SM, and in LR models: Manifest, Model A and Model B, compared with the CDF data. We include, in the first two rows, the unfolded CDF results and the MCFM calculation. Parameter sets (Set I, Set II and Unconstrained) for each model are given in the Table 4. . . . .	85
7	$t\bar{t}$ production cross-sections at the LHC for both $\sqrt{s} = 7$ TeV and $\sqrt{s} = 14$ TeV. . . . .	90
8	Forward and Central Charge Asymmetries at LHC. Parameter sets (Set I, Set II and Unconstrained) for each model are given in Table 4. . . . .	93
9	The QCD correction parameters $\eta_i(m_b)$ used in (3.21). . . . .	113

# List of Abbreviations

$\overline{MS}$	Modified Minimal Subtraction
$A_{FB}$	Forward-Backward Asymmetry
ALRM	Asymmetric Left-Right Symmetry
ATLAS	A Toroidal LHC Apparatus
BNL	Berkeley National Laboratory
BR	Branching Ratio
BSM	Beyond the Standard Model
CC	Charged Current Interactions
CDF	Collider Detector at Fermilab
CERN	Conseil Européen pour la Recherche Nucléaire
CKM	Cabbibo- Kobayashi-Maskawa Matrix
CMS	Compact Muon Solenoid
CP	Charge-Parity
DØ	DZero Experiment
EM	Electromagnetic Interactions
fb	Femtobarn
FCNC	Flavor-Changing Neutral Current

FNAL	Fermi National Accelerator Laboratory
GeV	Giga Electron Volt
KEKB	A Particle Accelerator in Belle Experiment
KK	Kaluza-Klein
LEP	Large Electron-Positron Collider
LHC	Large Hadron Collider
LHCb	Large Hadron Collider beauty
LO	Leading Order
LR	Left-Right
LRSM	Left-Right Symmetric Model
MeV	Mega Electron Volt
MLRSM	Manifest Left-Right Symmetric Model
NC	Neutral Current Interactions
NLO	Next-to-Leading Order
NNLO	Next-to-next-to Leading Order
NP	New Physics
OPE	Operator Product Expansion
pb	Picobarn
PDF	Parton Distribution Function
ps	Pico Second
QCD	Quantum Chromo Dynamics
RCKM	Right CKM quark mixing matrix

RG	Renormalization Group
RI-MOM	Regularization Invariant Momentum Subtraction
RS	Randall-Sundrum
SLAC	Stanford Linear Accelerator Center
SM	Standard Model
SSB	Spontaneous Symmetry Breaking
TeV	Tera Electron Volt
UED	Universal Extra Dimensions
VEV	Vacuum Expectation Value



# Chapter 1

## STANDARD MODEL

### 1.1 Introduction

We are living particularly exciting times right now. High Energy Physics, which attempts to provide a cohesive picture of the fundamental forces and particles governing the structure of matter is less than a century old. During this time, it has been extremely successful in explaining some of the basic underlying laws of nature. The crowning glory is the Standard Model (SM) of elementary particles, which encapsulates some of our knowledge of the field. Most of the particles and interactions it predicts have already been confirmed experimentally. Perhaps the only piece missing is the Higgs Boson, responsible for giving masses to fundamental particles and for electroweak symmetry breaking.

However the experimental success of the Standard Model is slightly overshadowed by its limitations. The model suffers from some theoretical inconsistencies, and cannot be a complete picture at higher energies. But the Large Hadron Collider (LHC) , the most ambitious project ever in experimental physics, is in the process of finding the last missing piece of the SM, and give some indications of what lies beyond it. In fact, even as I write this, the blogs are full of expectations that finding the Higgs is only weeks of data analysis away.

The theorists have been waiting with particular excitement to the findings of the LHC, but not while being idle. Many scenarios of physics Beyond the Standard Model (BSM) have been proposed, and many papers produced, which describe signatures that various models will have at the LHC. Supersymmetry (a theory proposing a

symmetry between bosons and fermions) remains the favorite model; yet the LHC has so far failed to see any signals for low-lying supersymmetric particles. A symmetry which treats left- and right-handed particles and interactions on an equal footing is perhaps the simplest extension of the SM. In this thesis I analyze a definitive signal for left-right models: a right-handed charged vector boson, the right-handed equivalent of the charged  $W_L$  vector boson in the SM. I concentrate on restrictions on the parameter space of the model, as well as characteristic signatures of production and decays of the boson, complete with simulation of signals which experiments at the LHC would see.

Finally, I investigate whether signals which have been observed already at a precursor of the LHC, the Tevatron experiment at Fermilab, which cannot be explained within the Standard Model, could be accommodated in the left-right models. Thus this thesis is a contribution to possible signals of BSM physics at hadron colliders, and in particular at the LHC.

## 1.2 Model Description

The SM of particle physics is an elegant description of elementary particles and their interactions at low energies. Incorporating three of the four fundamental interactions of nature and precisely explaining the dynamics of all experimentally known subatomic particles, the SM is an extremely successful theoretical framework. It covers three generations of leptons and quarks as elementary particles, electron ( $e$ ), muon ( $\mu$ ) and tau ( $\tau$ ) lepton with their associated neutrinos ( $\nu$ ) in the lepton sector and up ( $u$ ), down ( $d$ ), charm ( $c$ ), strange ( $s$ ), top ( $t$ ) and bottom ( $b$ ) quarks in the quark sector. Having half-integer spin ( $s = 1/2$ ) all the leptons and quarks obey to Fermi-Dirac statistics and therefore they are called *fermions*. Besides gravity, which appears to be the first handicap of the SM, all fundamental forces of nature are described by the exchange of force-carrier particles, that is, the photon ( $\gamma$ ) is responsible for electromagnetic interactions, weak forces are transmitted by  $Z^0, W^\pm$  and gluons ( $g$ ) mediate the strong forces. Since all these force-carrier particles have integer spin ( $s = 1$ ) they obey Bose-Einstein statistics thus called as *bosons*.

The SM is based on a gauge principle in which the exchanged bosons are gauge fields of corresponding symmetry groups. Concerning electromagnetic, weak and

strong interactions, the symmetry structure of the SM is

$$SU(3)_C \times SU(2)_L \times U(1)_Y \quad (1.1)$$

where all gauge bosons are related with the number of generators of the corresponding gauge group. There are 8 gluons  $G_\mu^a$  of  $SU(3)_C$  color (associated with  $3^2 - 1 = 8$  generators), 3 weak bosons  $W_\mu^i$  of  $SU(2)_L$  isospin (associated with  $2^2 - 1 = 3$  generators) and  $B_\mu$  boson of  $U(1)_Y$  hypercharge (associated with a single generator). The gauge structure of the SM is chiral sensitive, that is, it exhibits a built-in left-right asymmetry which means that left-handed and right-handed components of fermion fields are treated in a completely different manner. Having  $\pm 1/2$  weak isospin quantum numbers the left-handed fermion fields reside in doublet structure whereas the right-handed fermion fields take place in a singlet structure with no weak isospin quantum numbers at all. The field content of the SM and the quantum numbers are given in Table 1.

At high energies the gauge bosons of corresponding symmetry groups are mathematically seen to be virtual massless fields, however at low energies the spontaneous breaking of symmetries

$$SU(3)_C \times SU(2)_L \times U(1)_Y \longrightarrow SU(3)_C \times U(1)_{EM} \quad (1.2)$$

gives rise to physical massive gauge bosons i.e. neutral  $Z^0$  and charged  $W^\pm$  bosons. This symmetry breaking at low energies relates the corresponding quantum number electromagnetic charge (Q) of the  $U(1)_{EM}$  gauge group with the weak isospin ( $T$ ) of the  $SU(2)_L$  group and the hypercharge ( $Y$ ) of  $U(1)_Y$ . This relation is formulated in the so called Gell-Mann-Nishijima formula

$$Q = T + \frac{Y}{2} \quad (1.3)$$

The interactions and dynamics of SM fields are prescribed by the Lagrangian density

$$\mathcal{L} = \mathcal{L}_{Gauge} + \mathcal{L}_{Kinetic} + \mathcal{L}_{Higgs} + \mathcal{L}_{Yukawa} \quad , \quad (1.4)$$

where each term respectively refers to the Gauge, Kinetic, Higgs, and Yukawa sectors of the theory.

Fields	Components	$SU(3)_C \times SU(2)_L \times U(1)_Y$		
<b>Fermions</b>				
$L$	$\begin{bmatrix} \nu \\ e \end{bmatrix}_L$	1	2	-1
$E$	$e_R^c$	1	1	+2
$Q$	$\begin{bmatrix} u \\ d \end{bmatrix}_L$	3	2	$+\frac{1}{3}$
$U$	$u_R^c$	$\bar{3}$	1	$-\frac{4}{3}$
$D$	$d_R^c$	$\bar{3}$	1	$+\frac{2}{3}$
<b>Gauge bosons</b>				
$B_\mu$	$B_\mu^0$	1	1	0
$W_\mu$	$W_\mu^+, W_\mu^-, W_\mu^0$	1	3	0
$G_\mu$	$G_\mu^a (a = 1\dots 8)$	8	1	0
<b>Higgs</b>				
$\Phi$	$\begin{bmatrix} \phi^+ \\ \phi^0 \end{bmatrix}$	1	2	+1

Table 1: Field content of the Standard Model and respective quantum numbers in  $SU(3)_C \times SU(2)_L \times U(1)_Y$  gauge structure.

The Gauge Lagrangian density includes the interactions of gauge fields by means of field strength tensors

$$\begin{aligned}
\mathcal{L}_{Gauge} &= -\frac{1}{4} \sum F_{\mu\nu} F^{\mu\nu} , \\
\mathcal{L}_{Gauge} &= -\frac{1}{4} G_{\mu\nu}^a G^{\mu\nu a} - \frac{1}{4} W_{\mu\nu}^i W^{\mu\nu i} - \frac{1}{4} B_{\mu\nu} B^{\mu\nu} , \tag{1.5}
\end{aligned}$$

where the field strength tensors for  $SU(3)_C, SU(2)_L$  and  $U(1)_Y$  are, respectively,

$$\begin{aligned}
G_{\mu\nu}^a &= \partial_\mu G_\nu^a - \partial_\nu G_\mu^a - g_s f_{abc} G_\mu^b G_\nu^c \quad , \quad a, b, c = 1 \dots 8 \quad , \\
W_{\mu\nu}^i &= \partial_\mu W_\nu^i - \partial_\nu W_\mu^i - g_L \epsilon_{ijk} W_\mu^j W_\nu^k \quad , \quad i, j, k = 1 \dots 3 \quad , \\
B_{\mu\nu} &= \partial_\mu B_\nu - \partial_\nu B_\mu \quad ,
\end{aligned} \tag{1.6}$$

$g_s$  and  $g_L$  are gauge coupling constants,  $f_{abc}$  and  $\epsilon_{ijk}$  are generators in the adjoint representation of  $SU(3)_C$  and  $SU(2)_L$  respectively. These terms contain the gauge boson kinetic interactions as well as the three- and four-point self interactions of the  $G_\mu^a$  and  $W_\mu^i$  gauge fields.

The gauge-covariant kinetic interactions of fermions with gauge fields are encoded in the Kinetic Lagrangian density

$$\begin{aligned}
\mathcal{L}_{Kinetic} &= i \sum \bar{\psi} \gamma^\mu D_\mu \psi \quad , \\
\mathcal{L}_{Kinetic} &= i \sum_{j=1}^3 \left( \bar{L}_j \gamma^\mu D_\mu L_j + \bar{E}_j \gamma^\mu D_\mu E_j \right. \\
&\quad \left. + \bar{Q}_j \gamma^\mu D_\mu Q_j + \bar{U}_j \gamma^\mu D_\mu U_j + \bar{D}_j \gamma^\mu D_\mu D_j \right) \quad ,
\end{aligned} \tag{1.7}$$

in which the covariant derivative ( $D_\mu$ ) takes the following forms for each term

$$\bar{L} \gamma^\mu D_\mu L = \bar{L} \gamma^\mu \left( \partial_\mu - \frac{ig_L}{2} \sigma \cdot W_\mu + \frac{ig_Y}{2} B_\mu \right) L \quad , \tag{1.8}$$

$$\bar{E} \gamma^\mu D_\mu E = \bar{E} \gamma^\mu \left( \partial_\mu - ig_Y B_\mu \right) E \quad , \tag{1.9}$$

$$\bar{Q}^\alpha \gamma^\mu D_\mu Q^\beta = \bar{Q}^\alpha \gamma^\mu \left[ \left( \partial_\mu - \frac{ig_L}{2} \sigma \cdot W_\mu - \frac{ig_Y}{6} B_\mu \right) \delta_{\alpha\beta} - \frac{ig_s}{2} \lambda_{\alpha\beta} \cdot G_\mu \right] Q^\beta \quad , \tag{1.10}$$

$$\bar{U}^\alpha \gamma^\mu D_\mu U^\beta = \bar{U}^\alpha \gamma^\mu \left[ \left( \partial_\mu + \frac{2ig_Y}{3} B_\mu \right) \delta_{\alpha\beta} - \frac{ig_s}{2} \lambda_{\alpha\beta} \cdot G_\mu \right] U^\beta \quad , \tag{1.11}$$

$$\bar{D}^\alpha \gamma^\mu D_\mu D^\beta = \bar{D}^\alpha \gamma^\mu \left[ \left( \partial_\mu - \frac{ig_Y}{3} B_\mu \right) \delta_{\alpha\beta} - \frac{ig_s}{2} \lambda_{\alpha\beta} \cdot G_\mu \right] D^\beta \quad . \tag{1.12}$$

where  $\alpha$  and  $\beta$  are color indices for quarks,  $\sigma$  and  $\lambda_{\alpha\beta}$  are the  $2 \times 2$  Pauli spin and  $3 \times 3$  Gel-Mann matrices, respectively (generators of  $SU(2)_L$  and  $SU(3)_C$  in fundamental representation).

The scalar Higgs part of the Lagrangian density is

$$\mathcal{L}_{Higgs} = (D^\mu \phi)^\dagger D_\mu \phi - V(\phi) \quad , \tag{1.13}$$

where  $\phi$  is a complex scalar Higgs field and the covariant derivative reads

$$D_\mu \phi = \left( \partial_\mu - \frac{ig_L}{2} \sigma \cdot W_\mu - \frac{ig_Y}{2} B_\mu \right) \phi . \quad (1.14)$$

The square of covariant derivative leads to three and four-point interaction terms between the gauge and Higgs fields. The Higgs potential  $V(\phi)$  is restricted by the renormalizability and the invariance of  $SU(2) \times U(1)$  to the form

$$V(\phi) = \mu^2 \phi^\dagger \phi + \lambda (\phi^\dagger \phi)^2 . \quad (1.15)$$

For  $\mu^2 < 0$  the spontaneous symmetry breaking occurs and the non-zero vacuum expectation value (VEV) of  $\langle 0 | \phi^0 | 0 \rangle$  generates masses for  $W$  and  $Z$  bosons.

The Lagrangian density of the Yukawa sector is

$$\begin{aligned} \mathcal{L}_{Yukawa} &= - \sum y \bar{\psi}_L \phi \psi_R \\ \mathcal{L}_{Yukawa} &= - \sum_{i,j=1}^3 (y_{ij}^e \bar{L}_i \phi E_j + y_{ij}^u \bar{Q}_i \phi^c U_j + y_{ij}^d \bar{Q}_i \phi D_j) + h.c. , \end{aligned} \quad (1.16)$$

where  $y_{ij}^e$ ,  $y_{ij}^u$ ,  $y_{ij}^d$  are  $3 \times 3$  Yukawa matrices, which ultimately determine the fermion masses and mixings, and the charge conjugate of the Higgs field is

$$\phi^c = i\sigma^2 \phi^\dagger \equiv \begin{pmatrix} \phi^{0\dagger} \\ -\phi^- \end{pmatrix} . \quad (1.17)$$

These terms represent the Yukawa couplings between Higgs fields and fermions, which are necessary to generate fermion masses by the spontaneous breaking of the chiral symmetries.

### 1.3 Spontaneous Symmetry Breaking

Gauge theories do not allow bare mass terms for gauge bosons because they would break the gauge invariance and destroy the renormalizability of the theory. Without Spontaneous Symmetry Breaking (SSB), the SM predicts the existence of a number of massless particles which is actually not realistic. In reality, most of the fermions and some of the gauge bosons are real massive particles. To overcome this ambiguity, the Higgs mechanism which triggers the SSB is introduced. The Higgs field is defined

as a two-component complex  $SU(2)$  spinor in order to properly interact with weak gauge bosons in the  $SU(2)_L \times U(1)_Y$  sector;

$$\phi = \begin{pmatrix} \phi^+ \\ \phi^0 \end{pmatrix} = \frac{1}{\sqrt{2}} \begin{pmatrix} \phi_C + i\phi_D \\ \phi_A + i\phi_B \end{pmatrix} . \quad (1.18)$$

The minimum of the Higgs potential, Equation (1.15), occurs at  $\langle \phi \rangle = \frac{v}{\sqrt{2}}$  instead of  $\langle \phi \rangle = 0$  which is a local maximum of the potential, thus at the vacuum, i.e. at the minimum energy configuration, having a non-zero VEV, the Higgs field spans the space-time as a fluctuating background field.

$$\langle 0|\phi|0 \rangle = \langle \phi \rangle = \frac{1}{\sqrt{2}} \begin{pmatrix} 0 \\ v \end{pmatrix} \quad \text{with} \quad v = \sqrt{\frac{-\mu^2}{\lambda}} . \quad (1.19)$$

At high energies, above the electroweak scale ( $\sim 100$  GeV), the Higgs field resides on top of the local maximum ( $v = 0$ ) and preserves the symmetry of the system. However, when the energy falls below the electroweak scale the  $v = 0$  point becomes unstable and the Higgs field cannot stay on top of the local maximum anymore. Choosing an arbitrary direction it falls into the minimum energy configuration thus spontaneously breaks the electroweak symmetry  $SU(2)_L \times U(1)_Y$  to the electromagnetism  $U(1)_{EM}$  and in consequence generates masses for the gauge bosons and the chiral fermions. The energy configuration of the Higgs field is pictured in Figure 1.

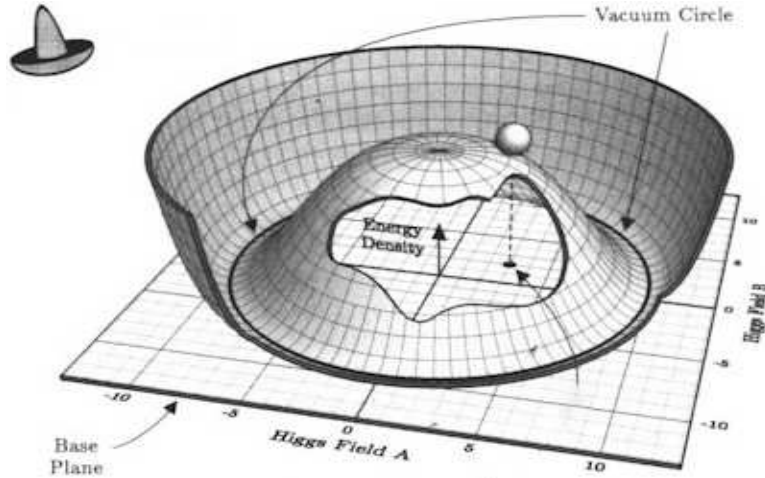


Figure 1: Energy configuration of Higgs field on real-imaginary plane.

Theories with SSB imply massless Goldstone bosons. In fact the SSB of the underlying local symmetry triggers conversion of the components of the scalar Higgs

field to Goldstone bosons. Instead of existing as a massless scalar particle, the degree of freedom carried by the Goldstone bosons manifests itself as the longitudinal spin component of a gauge boson which interacts with the other fields in the theory and produce mass terms for the gauge bosons (it is also said that the Goldstone boson has been eaten by the gauge boson). In the choice of unitary gauge, the scalar Higgs field is transformed into a basis in which Goldstone components are set to zero and can be expanded around the vacuum in terms of physical components,

$$\langle 0|\phi|0\rangle = \langle\phi\rangle = \frac{1}{\sqrt{2}} \begin{pmatrix} 0 \\ v + H \end{pmatrix}, \quad (1.20)$$

where  $H$  is a Hermitian scalar field, the physical Higgs boson.

### 1.3.1 Mass Generation of Gauge Bosons

Gauge fields acquire their masses kinetically interacting with the Higgs scalar. Therefore they arise from the kinetic part of the Higgs Lagrangian

$$|D_\mu\phi|^2 = \left| \left( \partial_\mu - \frac{ig_L}{2}\sigma \cdot W_\mu - \frac{ig_Y}{2}B_\mu \right) \phi \right|^2, \quad (1.21)$$

and the  $SU(2)$  part of the covariant derivative can be written as

$$\sigma \cdot W_\mu = \sigma^1 W_\mu^1 + \sigma^2 W_\mu^2 + \sigma^3 W_\mu^3 = \begin{pmatrix} W_\mu^3 & \sqrt{2}W_\mu^+ \\ \sqrt{2}W_\mu^- & -W_\mu^3 \end{pmatrix}, \quad (1.22)$$

where complex charged gauge bosons  $W_\mu^\pm$  mediate the charged current interactions

$$W_\mu^\pm = \frac{W_\mu^1 \mp iW_\mu^2}{\sqrt{2}}. \quad (1.23)$$

We obtain

$$\frac{g_L^2 v^2}{4} W^{\mu+} W_\mu^- + \frac{v^2}{8} (g_L W^{\mu 3} - g_Y B^\mu)(g_L W_\mu^3 - g_Y B_\mu). \quad (1.24)$$

the mixing of neutral fields ( $W_\mu^3$  and  $B_\mu$ ) can be removed by an orthogonal transformation

$$\begin{pmatrix} Z_\mu \\ A_\mu \end{pmatrix} = \begin{pmatrix} \cos\theta_W & -\sin\theta_W \\ \sin\theta_W & \cos\theta_W \end{pmatrix} \begin{pmatrix} W_\mu^3 \\ B_\mu \end{pmatrix} \quad (1.25)$$



where the  $\theta_W$  is the Weinberg angle which is responsible for the mixing

$$\cos \theta_W = \frac{g_L}{\sqrt{g_L^2 + g_Y^2}} \quad , \quad \sin \theta_W = \frac{g_Y}{\sqrt{g_L^2 + g_Y^2}} \quad , \quad (1.26)$$

then the compositions of physical neutral gauge bosons become

$$Z_\mu = \frac{g_L W_\mu^3 - g_Y B_\mu}{\sqrt{g_L^2 + g_Y^2}} \quad \text{and} \quad A_\mu = \frac{g_Y W_\mu^3 + g_L B_\mu}{\sqrt{g_L^2 + g_Y^2}} \quad , \quad (1.27)$$

they are responsible for neutral current and electromagnetic interactions respectively. With all these physical states of gauge fields, the kinetic part of the Higgs Lagrangian in vacuum takes the following form

$$\frac{g_L^2 v^2}{4} W^{\mu+} W_\mu^- + \frac{1}{2} \frac{(g_L^2 + g_Y^2) v^2}{4} Z^\mu Z_\mu + 0 A^\mu A_\mu \quad (1.28)$$

and the tree level physical masses of gauge bosons are predicted to be

$$M_W = \frac{g_L v}{2} \quad , \quad M_Z = \frac{g v}{2} = \frac{M_W}{\cos \theta_W} \quad , \quad M_A = 0 \quad , \quad (1.29)$$

where  $g = \sqrt{g_L^2 + g_Y^2}$  and the photon ( $A_\mu$ ) remains massless. The masses of  $W^\pm$  and  $Z$  bosons are roughly calculated to be  $M_W \sim 78$  GeV and  $M_Z \sim 89$  GeV. These predictions are increased by  $\sim 2$  GeV with loop corrections which at the end come to a complete agreement with their observed masses

$$M_W = 80.398 \pm 0.025 \text{ GeV} \quad , \quad M_Z = 91.1876 \pm 0.0021 \text{ GeV} \quad , \quad (1.30)$$

and the weak scale  $v$  is therefore evaluated as

$$v = \frac{2M_W}{g_L} \simeq 246 \text{ GeV} \quad . \quad (1.31)$$

In the unitary gauge the Higgs potential Equation (1.15) becomes

$$V(\phi) \rightarrow -\frac{\mu^4}{4\lambda} - \mu^2 H^2 + \lambda v H^3 + \frac{\lambda}{4} H^4 \quad , \quad (1.32)$$

the second term in the potential represents a tree-level mass for the Higgs boson

$$M_H = \sqrt{-2\mu^2} = v\sqrt{2\lambda} \quad , \quad (1.33)$$

the weak scale  $v$  is known but the quartic Higgs coupling  $\lambda$  is not. This puts a mystery on the Higgs mass, however there is a lower limit from LEP experiments  $M_H \gtrsim 114$  GeV.

### 1.3.2 Mass Generation of Fermions

Three families of leptons and quarks acquire their masses from Yukawa interactions of Higgs scalars

$$-\mathcal{L}_{Yukawa} = \sum y \bar{\psi}_L \phi \psi_R . \quad (1.34)$$

While the lower components of fermion doublets interact with  $\phi$ , the upper components interact with  $\phi^c$  because of non-zero VEV appearing in the lower component of Higgs doublet

$$-\mathcal{L}_{Yukawa} = \sum_{i,j=1}^3 (y_{ij}^e \bar{L}_i \phi E_j + y_{ij}^u \bar{Q}_i \phi^c U_j + y_{ij}^d \bar{Q}_i \phi D_j) + h.c. , \quad (1.35)$$

where fermions are introduced in their gauge eigenstates i.e.

$$\begin{aligned} L_L^e &= \{e^0, \mu^0, \tau^0\}_L & , & & Q_L^u &= \{u^0, c^0, t^0\}_L & , \\ L_L^\nu &= \{\nu_e^0, \nu_\mu^0, \nu_\tau^0\}_L & , & & Q_L^d &= \{d^0, s^0, b^0\}_L & , \\ E &= \{e^0, \mu^0, \tau^0\}_R^c & , & & U &= \{u^0, c^0, t^0\}_R^c & , \\ & & & & D &= \{d^0, s^0, b^0\}_R^c & . \end{aligned} \quad (1.36)$$

Notice that right-handed neutrinos ( $\nu_R$ ) do not exist in the framework of the SM which leaves neutrinos massless in the theory. However neutrino oscillation experiments showed that neutrinos have indeed very little mass.  $y_{ij}^e$ ,  $y_{ij}^u$  and  $y_{ij}^d$  are completely arbitrary  $3 \times 3$  matrices which ultimately determine the fermion masses and mixings. They do not have to be Hermitian, symmetric, diagonal or real. They are the most arbitrary aspect of the SM and they introduce most of the free parameters in the theory.

At the vacuum, the Yukawa Lagrangian for up-type quarks reads

$$\begin{aligned} -\mathcal{L}_{Yukawa}^u &= \sum_{i,j=1}^3 y_{ij}^u \bar{Q}_i \phi^c U_j = \sum_{i,j=1}^3 \bar{u}_{iL}^0 y_{ij}^u \left( \frac{v+H}{\sqrt{2}} \right) u_{jR}^{0c} + h.c \\ -\mathcal{L}_{Yukawa}^u &= \bar{u}_L^0 (M^u + h^u H) u_R^{0c} + h.c , \end{aligned} \quad (1.37)$$

where three families of up-type quarks are defined as  $u_L^0 = (u_1^0 u_2^0 u_3^0)_L^T$  in a 3 component column vector, with a similar definition for  $u_R^{0c}$ .  $M^u$  is a  $3 \times 3$  fermion mass matrix

$$M^u = y_{ij}^u \frac{v}{\sqrt{2}} , \quad (1.38)$$

and  $h^u$  is the  $3 \times 3$  Yukawa coupling matrix

$$h^u = \frac{y_{ij}^u}{\sqrt{2}} = \frac{M^u}{v} = \frac{g_L M^u}{2M_W} . \quad (1.39)$$

To switch to physical particle states, it is necessary to diagonalize the fermion mass matrix  $M^u$  by separate unitary transformations  $A_L$  and  $A_R$  on the left and right handed fermion fields,

$$A_L^{u\dagger} M^u A_R^u = M_D^u = \begin{pmatrix} m_u & 0 & 0 \\ 0 & m_c & 0 \\ 0 & 0 & m_t \end{pmatrix} \quad (1.40)$$

where the diagonal entries are real, non-negative eigenvalues corresponding to the physical masses of up-type quarks. The down type quark and charged lepton matrices are also diagonalized in a similar way by unitary transformations

$$A_L^{d\dagger} M^d A_R^d = M_D^d \quad , \quad A_L^{e\dagger} M^e A_R^e = M_D^e . \quad (1.41)$$

In terms of these unitary transformations physical eigenstates of fermion fields can be defined as

$$\begin{aligned} A_L^{e\dagger} e_L^0 &= (e_L \ \mu_L \ \tau_L)^T & , & & A_L^{u\dagger} u_L^0 &= (u_L \ c_L \ t_L)^T & , \\ A_R^{e\dagger} e_R^{0c} &= (e_R^c \ \mu_R^c \ \tau_R^c)^T & , & & A_R^{u\dagger} u_R^{0c} &= (u_R^c \ c_R^c \ t_R^c)^T & , \\ & & & & A_L^{d\dagger} d_L^0 &= (d_L \ s_L \ b_L)^T & , \\ & & & & A_R^{d\dagger} d_R^{0c} &= (d_R^c \ s_R^c \ b_R^c)^T & , \end{aligned} \quad (1.42)$$

so that the transition from gauge eigenstates to physical eigenstates is fairly easy

$$\bar{f}_L^0 M^f f_R^0 = \bar{f}_L M_D^f f_R \quad , \quad (1.43)$$

and with the following consequence

$$M_D^2 = (A_L^\dagger M A_R)(A_R^\dagger M^\dagger A_L) = (A_R^\dagger M^\dagger A_L)(A_L^\dagger M A_R) \quad , \quad (1.44)$$

$$M_D^2 = A_L^\dagger M M^\dagger A_L = A_R^\dagger M^\dagger M A_R \quad , \quad (1.45)$$

the diagonalizing matrices  $A_L$  and  $A_R$  can be obtained by computing the eigenvectors corresponding to the eigenvalues of  $M M^\dagger$  and  $M^\dagger M$ , respectively.

## 1.4 Electroweak Interactions

All electroweak interactions in the SM are generated from the kinetic part of the Lagrangian for both leptons and quarks:

$$\begin{aligned}
\mathcal{L}_{kinetic} &= i \sum \bar{\psi} \gamma^\mu D_\mu \psi \\
\mathcal{L}_{kinetic} &= i \sum_{j=1}^3 \left( \bar{L}_j \gamma^\mu D_\mu L_j + \bar{E}_j \gamma^\mu D_\mu E_j \right. \\
&\quad \left. + \bar{Q}_j \gamma^\mu D_\mu Q_j + \bar{U}_j \gamma^\mu D_\mu U_j + \bar{D}_j \gamma^\mu D_\mu D_j \right) . \tag{1.46}
\end{aligned}$$

There are three electroweak interactions: electromagnetic, neutral current and charged current interactions. To illustrate these let us consider only the first generation leptons and quarks; Equation (1.8) and Equation (1.10) lead us to the following interaction terms

$$\begin{aligned}
\mathcal{L}_{Kinetic}^{l,q} &= (\bar{\nu}_e \quad \bar{e})_L \frac{\gamma^\mu}{2} \begin{pmatrix} g_L W_\mu^3 - g_Y B_\mu & \sqrt{2} g_L W_\mu^+ \\ \sqrt{2} g_L W_\mu^- & -g_L W_\mu^3 - g_Y B_\mu \end{pmatrix} \begin{pmatrix} \nu_e \\ e \end{pmatrix}_L \\
&+ (\bar{u} \quad \bar{d})_L \frac{\gamma^\mu}{2} \begin{pmatrix} g_L W_\mu^3 + \frac{g_Y}{3} B_\mu & \sqrt{2} g_L W_\mu^+ \\ \sqrt{2} g_L W_\mu^- & -g_L W_\mu^3 + \frac{g_Y}{3} B_\mu \end{pmatrix} \begin{pmatrix} u \\ d \end{pmatrix}_L \\
&+ \bar{e}_R^c \gamma^\mu g_Y B_\mu e_R^c - \bar{u}_R^c \gamma^\mu \frac{2g_Y}{3} B_\mu u_R^c + \bar{d}_R^c \gamma^\mu \frac{g_Y}{3} B_\mu d_R^c . \tag{1.47}
\end{aligned}$$

Substituting the physical eigenstates for the neutral gauge bosons

$$\begin{pmatrix} W_\mu^3 \\ B_\mu \end{pmatrix} = \begin{pmatrix} \cos \theta_W & \sin \theta_W \\ -\sin \theta_W & \cos \theta_W \end{pmatrix} \begin{pmatrix} Z_\mu \\ A_\mu \end{pmatrix} \tag{1.48}$$

and defining the electric charge  $e = \frac{g_L g_Y}{g}$  we obtain all three electroweak interactions.

### 1.4.1 Electromagnetic Interactions

Electromagnetic interactions are mediated by massless photons therefore they are infinite-range interactions. From Equation (1.47) we have

$$\begin{aligned} \mathcal{L}_{EM} = & \left[ \bar{\nu}_e \frac{\gamma^\mu}{2} (g_L \sin \theta_W - g_Y \cos \theta_W) P_L \nu_e + \bar{e} \frac{\gamma^\mu}{2} (-g_L \sin \theta_W - g_Y \cos \theta_W) P_L e \right. \\ & + \bar{u} \frac{\gamma^\mu}{2} (g_L \sin \theta_W + \frac{g_Y}{3} \cos \theta_W) P_L u + \bar{d} \frac{\gamma^\mu}{2} (-g_L \sin \theta_W + \frac{g_Y}{3} \cos \theta_W) P_L d \\ & \left. + \bar{e}^c \gamma^\mu g_Y \cos \theta_W P_R e^c - \bar{u}^c \gamma^\mu \frac{2g_Y}{3} \cos \theta_W P_R u^c + \bar{d}^c \gamma^\mu \frac{g_Y}{3} \cos \theta_W P_R d^c \right] A_\mu \quad , \end{aligned} \quad (1.49)$$

$$\begin{aligned} \mathcal{L}_{EM} = & \left[ \bar{\nu}_e \gamma^\mu (0e) P_L \nu_e + \bar{e} \gamma^\mu (-e) P_L e + \bar{u} \gamma^\mu \left(\frac{2e}{3}\right) P_L u + \bar{d} \gamma^\mu \left(-\frac{e}{3}\right) P_L d \right. \\ & \left. + \bar{e}^c \gamma^\mu (e) P_R e^c + \bar{u}^c \gamma^\mu \left(\frac{-2e}{3}\right) P_R u^c + \bar{d}^c \gamma^\mu \left(\frac{e}{3}\right) P_R d^c \right] A_\mu \quad , \end{aligned} \quad (1.50)$$

where  $P_L$  and  $P_R$  are projection operators which separate left- and right-handed components of fermion fields. They are defined in Appendix A. It is obvious that a photon couples to fermions with their electric charges, so in general a photon only couples to electrically charged particles, it does not couple to neutrinos as they are electrically neutral. Therefore, the electromagnetic interactions can be described in a simpler form

$$\mathcal{L}_{EM} = e A_\mu J_A^\mu \quad , \quad (1.51)$$

where  $J_A^\mu$  is the electromagnetic current which covers the three flavors of fermions

$$\begin{aligned} J_A^\mu &= \sum_i Q^i \bar{f}_i \gamma^\mu f_i \\ J_A^\mu &= Q^e \bar{e} \gamma^\mu e + Q^u \bar{u} \gamma^\mu u + Q^d \bar{d} \gamma^\mu d \quad , \end{aligned} \quad (1.52)$$

The Feynman diagram of electromagnetic interactions is given in Figure 2.

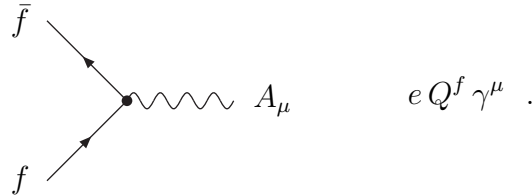


Figure 2: Feynman diagram of electromagnetic interactions in the SM.

## 1.4.2 Neutral Current Weak Interactions

Neutral current interactions are transmitted by neutral  $Z$  bosons. Because of broken electroweak symmetry (massive  $Z$  bosons) they are short-range interactions. From Equation (1.47), the neutral current interactions can be summarized as

$$\begin{aligned} \mathcal{L}_{NC} = & \left[ \bar{\nu}_e \frac{\gamma^\mu}{2} (g_L \cos \theta_W + g_Y \sin \theta_W) P_L \nu_e + \bar{e} \frac{\gamma^\mu}{2} (-g_L \cos \theta_W + g_Y \sin \theta_W) P_L e \right. \\ & + \bar{u} \frac{\gamma^\mu}{2} (g_L \cos \theta_W - \frac{g_Y}{3} \sin \theta_W) P_L u + \bar{d} \frac{\gamma^\mu}{2} (-g_L \cos \theta_W - \frac{g_Y}{3} \sin \theta_W) P_L d \\ & \left. - \bar{e}^c \gamma^\mu g_Y \sin \theta_W P_R e^c + \bar{u}^c \gamma^\mu \frac{2g_Y}{3} \sin \theta_W P_R u^c - \bar{d}^c \gamma^\mu \frac{g_Y}{3} \sin \theta_W P_R d^c \right] Z_\mu \ , \end{aligned} \quad (1.53)$$

$$\begin{aligned} \mathcal{L}_{NC} = & \left[ \bar{\nu}_e \gamma^\mu \frac{g_L}{\cos \theta_W} \left(\frac{1}{2}\right) P_L \nu_e + \bar{e} \gamma^\mu \frac{g_L}{\cos \theta_W} \left(-\frac{1}{2} + \sin^2 \theta_W\right) P_L e \right. \\ & + \bar{u} \gamma^\mu \frac{g_L}{\cos \theta_W} \left(\frac{1}{2} - \frac{2}{3} \sin^2 \theta_W\right) P_L u + \bar{d} \gamma^\mu \frac{g_L}{\cos \theta_W} \left(-\frac{1}{2} + \frac{1}{3} \sin^2 \theta_W\right) P_L d \\ & + \bar{e}^c \gamma^\mu \frac{g_L}{\cos \theta_W} (-\sin^2 \theta_W) P_R e^c + \bar{u}^c \gamma^\mu \frac{g_L}{\cos \theta_W} \left(\frac{2}{3} \sin^2 \theta_W\right) P_R u^c \\ & \left. + \bar{d}^c \gamma^\mu \frac{g_L}{\cos \theta_W} \left(-\frac{1}{3} \sin^2 \theta_W\right) P_R d^c \right] Z_\mu \ . \end{aligned} \quad (1.54)$$

Equation (1.54) can be simplified further

$$\mathcal{L}_{NC} = \frac{g_L}{\cos \theta_W} Z_\mu J_Z^\mu \ , \quad (1.55)$$

where  $J_Z^\mu$  is neutral current given by

$$J_Z^\mu = \sum_i (T^i P_L - Q^i \sin^2 \theta_W) \bar{f}_i \gamma^\mu f_i \ , \quad (1.56)$$

$T$  and  $Q$  are the weak isospin and electric charge of the fermion fields, respectively. Figure 3 shows the Feynman diagram of neutral current interactions in the SM.

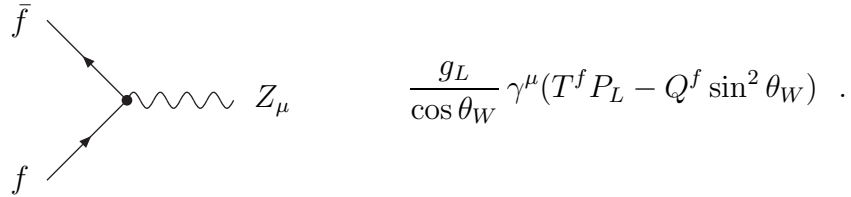


Figure 3: Feynman diagram of neutral current interactions in the SM.

### 1.4.3 Charged Current Weak Interactions

Mediators of charged current interactions are the charged  $W^\pm$  gauge bosons. Since the  $W^\pm$  bosons are massive, these interactions are short-range interactions as well. The Lagrangian of charged current interactions can be inferred from Equation (1.47) as

$$\mathcal{L}_{CC} = \frac{g_L}{\sqrt{2}}(W_\mu^- J_W^\mu + W_\mu^+ J_W^{\mu\dagger}) \quad , \quad (1.57)$$

where  $J_W^\mu$  is the charged current and  $J_W^{\mu\dagger}$  its conjugate

$$\begin{aligned} J_W^\mu &= \sum_{i,j} (\bar{e}_{Lj} \gamma^\mu \nu_{Li} \delta_{ij} + \bar{d}_{Lj} \gamma^\mu u_{Li} V_{ij}^\dagger) \quad , \\ J_W^{\mu\dagger} &= \sum_{i,j} (\bar{\nu}_{Li} \gamma^\mu e_{Lj} \delta_{ij} + \bar{u}_{Li} \gamma^\mu d_{Lj} V_{ij}) \quad . \end{aligned} \quad (1.58)$$

In the lepton sector, since neutrinos are massless in the SM, their eigenstates are arbitrary. There is nothing to distinguish them except their weak interactions. So it is acceptable to define  $\nu_e$ ,  $\nu_\mu$ , and  $\nu_\tau$  as the weak interaction partners of  $e$ ,  $\mu$ , and  $\tau$  respectively. This ensures that  $A_L^\nu = A_L^e$  so that the physical eigenstates of neutrinos are  $\nu_L = A_L^{e\dagger} \nu_L^0$ . Therefore,

$$\bar{\nu}_k^0 \gamma^\mu e_k^0 = \bar{\nu}_i \gamma^\mu A_{ik}^{e\dagger} A_{kj}^e e_j = \bar{\nu}_i \gamma^\mu e_j \delta_{ij} \quad , \quad (1.59)$$

hence the  $W^\pm$  boson does not mix lepton flavors. The Feynman diagram of leptons charged current interactions is given in Figure 4.

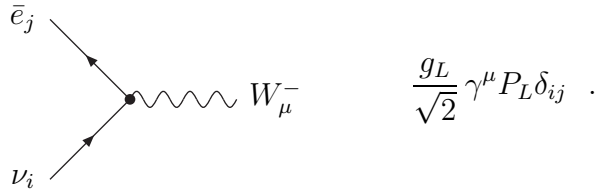


Figure 4: Feynman diagram of leptons charged current interactions in the SM.

However, in the quark sector things are different: since all quarks are massive particles their physical eigenstates mix with a  $3 \times 3$  matrix in the charged current interactions. That is,

$$\bar{u}_k^0 \gamma^\mu d_k^0 = \bar{u}_i \gamma^\mu A_{ik}^{u\dagger} A_{kj}^d d_j = \bar{u}_i \gamma^\mu d_j V_{ij} \quad (1.60)$$

and  $A_{ik}^{u\dagger} A_{kj}^d = V_{ij}$  is the so-called Cabibbo-Kobayashi-Maskawa (CKM) quark mixing matrix.

$$V_{CKM} = \begin{pmatrix} V_{ud} & V_{us} & V_{ub} \\ V_{cd} & V_{cs} & V_{cb} \\ V_{td} & V_{ts} & V_{tb} \end{pmatrix} \quad (1.61)$$

The standard parametrization of the CKM matrix involves three Euler angles  $(\theta_{12}, \theta_{23}, \theta_{13})$  and one CP violating phase  $\delta_{13}$ :

$$V_{CKM} = \begin{pmatrix} c_{12} c_{13} & s_{12} c_{13} & s_{13} e^{-i\delta_{13}} \\ -s_{12} c_{23} - c_{12} s_{23} s_{13} e^{i\delta_{13}} & c_{13} c_{23} - s_{12} s_{23} s_{13} e^{i\delta_{13}} & s_{23} c_{13} \\ s_{12} s_{23} - c_{12} c_{23} s_{13} e^{i\delta_{13}} & -c_{12} s_{23} - s_{12} c_{23} s_{13} e^{i\delta_{13}} & c_{23} c_{13} \end{pmatrix} \quad (1.62)$$

where  $c_{ij}$  and  $s_{ij}$  are cosines and sines of mixing angles  $(\theta_{12}, \theta_{23}, \theta_{13})$ . Another useful parametrization is the Wolfenstein parametrization in which the hierarchical structure of mixings between generations is clearly seen

$$V_{CKM} \sim \begin{pmatrix} 1 & \lambda & \lambda^3 \\ -\lambda & 1 & \lambda^2 \\ \lambda^3 & -\lambda^2 & 1 \end{pmatrix} \quad (1.63)$$

where  $\lambda = \sin \theta_{12}$  and the Cabibbo angle  $\theta_{12}$  is the mixing of the first two generations which is precisely measured in various experiments ( $\sin \theta_{12} \sim 0.23$ ). And Figure 5 shows the Feynman diagram of quarks charged current interactions in the SM.

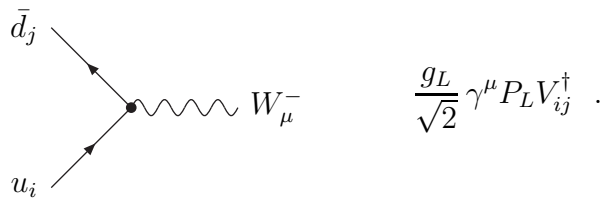


Figure 5: Feynman diagram of quarks charged current interactions in the SM.

## 1.5 Challenges in the Standard Model

The SM was developed in 1960's and finalized to its ultimate form in 1970's with the experimental confirmation of the existence of the quarks. First, electromagnetic and



weak interactions were combined in electroweak theory by Sheldon Glashow, and then the Higgs Mechanism was incorporated by Steven Weinberg and Abdus Salam giving the SM its modern form. Since then, most of the SM predictions were experimentally confirmed;

- Discovery of quarks in deep inelastic scattering experiments: up, down, and strange quarks (Stanford Linear Accelerator Center (SLAC) 1968), charm quark (SLAC and Berkeley National Laboratory (BNL) 1974), bottom quark (Fermilab (FNAL) 1977) and finally top quark (FNAL 1995).
- Neutral weak currents were discovered at European Council for Nuclear Research (CERN) in 1973,
- $W^\pm$  and  $Z^0$  bosons were discovered by UA1 and UA2 collaborations at CERN in 1983. Their masses were measured to be exactly the same as the SM predicted.
- And many other sub-atomic phenomenons that are predicted by the SM were experimentally confirmed up to date.

Because of its success in explaining a large variety of experimental results, the SM commonly regarded as the theory of almost everything.

Despite being the most successful theory of particle physics to date, the SM is not perfect. There are a number of experimental observations for which the SM does not give an adequate explanation. First of all, it cannot provide an explanation of gravity which is one of the four fundamental forces in nature. Then, according to the SM the neutrinos are massless particles. However, neutrino oscillation experiments have shown that neutrinos do actually have a small mass. The SM predicts that matter and anti-matter should have been created in (almost) equal amounts, which would have annihilated each other as the universe cooled. However, the cosmological observations showed that there is a matter-anti-matter asymmetry in the universe, i.e, the universe is made out of mostly matter. The SM is able to explain only about 4% of the energy present in the universe, 24% is accounted for the dark matter which interacts only weakly with SM fields, and the rest is considered to be the dark energy, a constant energy density for the vacuum. Attempts to explain the dark energy in terms of vacuum energy of the SM lead to a mismatch of 120 orders of magnitude.

Besides experimental discrepancies there are some theoretical problems as well in the model. Some features of the SM are added in an ad hoc way. These are not a

problem per-se, i.e, the theory works fine with these ad-hoc features, but they imply a lack of understanding. Some of the ad hoc features are: the hierarchy problem, the strong CP problem, and the number of parameters. The SM introduces particle masses through a process known as spontaneous symmetry breaking caused by the Higgs field. Within the SM, the mass of the Higgs field gets some very large quantum corrections due to the presence of virtual particles, mostly virtual top quarks. These corrections are much larger than the actual mass of the Higgs field. This means that the bare mass parameter of the Higgs field in the SM must be fine tuned in such a way that almost completely cancels the quantum corrections. This level of fine tuning is deemed unnatural by many theorists and called the hierarchy problem. In order to explain the matter-anti-matter asymmetry a term that breaks CP symmetry in the strong interaction sector may be included in the context of the SM; however no such violation has been found so far implying that the coefficient of this term is very close to zero. This fine tuning is also unnatural and called the strong CP problem. Finally the SM depends on 19 numerical parameters. Their values are known from experiments, but the origin of the values is unknown. With all those inconsistencies in the SM, theorists try to extend the SM or establish new models in order to explain all these problems and to find the true symmetry of the nature. Theories that lie beyond the Standard Model include natural extensions of the SM such as Grand Unified Theories, Left-Right Symmetric Models or supersymmetric extensions, such as the Minimal Supersymmetric Standard Model, Next-to-Minimal Supersymmetric Standard Model, or entirely novel explanations, such as string theory, M-theory and extra dimensions.

In this work we concentrate on Left-Right Symmetric Models as a natural extension of the SM and investigate some features of  $W_R$  gauge boson detection at the Tevatron and the LHC. The LHC, being the most powerful and the largest magnifier ever, it is a wonderful opportunity to find new particles and interactions and to test the new theories beyond the SM. There are a number of studies investigating a new neutral gauge boson which would be a signal for an extra  $U(1)$  symmetry. However, the search for a new charged gauge boson is far less than that. A charged gauge boson would indicate an extra  $SU(2)$  symmetry and one can easily test chiral interactions to determine whether the underlying symmetry is  $SU(2)_L$  or  $SU(2)_R$ .

In the next chapter we give the details and descriptions of the Left-Right Symmetric Model. Then in Chapter 3 we focus on  $b \rightarrow d, s$  transitions in an asymmetric class of  $SU(2)_L \times SU(2)_R \times U(1)_{B-L}$  models, with a simple, one-parameter structure of the right-handed mixing matrix for the quarks, which obey the constraints of Kaon physics. We impose experimental constraints on the branching ratios of  $b \rightarrow s\gamma$ ,  $b \rightarrow ce\bar{\nu}_e$ , and  $B_{d,s}^0 - \bar{B}_{d,s}^0$  mixing to restrict the parameters of the model:  $g_R/g_L, M_{W_R}, M_{H^\pm}, \tan\beta$  as well as the elements of the right-handed quark mixing matrix  $V_{CKM}^R$ .

In Chapter 4 we analyze the single  $W_R$  boson production in the asymmetric left-right model, where the left and right quark mixing matrices are not constrained to be equal. We investigate the cross sections as well as the branching ratios of  $W_R$  bosons at the LHC, including constraints from low-energy phenomenology. We then look for most likely signals in  $pp \rightarrow W_R t \rightarrow t$  (*dijet*) production. Including the background, we find that LHC could show significant signals for the new charged bosons. We compare our results throughout with those of the manifest left-right symmetric model and comment on similarities and differences.

Finally in Chapter 5, in light of the recent measurements of the top quark forward-backward asymmetry at the Fermilab Tevatron experiment, which in some regions of the parameter space shows a discrepancy of  $3\sigma$  compared to the SM prediction, we analyze top quark pair production and asymmetry in the context of left-right models both at the Tevatron and LHC. We use the minimal manifest left-right model and an asymmetric left-right model where gauge couplings and flavor mixing in the right-handed sector are allowed to differ from those in the left-handed sector. We explore the consequences of including effects from  $W_R$  and  $Z_R$  gauge bosons, consistent with phenomenological constraints from meson mixing and new bounds from ATLAS and CMS, for the  $t\bar{t}$  cross section, invariant mass distribution and forward-backward asymmetry at the Tevatron, and predict their values at the LHC. We show that, varying the parameters of the model while preserving agreement with collider, electroweak precision, and flavor violation data, the generic left-right model cannot account for the large deviations of the observed asymmetry at the Tevatron and also that it predicts very small charge asymmetries at the LHC.

# Chapter 2

## LEFT-RIGHT SYMMETRIC MODEL

### 2.1 Model Description

The main motivation for the Left-Right Symmetric Model (LRSM) is to treat the right-handed particles and their interactions on an equal footing with the left ones. The SM breaks parity maximally, that is all the fermions in the model are chiral Weyl fermions which means that the weak gauge bosons  $W^\pm$  and  $Z$  only couple to left-handed leptons and quarks. Apparently left-handed particles and interactions are favored in the SM, but a proper answer to the question 'Why should nature prefer such a discrimination?' is absent. Moreover, as recent experiments showed that neutrinos do indeed have small masses, it means they in fact can flip their chirality under proper circumstances which is not allowed in the context of the SM because there is no room for right-handed neutrinos. Following these motivations, the LRSM, being a natural extension of the SM, can fulfill the above requirements and also may give some interesting consequences.

The weak interactions of LRSM are based on the gauge group  $SU(2)_L \times SU(2)_R \times U(1)_{B-L}$  where  $B - L$  stands for the difference in baryon and lepton numbers. The field content of the model and quantum numbers are given in Table 2. Contrary to the SM, all right-handed component of fermion fields transform as doublets under  $SU(2)_R$  symmetry in the LRSM; the corresponding gauge bosons of this new symmetry only couple to right-handed fermions. This Left-Right (LR) symmetry emerged from the

idea that the physical laws must be as valid for right-handed motions as they are for the left-handed ones.

Fields	Components	$SU(2)_L \times SU(2)_R \times U(1)_{B-L}$		
<b>Fermions</b>				
$L_L$	$\begin{bmatrix} \nu \\ e \end{bmatrix}_L$	2	1	-1
$L_R$	$\begin{bmatrix} \nu \\ e \end{bmatrix}_R$	1	2	-1
$Q_L$	$\begin{bmatrix} u \\ d \end{bmatrix}_L$	2	1	$+\frac{1}{3}$
$Q_R$	$\begin{bmatrix} u \\ d \end{bmatrix}_R$	1	2	$+\frac{1}{3}$
<b>Gauge bosons</b>				
$W_L$	$W_L^+, W_L^-, W_L^3$	3	1	0
$W_R$	$W_R^+, W_R^-, W_R^3$	1	3	0
$V$	$V^0$	1	1	0
<b>Higgs</b>				
$\Phi$	$\begin{bmatrix} \Phi_1^0 & \Phi_1^+ \\ \Phi_2^- & \Phi_2^0 \end{bmatrix}$	2	2	0
$\Delta_L$	$\begin{bmatrix} \frac{\Delta^+}{\sqrt{2}} & \Delta^{++} \\ \Delta^0 & -\frac{\Delta^+}{\sqrt{2}} \end{bmatrix}_L$	3	1	+2
$\Delta_R$	$\begin{bmatrix} \frac{\Delta^+}{\sqrt{2}} & \Delta^{++} \\ \Delta^0 & -\frac{\Delta^+}{\sqrt{2}} \end{bmatrix}_R$	1	3	+2

Table 2: Field content of the LRSM and respective quantum numbers in  $SU(2)_L \times SU(2)_R \times U(1)_{B-L}$  gauge structure.

It was shown by Mohapatra and Senjanovic [2] in 1975 that the LR symmetry can be spontaneously broken to give a chiral low-energy theory which is the SM at the weak scale and the small neutrino masses via the see-saw mechanism. The complete symmetry breaking pattern of the LRSM is accomplished in two stages

$$\begin{aligned} SU(3)_C \times SU(2)_L \times SU(2)_R \times U(1)_{B-L} &\longrightarrow SU(3)_C \times SU(2)_L \times U(1)_Y \ , \\ SU(3)_C \times SU(2)_L \times U(1)_Y &\longrightarrow SU(3)_C \times U(1)_{EM} \ , \end{aligned} \quad (2.1)$$

where the electromagnetic charge is defined by the modified Gell-Mann-Nishijima formula

$$Q = T_L + T_R + \frac{Y_{B-L}}{2} \ . \quad (2.2)$$

The Lagrangian density of the LRSM can be summarized in the same way as in the SM (see Equation (1.4)).

- Gauge Lagrangian

The gauge part of the Lagrangian density contains the gauge bosons kinetic energy terms as well as the three- and four-point self interactions for the gauge fields  $G_\mu^a, W_{L\mu}^i$  and  $W_{R\mu}^i$ :

$$\begin{aligned} \mathcal{L}_{Gauge} &= -\frac{1}{4} \sum F_{\mu\nu} F^{\mu\nu} \\ \mathcal{L}_{Gauge} &= -\frac{1}{4} G_{\mu\nu}^a G^{\mu\nu a} - \frac{1}{4} W_{L\mu\nu}^i W_L^{\mu\nu i} - \frac{1}{4} W_{R\mu\nu}^i W_R^{\mu\nu i} - \frac{1}{4} V_{\mu\nu} V^{\mu\nu} \ , \end{aligned} \quad (2.3)$$

where the field strength tensors for  $SU(3)_C, SU(2)_L, SU(2)_R$  and  $U(1)_{B-L}$  are, respectively,

$$\begin{aligned} G_{\mu\nu}^a &= \partial_\mu G_\nu^a - \partial_\nu G_\mu^a - g_s f_{abc} G_\mu^b G_\nu^c \ , \quad a, b, c = 1 \dots 8 \ , \\ W_{L\mu\nu}^i &= \partial_\mu W_{L\nu}^i - \partial_\nu W_{L\mu}^i - g_L \epsilon_{ijk} W_{L\mu}^j W_{L\nu}^k \ , \quad i, j, k = 1 \dots 3 \ , \\ W_{R\mu\nu}^i &= \partial_\mu W_{R\nu}^i - \partial_\nu W_{R\mu}^i - g_R \epsilon_{ijk} W_{R\mu}^j W_{R\nu}^k \ , \quad i, j, k = 1 \dots 3 \ , \\ V_{\mu\nu} &= \partial_\mu V_\nu - \partial_\nu V_\mu \ , \end{aligned} \quad (2.4)$$

$g_s, g_L$  and  $g_R$  are gauge coupling constants while  $f_{abc}$  and  $\epsilon_{ijk}$  are generators in adjoint representations of  $SU(3)$  and  $SU(2)$  groups, respectively.

- Kinetic Lagrangian

The kinetic part of the Lagrangian density constitutes the kinetic terms of fermions and gauge bosons

$$\begin{aligned}\mathcal{L}_{Kinetic} &= i \sum \bar{\psi} \gamma^\mu D_\mu \psi \\ \mathcal{L}_{Kinetic} &= i \sum_{j=1}^3 \left( \bar{L}_{Lj} \gamma^\mu D_\mu L_{Lj} + \bar{L}_{Rj} \gamma^\mu D_\mu L_{Rj} + \bar{Q}_{Lj} \gamma^\mu D_\mu Q_{Lj} + \bar{Q}_{Rj} \gamma^\mu D_\mu Q_{Rj} \right),\end{aligned}\tag{2.5}$$

the covariant derivative takes the following forms for each term

$$\bar{L}_L \gamma^\mu D_\mu L_L = \bar{L}_L \gamma^\mu \left( \partial_\mu - \frac{ig_L}{2} \sigma \cdot W_{L\mu} + \frac{ig_{B-L}}{2} V_\mu \right) L_L, \tag{2.6}$$

$$\bar{L}_R \gamma^\mu D_\mu L_R = \bar{L}_R \gamma^\mu \left( \partial_\mu - \frac{ig_R}{2} \sigma \cdot W_{R\mu} + \frac{ig_{B-L}}{2} V_\mu \right) L_R, \tag{2.7}$$

$$\bar{Q}_L^\alpha \gamma^\mu D_\mu Q_L^\beta = \bar{Q}_L^\alpha \gamma^\mu \left[ \left( \partial_\mu - \frac{ig_L}{2} \sigma \cdot W_{L\mu} - \frac{ig_{B-L}}{6} V_\mu \right) \delta_{\alpha\beta} - \frac{ig_s}{2} \lambda_{\alpha\beta} \cdot G_\mu \right] Q_L^\beta, \tag{2.8}$$

$$\bar{Q}_R^\alpha \gamma^\mu D_\mu Q_R^\beta = \bar{Q}_R^\alpha \gamma^\mu \left[ \left( \partial_\mu - \frac{ig_R}{2} \sigma \cdot W_{R\mu} - \frac{ig_{B-L}}{6} V_\mu \right) \delta_{\alpha\beta} - \frac{ig_s}{2} \lambda_{\alpha\beta} \cdot G_\mu \right] Q_R^\beta, \tag{2.9}$$

where the strong and weak interactions of fermions and bosons are encoded in these kinetic terms.

- Scalar Lagrangian

The scalar part of the Lagrangian contains the kinetic terms and potential of Higgs multiplets

$$\mathcal{L}_{Higgs} = \sum_i Tr |D_\mu \phi_i|^2 - V_{Higgs}, \tag{2.10}$$

where the Higgs multiplets are  $\phi_i = \{\Phi, \Delta_L, \Delta_R\}$ . Gauge bosons mass terms are encoded in the kinetic part of the above equation. The form of the covariant derivative for each multiplet is explicitly given in Appendix A. The most general CP-invariant and renormalizable Higgs potential is

$$\begin{aligned}
V_{Higgs} = & - \mu_1^2 Tr(\Phi^\dagger \Phi) - \mu_2^2 [Tr(\tilde{\Phi} \Phi^\dagger) + Tr(\tilde{\Phi}^\dagger \Phi)] - \mu_3^2 [Tr(\Delta_L \Delta_L^\dagger) + Tr(\Delta_R \Delta_R^\dagger)] \\
& + \lambda_1 [Tr(\Phi \Phi^\dagger)]^2 + \lambda_2 \{ [Tr(\tilde{\Phi} \Phi^\dagger)]^2 + [Tr(\tilde{\Phi}^\dagger \Phi)]^2 \} + \lambda_3 [Tr(\tilde{\Phi} \Phi^\dagger) Tr(\tilde{\Phi}^\dagger \Phi)] \\
& + \lambda_4 \{ Tr(\Phi \Phi^\dagger) [Tr(\tilde{\Phi} \Phi^\dagger) + Tr(\tilde{\Phi}^\dagger \Phi)] \} + \rho_1 \{ [Tr(\Delta_L \Delta_L^\dagger)]^2 + [Tr(\Delta_R \Delta_R^\dagger)]^2 \} \\
& + \rho_2 [Tr(\Delta_L \Delta_L) Tr(\Delta_L^\dagger \Delta_L^\dagger) + Tr(\Delta_R \Delta_R) Tr(\Delta_R^\dagger \Delta_R^\dagger)] + \rho_3 [Tr(\Delta_L \Delta_L^\dagger) \\
& \times Tr(\Delta_R \Delta_R^\dagger)] + \rho_4 [Tr(\Delta_L \Delta_L) Tr(\Delta_R^\dagger \Delta_R^\dagger) + Tr(\Delta_L^\dagger \Delta_L^\dagger) Tr(\Delta_R \Delta_R)] \\
& + \alpha_1 \{ Tr(\Phi \Phi^\dagger) [Tr(\Delta_L \Delta_L^\dagger) + Tr(\Delta_R \Delta_R^\dagger)] \} + \alpha_2 [Tr(\Phi \tilde{\Phi}^\dagger) + Tr(\Phi^\dagger \tilde{\Phi})] \\
& \times [Tr(\Delta_L \Delta_L^\dagger) + Tr(\Delta_R \Delta_R^\dagger)] + \alpha_3 [Tr(\Phi \Phi^\dagger \Delta_L \Delta_L^\dagger) + Tr(\Phi^\dagger \Phi \Delta_R \Delta_R^\dagger)] \\
& + \beta_1 [Tr(\Phi \Delta_R \Phi^\dagger \Delta_L^\dagger) + Tr(\Phi^\dagger \Delta_L \Phi \Delta_R^\dagger)] + \beta_2 [Tr(\tilde{\Phi} \Delta_R \Phi^\dagger \Delta_L^\dagger) \\
& + Tr(\tilde{\Phi}^\dagger \Delta_L \Phi \Delta_R^\dagger)] + \beta_3 [Tr(\Phi \Delta_R \tilde{\Phi}^\dagger \Delta_L^\dagger) + Tr(\Phi^\dagger \Delta_L \tilde{\Phi} \Delta_R^\dagger)] \quad , \quad (2.11)
\end{aligned}$$

where all the coefficients are real. Since our interest is not on the Higgs sector of the model, we will give a general overview of the Higgs sector in section 2.4.

- Yukawa Lagrangian

This part of the Lagrangian contains Yukawa-type interactions of fermions with Higgs multiplets

$$\begin{aligned}
-\mathcal{L}_{Yukawa} &= \sum y \bar{\psi}_L \Phi \psi_R \\
-\mathcal{L}_{Yukawa} &= \sum_{i,j=1}^3 \left( y_{ij}^L \bar{L}_{Li} \Phi L_{Rj} + \tilde{y}_{ij}^L \bar{L}_{Li} \tilde{\Phi} L_{Rj} + y_{ij}^Q \bar{Q}_{Li} \Phi Q_{Rj} + \tilde{y}_{ij}^Q \bar{Q}_{Li} \tilde{\Phi} Q_{Rj} \right. \\
&\quad \left. + y_{ij}^\Delta (L_{Li}^T i\sigma_2 \Delta_L L_{Lj} + L_{Ri}^T i\sigma_2 \Delta_R L_{Rj}) \right) + h.c. \quad , \quad (2.12)
\end{aligned}$$

here  $y_{ij}^L, \tilde{y}_{ij}^L, y_{ij}^Q, \tilde{y}_{ij}^Q$  and  $y_{ij}^\Delta$  are  $3 \times 3$  Yukawa matrices which again will determine fermion masses and mixings. For the conjugated Higgs bidoublet, it is defined by

$$\tilde{\Phi} = \sigma_2 \Phi^* \sigma_2 = \begin{pmatrix} \Phi_2^0 & -\Phi_2^+ \\ -\Phi_1^- & \Phi_1^0 \end{pmatrix} . \quad (2.13)$$

## 2.2 Spontaneous Symmetry Breaking in the LRSM

The Lagrangian of the LRSM is completely invariant under  $SU(2)_L \times SU(2)_R \times U(1)_{B-L}$ . Therefore all the fermions and gauge bosons are massless before the SSB.



The symmetry breaking of the LRSM is spontaneously achieved in two steps and it is similar to that of the SM, that is, it occurs via the VEV of scalar Higgs multiplets. The symmetry breaking scheme is as follows

$$SU(2)_L \times SU(2)_R \times U(1)_{B-L} \xrightarrow{\langle \Delta_R \rangle} SU(2)_L \times U(1)_Y \quad . \quad (2.14)$$

At this stage the right-handed scalar Higgs triplet gets a VEV and breaks the LR symmetry to electroweak symmetry. Physical  $W_{R\mu}^\pm$  and  $Z_{R\mu}^0$  gauge bosons gain their masses by interacting with right-handed Higgs triplet. The next step is the breaking of the electroweak symmetry which is exactly the same as in the SM

$$SU(2)_L \times U(1)_Y \xrightarrow{\langle \Phi \rangle, \langle \Delta_L \rangle} U(1)_{EM} \quad , \quad (2.15)$$

where bidoublet Higgs and (possibly but not necessarily) left-handed Higgs triplet get VEV and break the electroweak symmetry to electromagnetism. Consequently physical  $W_{L\mu}^\pm$  and  $Z_{L\mu}^0$  gauge bosons acquire their masses. The VEVs of Higgs scalars are

$$\langle \Phi \rangle = \frac{1}{\sqrt{2}} \begin{pmatrix} v_u & 0 \\ 0 & v_d \end{pmatrix} , \quad \langle \Delta_R \rangle = \frac{1}{\sqrt{2}} \begin{pmatrix} 0 & 0 \\ v_R & 0 \end{pmatrix} , \quad \langle \Delta_L \rangle = \frac{1}{\sqrt{2}} \begin{pmatrix} 0 & 0 \\ v_L & 0 \end{pmatrix} . \quad (2.16)$$

The hierarchy between VEVs is like  $v_R \gg (v_u, v_d) \gg v_L$ . Since the electroweak analysis lead to the constraint  $v_L \leq 10$  GeV and the see-saw mechanism for small left-handed neutrino masses requires  $v_L \leq$  a few MeV, we will work at the limit  $v_L \rightarrow 0$  in this thesis. The value  $\sqrt{v_u^2 + v_d^2} = v \equiv 246$  GeV is chosen to be compatible with the SM.

## 2.2.1 Generation of Gauge Boson Masses in the LRSM

Gauge bosons masses arise from Higgs fields kinetic terms. At the first step, right-handed Higgs triplet takes a VEV  $\langle \Delta_R \rangle = v_R$  and breaks the LR symmetry as in Equation (2.14). The corresponding Higgs kinetic terms are

$$\begin{aligned} Tr|D_\mu \Delta_R|^2 &= Tr[(D^\mu \Delta_R)^\dagger (D_\mu \Delta_R)] \\ &= \frac{g_R^2 v_R^2}{2} W_R^{\mu-} W_{R\mu}^+ + \frac{v_R^2}{2} (g_R W_R^{\mu 3} - g_{B-L} V^\mu) (g_R W_{R\mu}^3 - g_{B-L} V_\mu) \quad . \end{aligned} \quad (2.17)$$

Neutral fields can be diagonalized by an orthogonal transformation and the compositions of the physical gauge bosons in terms of gauge eigenstates become

$$W_{R\mu}^\pm = \frac{W_{R\mu}^1 \mp iW_{R\mu}^2}{\sqrt{2}} , \quad \begin{pmatrix} Z_{R\mu} \\ B_\mu \end{pmatrix} = \begin{pmatrix} \cos \varphi & -\sin \varphi \\ \sin \varphi & \cos \varphi \end{pmatrix} \begin{pmatrix} W_{R\mu}^3 \\ V_\mu \end{pmatrix} , \quad (2.18)$$

where  $\varphi$  is a mixing angle which plays a similar role as the SM Weinberg angle ( $\theta_W$ ),

$$\cos \varphi = \frac{g_R}{\sqrt{g_R^2 + g_{B-L}^2}} \quad , \quad \sin \varphi = \frac{g_{B-L}}{\sqrt{g_R^2 + g_{B-L}^2}} \quad . \quad (2.19)$$

At this stage of  $SU(2)_R \times U(1)_{B-L}$  breaking, the neutral gauge eigenstates  $W_{R\mu}^3$  and  $V_\mu$  mix to give a physical massless state which will be identified as the hypercharge  $B_\mu$  field and a physical massive  $Z_{R\mu}$  boson which will decouple from the further breakdown process.

The second stage is controlled by the Higgs bidoublet getting a non zero VEV  $\langle \Phi \rangle \neq 0$  and possibly, but not necessarily, by the left triplet VEV  $\langle \Delta_L \rangle = v_L$ . The left-handed Higgs triplet ( $\Delta_L$ ) is only responsible for maintaining the discrete parity symmetry [3] in the theory, whereas the Higgs bidoublet is needed to give masses to leptons, quarks and SM gauge bosons. The kinetic terms for left triplet and bidoublet Higgs fields are

$$\begin{aligned} Tr|D_\mu \Delta_L|^2 &= Tr[(D^\mu \Delta_L)^\dagger (D_\mu \Delta_L)] \\ &= \frac{g_L^2 v_L^2}{2} W_L^{\mu-} W_{L\mu}^+ + \frac{v_L^2}{2} (g_L W_L^{\mu 3} - g_{B-L} V^\mu)(g_L W_{L\mu}^3 - g_{B-L} V_\mu) \end{aligned} \quad (2.20)$$

and

$$\begin{aligned} Tr|D_\mu \Phi|^2 &= Tr[(D^\mu \Phi)^\dagger (D_\mu \Phi)] \\ &= \frac{v^2}{8} (g_L W_L^{\mu 3} - g_R W_R^{\mu 3})(g_L W_{L\mu}^3 - g_R W_{R\mu}^3) \\ &\quad + \frac{v^2}{4} (g_L^2 W_L^{\mu+} W_{L\mu}^- + g_R^2 W_R^{\mu+} W_{R\mu}^-) \\ &\quad - \frac{g_L g_R v_u v_d}{2} (W_L^{\mu+} W_{R\mu}^- + W_R^{\mu+} W_{L\mu}^-) \end{aligned} \quad (2.21)$$

and the compositions of physical gauge bosons at this stage are

$$W_{L\mu}^\pm = \frac{W_{L\mu}^1 \mp i W_{L\mu}^2}{\sqrt{2}} \quad , \quad \begin{pmatrix} Z_{L\mu} \\ A_\mu \end{pmatrix} = \begin{pmatrix} \cos \theta_W & -\sin \theta_W \\ \sin \theta_W & \cos \theta_W \end{pmatrix} \begin{pmatrix} W_{L\mu}^3 \\ B_\mu \end{pmatrix} \quad , \quad (2.22)$$

where the Weinberg mixing angle is defined as

$$\cos \theta_W = \frac{g_L}{\sqrt{g_L^2 + g_Y^2}} \quad , \quad \sin \theta_W = \frac{g_Y}{\sqrt{g_L^2 + g_Y^2}} \quad , \quad g_Y = \frac{g_R g_{B-L}}{\sqrt{g_R^2 + g_{B-L}^2}} \quad , \quad (2.23)$$

and the hypercharge coupling constant ( $g_Y$ ) is related to the coupling constants of the unbroken LR symmetry ( $g_R$  and  $g_{B-L}$ ).

Now it is easy to extract the neutral and charged gauge bosons mass matrices from those Higgs kinetic terms above. The mass squared matrix for neutral gauge bosons in the basis  $\{W_{L\mu}^3, W_{R\mu}^3, V_\mu\}$  is

$$M_{V^0}^2 = \frac{1}{4} \begin{pmatrix} g_L^2(4v_L^2 + v^2) & -g_L g_R v^2 & -4g_L g_{B-L} v_L^2 \\ -g_L g_R v^2 & g_R^2(4v_R^2 + v^2) & -4g_R g_{B-L} v_R^2 \\ -4g_L g_{B-L} v_L^2 & -4g_R g_{B-L} v_R^2 & g_{B-L}^2(4v_R^2 + 4v_L^2) \end{pmatrix}, \quad (2.24)$$

and it is diagonalized by the rotation of gauge fields into physical eigenstates,

$$\begin{pmatrix} W_{L\mu}^3 \\ W_{R\mu}^3 \\ V_\mu \end{pmatrix} = \begin{pmatrix} \cos \theta_W & 0 & \sin \theta_W \\ -\sin \varphi \sin \theta_W & \cos \varphi & \sin \varphi \cos \theta_W \\ -\cos \varphi \sin \theta_W & -\sin \varphi & \cos \varphi \cos \theta_W \end{pmatrix} \begin{pmatrix} Z_{L\mu} \\ Z_{R\mu} \\ A_\mu \end{pmatrix}, \quad (2.25)$$

or in terms of the electromagnetic coupling constant  $e$  and the gauge coupling constants  $g_L, g_R, g_{B-L}$  and  $g_Y$

$$\begin{pmatrix} W_{L\mu}^3 \\ W_{R\mu}^3 \\ V_\mu \end{pmatrix} = \begin{pmatrix} \frac{e}{g_Y} & 0 & \frac{e}{g_L} \\ \frac{-eg_Y}{g_L g_R} & \frac{g_Y}{g_{B-L}} & \frac{e}{g_R} \\ \frac{-eg_Y}{g_L g_{B-L}} & \frac{-g_Y}{g_R} & \frac{e}{g_{B-L}} \end{pmatrix} \begin{pmatrix} Z_{L\mu} \\ Z_{R\mu} \\ A_\mu \end{pmatrix}. \quad (2.26)$$

The relations between mixing angles and coupling constants are given by

$$\begin{aligned} \cos \varphi &= \frac{g_R}{\sqrt{g_R^2 + g_{B-L}^2}}, & \sin \varphi &= \frac{g_{B-L}}{\sqrt{g_R^2 + g_{B-L}^2}}, \\ \cos \theta_W &= \frac{g_L}{\sqrt{g_L^2 + g_R^2 \sin^2 \varphi}}, & \sin \theta_W &= \frac{g_R \sin \varphi}{\sqrt{g_L^2 + g_R^2 \sin^2 \varphi}}, \\ \tan \varphi &= \frac{g_Y}{\sqrt{g_R^2 - g_Y^2}}, \end{aligned} \quad (2.27)$$

and some useful relations

$$\begin{aligned}
g_L &= \frac{e}{\sin \theta_W} \quad , \quad g_Y = \frac{e}{\cos \theta_W} \quad , \\
g_R &= \frac{e}{\sin \varphi \cos \theta_W} \quad , \quad g_{B-L} = \frac{e}{\cos \varphi \cos \theta_W} \quad , \\
g_{B-L} &= \frac{g_Y g_R}{\sqrt{g_R^2 - g_Y^2}} \quad , \quad e = \frac{g_L g_Y}{\sqrt{g_L^2 + g_Y^2}} \quad .
\end{aligned} \tag{2.28}$$

With the VEV hierarchy mentioned before, neutral gauge boson masses read

$$M_{Z_L} \cong \frac{v \sqrt{g_L^2 + g_Y^2}}{2} \quad , \quad M_{Z_R} \cong v_R \sqrt{g_R^2 + g_{B-L}^2} \quad , \quad M_A = 0 \quad . \tag{2.29}$$

Since  $\Phi$  transforms non-trivially under both  $SU(2)_L$  and  $SU(2)_R$ , it mixes the  $W_R$  and  $W_L$  gauge bosons with the following mass-squared matrix in the basis  $\{W_{L\mu}^\pm, W_{R\mu}^\pm\}$

$$M_{V^\pm}^2 = \begin{pmatrix} M_L^2 & M_{LR}^2 \\ M_{LR}^2 & M_R^2 \end{pmatrix} = \frac{1}{4} \begin{pmatrix} g_L^2 (2v_L^2 + v^2) & -2g_L g_R v_u v_d \\ -2g_L g_R v_u v_d & g_R^2 (2v_R^2 + v^2) \end{pmatrix} \quad , \tag{2.30}$$

where the two mass eigenstates  $W_1^\pm$  and  $W_2^\pm$  mix with an orthogonal rotation matrix to construct physical W gauge bosons

$$\begin{pmatrix} W_{1\mu}^\pm \\ W_{2\mu}^\pm \end{pmatrix} = \begin{pmatrix} \cos \xi & e^{-i\omega} \sin \xi \\ -\sin \xi & e^{-i\omega} \cos \xi \end{pmatrix} \begin{pmatrix} W_{L\mu}^\pm \\ W_{R\mu}^\pm \end{pmatrix} \quad , \tag{2.31}$$

here  $\xi$  is a mixing angle which has already some natural bounds on it ( $\xi < 10^{-3}$ ) [4] and  $\omega$  is a phase. The mixing angle and two mass eigenstates in the predefined VEV hierarchy limit are defined by

$$\tan 2\xi = \frac{2M_{LR}^2}{M_L^2 - M_R^2} = \frac{4g_{RL}v_u v_d}{2g_{RL}^2 v_R^2 + (g_{RL}^2 - 1)v^2} \quad , \tag{2.32}$$

$$\begin{aligned}
M_{W_1}^2 &= \frac{g_L^2}{4} [v^2 \cos^2 \xi - 2g_{RL}v_u v_d \sin 2\xi + g_{RL}^2 (2v_R^2 + v^2) \sin^2 \xi] \quad , \\
M_{W_2}^2 &= \frac{g_L^2}{4} [v^2 \sin^2 \xi + 2g_{RL}v_u v_d \sin 2\xi + g_{RL}^2 (2v_R^2 + v^2) \cos^2 \xi] \quad ,
\end{aligned} \tag{2.33}$$

where we have introduced a new parameter  $g_{RL} = g_R/g_L$  (for numerical purposes) and the shorthand notation  $v^2 = v_u^2 + v_d^2$ . Notice that in the case of no mixing ( $\xi \rightarrow 0$ ) the mass eigenstates will exactly be  $M_{W_1} = M_{W_L}$  and  $M_{W_2} = M_{W_R}$ .

$$M_{W_L} = \frac{vg_L}{2} \quad , \quad M_{W_R} = \frac{v_R g_R}{\sqrt{2}} \quad . \quad (2.34)$$

The relation between the masses of  $W$  and  $Z$  bosons are

$$\frac{M_{W_L}}{M_{Z_L}} = \frac{g_L}{\sqrt{g_L^2 + g_Y^2}} = \cos \theta_W \quad , \quad \frac{M_{W_R}}{M_{Z_R}} = \frac{g_R}{\sqrt{2(g_R^2 + g_{B-L}^2)}} = \frac{\cos \varphi}{\sqrt{2}} \quad . \quad (2.35)$$

## 2.2.2 Generation of Fermion Masses in the LRSM

Similar to the SM, three generations of leptons and quarks acquire their masses through Yukawa interactions of Higgs multiplets.

$$\begin{aligned} -\mathcal{L}_{Yukawa} &= \sum y \bar{\psi}_L \Phi \psi_R \\ -\mathcal{L}_{Yukawa} &= \sum_{i,j=1}^3 \left( \bar{L}_{Li} (y_{ij}^L \Phi + \tilde{y}_{ij}^L \tilde{\Phi}) L_{Rj} + \bar{Q}_{Li} (y_{ij}^Q \Phi + \tilde{y}_{ij}^Q Q_{Rj} \tilde{\Phi}) Q_{Rj} \right. \\ &\quad \left. + y_{ij}^\Delta (L_{Li}^T i\sigma_2 \Delta_L L_{Lj} + L_{Ri}^T i\sigma_2 \Delta_R L_{Rj}) \right) + h.c. \quad . \end{aligned} \quad (2.36)$$

$\Phi$  and  $\tilde{\Phi}$  couple to both leptons and quarks, they generate Dirac masses for fermions, and their Yukawa matrices are independent allowing nontrivial quark and lepton mixings in the charged current interactions.  $\Delta_L$  and  $\Delta_R$  only couple to leptons generating light Majorana masses to the left-handed neutrinos and heavy Majorana masses to the right-handed neutrinos according to see-saw mechanism. The Yukawa Lagrangian leads the following Dirac mass matrices for leptons and quarks

$$\begin{aligned} M_\nu &= \frac{1}{\sqrt{2}} (y_{ij}^L v_u + \tilde{y}_{ij}^L v_d) \quad , \quad M_e = \frac{1}{\sqrt{2}} (y_{ij}^L v_d + \tilde{y}_{ij}^L v_u) \quad , \\ M_u &= \frac{1}{\sqrt{2}} (y_{ij}^Q v_u + \tilde{y}_{ij}^Q v_d) \quad , \quad M_d = \frac{1}{\sqrt{2}} (y_{ij}^Q v_d + \tilde{y}_{ij}^Q v_u) \quad , \end{aligned} \quad (2.37)$$

and the Majorana mass matrices for neutrinos

$$M_{\nu_L} = \frac{1}{\sqrt{2}} y_{ij}^\Delta v_L \quad , \quad M_{\nu_R} = \frac{1}{\sqrt{2}} y_{ij}^\Delta v_R \quad . \quad (2.38)$$

These mass matrices can be diagonalized just as in the SM by unitary transformations.

## 2.3 Electroweak Interactions in the LRSM

Electroweak interactions of leptons and quarks arise from the kinetic part of the Lagrangian as in the SM,

$$\begin{aligned}\mathcal{L}_{Kinetic} &= i \sum \bar{\psi} \gamma^\mu D_\mu \psi \\ \mathcal{L}_{Kinetic} &= i \sum_{j=1}^3 \left( \bar{L}_{Lj} \gamma^\mu D_\mu L_{Lj} + \bar{L}_{Rj} \gamma^\mu D_\mu L_{Rj} + \bar{Q}_{Lj} \gamma^\mu D_\mu Q_{Lj} + \bar{Q}_{Rj} \gamma^\mu D_\mu Q_{Rj} \right).\end{aligned}\tag{2.39}$$

Again considering only the first generation of leptons and quarks, Equations (2.6-2.9) lead us to the following electroweak interaction terms

$$\begin{aligned}\mathcal{L}_{Kinetic}^{l,q} &= (\bar{\nu}_e \quad \bar{e})_L \frac{\gamma^\mu}{2} \begin{pmatrix} g_L W_{L\mu}^3 - g_{B-L} V_\mu & \sqrt{2} g_L W_{L\mu}^+ \\ \sqrt{2} g_L W_{L\mu}^- & -g_L W_{L\mu}^3 - g_{B-L} V_\mu \end{pmatrix} \begin{pmatrix} \nu_e \\ e \end{pmatrix}_L \\ &+ (\bar{\nu}_e \quad \bar{e})_R \frac{\gamma^\mu}{2} \begin{pmatrix} g_R W_{R\mu}^3 - g_{B-L} V_\mu & \sqrt{2} g_R W_{R\mu}^+ \\ \sqrt{2} g_R W_{R\mu}^- & -g_R W_{R\mu}^3 - g_{B-L} V_\mu \end{pmatrix} \begin{pmatrix} \nu_e \\ e \end{pmatrix}_R \\ &+ (\bar{u} \quad \bar{d})_L \frac{\gamma^\mu}{2} \begin{pmatrix} g_L W_{L\mu}^3 + \frac{g_{B-L}}{3} V_\mu & \sqrt{2} g_L W_{L\mu}^+ \\ \sqrt{2} g_L W_{L\mu}^- & -g_L W_{L\mu}^3 + \frac{g_{B-L}}{3} V_\mu \end{pmatrix} \begin{pmatrix} u \\ d \end{pmatrix}_L \\ &+ (\bar{u} \quad \bar{d})_R \frac{\gamma^\mu}{2} \begin{pmatrix} g_R W_{R\mu}^3 + \frac{g_{B-L}}{3} V_\mu & \sqrt{2} g_R W_{R\mu}^+ \\ \sqrt{2} g_R W_{R\mu}^- & -g_R W_{R\mu}^3 + \frac{g_{B-L}}{3} V_\mu \end{pmatrix} \begin{pmatrix} u \\ d \end{pmatrix}_R.\end{aligned}\tag{2.40}$$

Substituting the physical eigenstates for the neutral gauge bosons from Equation (2.25) and Equation (2.26), we can simply extract all three electroweak interactions.

### 2.3.1 Electromagnetic Interactions in the LRSM

Massless photons are the mediators of electromagnetic interactions in LRSM as well. Again they only couple to electrically charged fermions with their electric charges. From Equation (2.40) we can read the electromagnetic interactions of fermions

$$\begin{aligned}
\mathcal{L}_{EM} &= \left[ \bar{\nu}_e \frac{\gamma^\mu}{2} \left( g_L \frac{e}{g_L} - g_{B-L} \frac{e}{g_{B-L}} \right) P_L \nu_e + \bar{e} \frac{\gamma^\mu}{2} \left( -g_L \frac{e}{g_L} - g_{B-L} \frac{e}{g_{B-L}} \right) P_L e \right. \\
&+ \bar{u} \frac{\gamma^\mu}{2} \left( g_L \frac{e}{g_L} + \frac{g_{B-L}}{3} \frac{e}{g_{B-L}} \right) P_L u + \bar{d} \frac{\gamma^\mu}{2} \left( -g_L \frac{e}{g_L} + \frac{g_{B-L}}{3} \frac{e}{g_{B-L}} \right) P_L d \\
&+ \bar{\nu}_e \frac{\gamma^\mu}{2} \left( g_R \frac{e}{g_R} - g_{B-L} \frac{e}{g_{B-L}} \right) P_R \nu_e + \bar{e} \frac{\gamma^\mu}{2} \left( -g_R \frac{e}{g_R} - g_{B-L} \frac{e}{g_{B-L}} \right) P_R e \\
&+ \left. \bar{u} \frac{\gamma^\mu}{2} \left( g_R \frac{e}{g_R} + \frac{g_{B-L}}{3} \frac{e}{g_{B-L}} \right) P_R u + \bar{d} \frac{\gamma^\mu}{2} \left( -g_R \frac{e}{g_R} + \frac{g_{B-L}}{3} \frac{e}{g_{B-L}} \right) P_R d \right] A_\mu \\
\mathcal{L}_{EM} &= \left[ \bar{\nu}_e \gamma^\mu (0e) P_L \nu_e + \bar{e} \gamma^\mu (-e) P_L e + \bar{u} \gamma^\mu \left( \frac{2e}{3} \right) P_L u + \bar{d} \gamma^\mu \left( -\frac{e}{3} \right) P_L d \right. \\
&+ \left. \bar{\nu}_e \gamma^\mu (0e) P_R \nu_e + \bar{e} \gamma^\mu (-e) P_R e + \bar{u} \gamma^\mu \left( \frac{2e}{3} \right) P_R u + \bar{d} \gamma^\mu \left( -\frac{e}{3} \right) P_R d \right] A_\mu .
\end{aligned} \tag{2.41}$$

The compact form of electromagnetic interactions is simply written

$$\mathcal{L}_{EM} = e A_\mu J_A^\mu , \tag{2.42}$$

where  $J_A^\mu$  is the electromagnetic current which covers the three flavors of fermions

$$\begin{aligned}
J_A^\mu &= \sum_i Q^i \bar{f}_i \gamma^\mu f_i \\
J_A^\mu &= Q^e \bar{e} \gamma^\mu e + Q^u \bar{u} \gamma^\mu u + Q^d \bar{d} \gamma^\mu d ,
\end{aligned} \tag{2.43}$$

As shown in Figure 6, the Feynman rule of electromagnetic interactions in the LRSM is exactly the same with that of the SM.

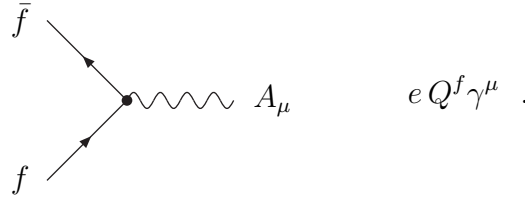


Figure 6: Feynman diagram of electromagnetic interactions in the LRSM.

### 2.3.2 Neutral Current Interactions in the LRSM

Neutral currents in the LRSM are mediated by  $Z_L$  and  $Z_R$  gauge bosons. Mixings of neutral gauge eigenstates ensure that both  $Z_L$  and  $Z_R$  are involved in left and right neutral currents. Following Equation (2.40)

$$\begin{aligned}
\mathcal{L}_{NC} = & \left[ \bar{\nu}_e \frac{\gamma^\mu}{2} (g_L \cos \theta_W + g_{B-L} \cos \varphi \sin \theta_W) P_L \nu_e \right. \\
& + \bar{e} \frac{\gamma^\mu}{2} (-g_L \cos \theta_W + g_{B-L} \cos \varphi \sin \theta_W) P_L e \\
& + \bar{u} \frac{\gamma^\mu}{2} (g_L \cos \theta_W - \frac{g_{B-L}}{3} \cos \varphi \sin \theta_W) P_L u \\
& + \bar{d} \frac{\gamma^\mu}{2} (-g_L \cos \theta_W - \frac{g_{B-L}}{3} \cos \varphi \sin \theta_W) P_L d \\
& + \bar{\nu}_e \frac{\gamma^\mu}{2} (-g_R \sin \varphi \sin \theta_W + g_{B-L} \cos \varphi \sin \theta_W) P_R \nu_e \\
& + \bar{e} \frac{\gamma^\mu}{2} (g_R \sin \varphi \sin \theta_W + g_{B-L} \cos \varphi \sin \theta_W) P_R e \\
& + \bar{u} \frac{\gamma^\mu}{2} (-g_R \sin \varphi \sin \theta_W - \frac{g_{B-L}}{3} \cos \varphi \sin \theta_W) P_R u \\
& + \left. \bar{d} \frac{\gamma^\mu}{2} (g_R \sin \varphi \sin \theta_W - \frac{g_{B-L}}{3} \cos \varphi \sin \theta_W) P_R d \right] Z_{L\mu} \\
& + \left[ \bar{\nu}_e \frac{\gamma^\mu}{2} (g_{B-L} \sin \varphi) P_L \nu_e + \bar{e} \frac{\gamma^\mu}{2} (g_{B-L} \sin \varphi) P_L e \right. \\
& + \bar{u} \frac{\gamma^\mu}{2} (-\frac{g_{B-L}}{3} \sin \varphi) P_L u + \bar{d} \frac{\gamma^\mu}{2} (-\frac{g_{B-L}}{3} \sin \varphi) P_L d \\
& + \bar{\nu}_e \frac{\gamma^\mu}{2} (g_R \cos \varphi + g_{B-L} \sin \varphi) P_R \nu_e + \bar{e} \frac{\gamma^\mu}{2} (-g_R \cos \varphi + g_{B-L} \sin \varphi) P_R e \\
& + \left. \bar{u} \frac{\gamma^\mu}{2} (g_R \cos \varphi - \frac{g_{B-L}}{3} \sin \varphi) P_R u + \bar{d} \frac{\gamma^\mu}{2} (-g_R \cos \varphi - \frac{g_{B-L}}{3} \sin \varphi) P_R d \right] Z_{R\mu} \\
& \tag{2.44}
\end{aligned}$$

$$\begin{aligned}
\mathcal{L}_{NC} = & \left[ \bar{\nu}_e \gamma^\mu \frac{g_L}{\cos \theta_W} \left(\frac{1}{2}\right) P_L \nu_e + \bar{e} \gamma^\mu \frac{g_L}{\cos \theta_W} \left(-\frac{1}{2} + \sin^2 \theta_W\right) P_L e \right. \\
& + \bar{u} \gamma^\mu \frac{g_L}{\cos \theta_W} \left(\frac{1}{2} - \frac{2}{3} \sin^2 \theta_W\right) P_L u + \bar{d} \gamma^\mu \frac{g_L}{\cos \theta_W} \left(-\frac{1}{2} + \frac{1}{3} \sin^2 \theta_W\right) P_L d \\
& + \bar{\nu}_e \gamma^\mu \frac{g_L}{\cos \theta_W} (0) P_R \nu_e + \bar{e} \gamma^\mu \frac{g_L}{\cos \theta_W} (\sin^2 \theta_W) P_R e \\
& + \left. \bar{u} \gamma^\mu \frac{g_L}{\cos \theta_W} \left(-\frac{2}{3} \sin^2 \theta_W\right) P_R u + \bar{d} \gamma^\mu \frac{g_L}{\cos \theta_W} \left(\frac{1}{3} \sin^2 \theta_W\right) P_R d \right] Z_{L\mu} \\
& + \left[ \bar{\nu}_e \gamma^\mu \frac{g_Y}{\tan \varphi} \left(\frac{\tan^2 \varphi}{2}\right) P_L \nu_e + \bar{e} \gamma^\mu \frac{g_Y}{\tan \varphi} \left(\frac{\tan^2 \varphi}{2}\right) P_L e \right. \\
& + \bar{u} \gamma^\mu \frac{g_Y}{\tan \varphi} \left(-\frac{\tan^2 \varphi}{6}\right) P_L u + \bar{d} \gamma^\mu \frac{g_Y}{\tan \varphi} \left(-\frac{\tan^2 \varphi}{6}\right) P_L d \\
& + \bar{\nu}_e \gamma^\mu \frac{g_Y}{\tan \varphi} \left(\frac{1}{2} + \frac{\tan^2 \varphi}{2}\right) P_R \nu_e + \bar{e} \gamma^\mu \frac{g_Y}{\tan \varphi} \left(-\frac{1}{2} + \frac{\tan^2 \varphi}{2}\right) P_R e \\
& + \left. \bar{u} \gamma^\mu \frac{g_Y}{\tan \varphi} \left(\frac{1}{2} - \frac{\tan^2 \varphi}{6}\right) P_R u + \bar{d} \gamma^\mu \frac{g_Y}{\tan \varphi} \left(-\frac{1}{2} - \frac{\tan^2 \varphi}{6}\right) P_R d \right] Z_{R\mu} , \tag{2.45}
\end{aligned}$$



this expression can be summarized in terms of neutral currents

$$\mathcal{L}_{NC} = \frac{g_L}{\cos \theta_W} Z_{L\mu} J_{Z_L}^\mu + \frac{g_Y}{\tan \varphi} Z_{R\mu} J_{Z_R}^\mu , \quad (2.46)$$

where  $J_{Z_L}^\mu$  and  $J_{Z_R}^\mu$  are left and right neutral currents, respectively, covering three generation of fermions and they are defined by

$$\begin{aligned} J_{Z_L}^\mu &= \sum_i (T_L^i P_L - Q^i \sin^2 \theta_W) \bar{f}_i \gamma^\mu f_i , \\ J_{Z_R}^\mu &= \sum_i (T_R^i P_R - \frac{Y_{B-L}^i}{2} \tan^2 \varphi) \bar{f}_i \gamma^\mu f_i . \end{aligned} \quad (2.47)$$

$T_L, T_R$  are left and right weak isospin components,  $Q$  is the electric charge, and  $Y_{B-L}$  the  $B - L$  number of fermion fields. Feynman diagrams of left and right neutral currents in LRSM is given in Figure 7.

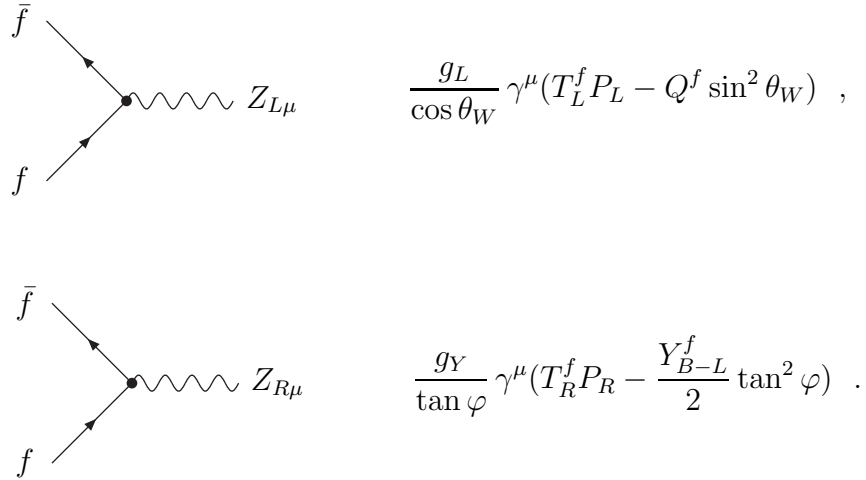


Figure 7: Feynman diagrams of neutral current interactions in the LRSM.

### 2.3.3 Charged Current Interactions in the LRSM

$$\mathcal{L}_{CC} = \frac{g_L}{\sqrt{2}} (W_{L\mu}^- J_{W_L}^\mu + W_{L\mu}^+ J_{W_L}^{\mu\dagger}) + \frac{g_R}{\sqrt{2}} (W_{R\mu}^- J_{W_R}^\mu + W_{R\mu}^+ J_{W_R}^{\mu\dagger}) , \quad (2.48)$$

where  $J_{W_L}^\mu, J_{W_R}^\mu$  are left and right charged currents and  $J_{W_L}^{\mu\dagger}, J_{W_R}^{\mu\dagger}$  are their conjugates. While neutral gauge bosons  $Z_{L,R}$  couple to both left and right handed components of fermions, the charged gauge boson  $W_{L(R)}$  only couples to left(right) handed components of fermions.

$$\begin{aligned}
J_{W_L}^\mu &= \sum_{i,j} (\bar{e}_{Lj} \gamma^\mu \nu_{Li} U_{ij}^{L\dagger} + \bar{d}_{Lj} \gamma^\mu u_{Li} V_{ij}^{L\dagger}) \ , \\
J_{W_L}^{\mu\dagger} &= \sum_{i,j} (\bar{\nu}_{Li} \gamma^\mu e_{Lj} U_{ij}^L + \bar{u}_{Li} \gamma^\mu d_{Lj} V_{ij}^L) \ , \\
J_{W_R}^\mu &= \sum_{i,j} (\bar{e}_{Rj} \gamma^\mu \nu_{Ri} U_{ij}^{R\dagger} + \bar{d}_{Rj} \gamma^\mu u_{Ri} V_{ij}^{R\dagger}) \ , \\
J_{W_R}^{\mu\dagger} &= \sum_{i,j} (\bar{\nu}_{Ri} \gamma^\mu e_{Rj} U_{ij}^R + \bar{u}_{Ri} \gamma^\mu d_{Rj} V_{ij}^R) \ .
\end{aligned} \tag{2.49}$$

In the context of the LRSM both left and right-handed neutrinos can have masses, and they are also subject to mix under proper circumstances. Therefore,  $U^{L,R}$  represent corresponding left and right lepton mixing matrices as well as  $V^{L,R}$  in the quark sector. Since in this thesis we mainly focus on the effects of  $W_R$  gauge boson in the quark sector, we leave the lepton mixing matrices generic without further consideration. We give the Feynman diagram of leptons charged current interactions in Figure 8.

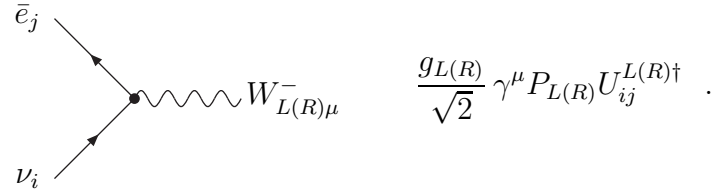


Figure 8: Feynman diagrams of leptons charged current interactions in the LRSM.

where  $U^L$  and  $U^R$  are in generic form

$$U^{L,R} = \begin{pmatrix} U_{\nu_e e} & U_{\nu_e \mu} & U_{\nu_e \tau} \\ U_{\nu_\mu e} & U_{\nu_\mu \mu} & U_{\nu_\mu \tau} \\ U_{\nu_\tau e} & U_{\nu_\tau \mu} & U_{\nu_\tau \tau} \end{pmatrix}_{L,R} \ . \tag{2.50}$$

In the quark sector, the  $W_L$  gauge boson mixes left handed quarks in the same way as in the SM with the same CKM quark mixing matrix ( $V_{CKM}^L$ ). However, the mixing of right handed quarks is left arbitrary in the most general form ( $V_{CKM}^R$ ). In this thesis we will adopt a specific choice for  $V_{CKM}^R$  that is introduced in [5] it is constructed in such a way that it is constrained by some well-known low-energy

phenomenologies. Feynman diagrams of quarks charged current interactions is given in Figure 9.

$$\frac{g_{L(R)}}{\sqrt{2}} \gamma^\mu P_{L(R)} V_{ij}^{L(R)\dagger} .$$

Figure 9: Feynman diagrams of quarks charged current interactions in the LRSM.

### 2.3.4 Right CKM Quark Mixing Matrix

There are several left-right scenarios which appear in the literature for the right-handed CKM matrix;

- In *manifest LR symmetric models* (MLRSM) [6], the CP violation is generated by complex Yukawa couplings, while the VEVs of the Higgs fields remain real. This implies the same mixing for right and left-handed quarks,  $V_{CKM}^R = V_{CKM}^L$ , and equal gauge couplings for  $SU(2)_L$  and  $SU(2)_R$ ,  $g_R = g_L$ .
- In *pseudo-manifest LR symmetry*, both CP and P symmetries are spontaneously broken [7], such that the Yukawa couplings are real. In this case the left and right handed quark mixings are related through  $V_{CKM}^R = V_{CKM}^{L*} K$ , with  $K$  a diagonal phase matrix. Here as well,  $g_R = g_L$ .
- In *asymmetric LR symmetry* (ALRM), left-right symmetry is assumed to be fundamental, superseding the Higgs, Yukawa, or fermion structure [5]. Here arbitrary mixing between the second and third generations, or between the first and third generations are allowed (within unitarity constraints). To simplify the notation, we drop the CKM subscript and, following [5], denote the parametrizations as  $(U_A)$  and  $(U_B)$ , where

$$U_A = \begin{pmatrix} 1 & 0 & 0 \\ 0 & \cos \alpha & \pm \sin \alpha \\ 0 & \sin \alpha & \mp \cos \alpha \end{pmatrix}, \quad U_B = \begin{pmatrix} 0 & 1 & 0 \\ \cos \alpha & 0 & \pm \sin \alpha \\ \sin \alpha & 0 & \mp \cos \alpha \end{pmatrix}, \quad (2.51)$$

with  $\alpha$  an arbitrary angle ( $-\pi/2 \leq \alpha \leq \pi/2$ ). In parametrization  $U_A$ , depending on the values of  $\alpha$ , the dominant coupling could be  $U_{ts}$  while in  $U_B$ , the dominant

coupling could be  $U_{td}$ . The (A) and (B) parametrizations are chosen to allow relaxing the mass limit on  $W_R$  while obeying the restrictions on  $\Delta m_K$  without fine tuning.

The form of the CKM matrix in the right-handed quark sector affects low-energy phenomenology, in particular processes with flavor violation, and thus restricts the mass  $M_{W_R}$  and the mixing angle  $\xi$ . These have been analyzed recently in [8]. (For an alternative analysis, concentrating on the CP violation properties of the model, see Reference [9].)

## 2.4 Higgs Sector in the LRSM

The Higgs sector of the LRSM consists of one bidoublet ( $\Phi$ ) and two triplet ( $\Delta_{L,R}$ ) complex scalar Higgs fields. The right triplet ( $\Delta_R$ ) is responsible for the 1st stage of symmetry breaking

$$SU(2)_L \times SU(2)_R \times U(1)_{B-L} \rightarrow SU(2)_L \times U(1)_Y \quad ,$$

and the bidoublet ( $\Phi$ ) accomplishes the 2nd stage

$$SU(2)_L \times U(1)_Y \rightarrow U(1)_{EM} \quad ,$$

whereas the left triplet ( $\Delta_L$ ) is only present to maintain the discrete parity symmetry in the theory.

$$\Phi = \begin{bmatrix} \Phi_1^0 & \Phi_1^+ \\ \Phi_2^- & \Phi_2^0 \end{bmatrix} \quad , \quad \Delta_L = \begin{bmatrix} \frac{\Delta^+}{\sqrt{2}} & \Delta^{++} \\ \Delta^0 & -\frac{\Delta^+}{\sqrt{2}} \end{bmatrix}_L \quad , \quad \Delta_R = \begin{bmatrix} \frac{\Delta^+}{\sqrt{2}} & \Delta^{++} \\ \Delta^0 & -\frac{\Delta^+}{\sqrt{2}} \end{bmatrix}_R \quad . \quad (2.52)$$

The formation of triplet fields in the form of bidoublets is explained in Appendix A. Neutral component of Higgs fields are expanded around the vacuum as

$$\begin{aligned} \Phi_1^0 &= \frac{v_u + h_1^0 + i\varphi_1^0}{\sqrt{2}} \quad , \quad \Phi_2^0 = \frac{v_d + h_2^0 + i\varphi_2^0}{\sqrt{2}} \quad , \\ \Delta_L^0 &= \frac{v_L + h_L^0 + i\varphi_L^0}{\sqrt{2}} \quad , \quad \Delta_R^0 = \frac{v_R + h_R^0 + i\varphi_R^0}{\sqrt{2}} \quad . \end{aligned} \quad (2.53)$$

There are four neutral scalar, four neutral pseudo scalar, four singly charged scalar and two doubly charged scalar Higgs fields in the theory. They mix appropriately with unitary transformations to construct the physical Higgs spectrum of the LRSM.

- Neutral Scalars

$$\begin{aligned} (S_i^0)^T &= (h_1^0 \ h_2^0 \ h_L^0 \ h_R^0) \ , \\ (H_i^0)^T &= (H_1^0 \ H_2^0 \ H_3^0 \ H_4^0) \ . \end{aligned} \quad (2.54)$$

- Neutral Pseudo Scalars

$$\begin{aligned} (P_i^0)^T &= (\varphi_1^0 \ \varphi_2^0 \ \varphi_L^0 \ \varphi_R^0) \ , \\ (A_i^0)^T &= (A_1^0 \ A_2^0 \ G_1^0 \ G_2^0) \ . \end{aligned} \quad (2.55)$$

- Singly Charged Scalars

$$\begin{aligned} (C_i^+)^T &= (\Phi_1^+ \ \Phi_2^{-*} \ \Delta_L^+ \ \Delta_R^+) \ , \\ (H_i^+)^T &= (H_1^+ \ H_2^+ \ G_1^+ \ G_2^+) \ . \end{aligned} \quad (2.56)$$

- Doubly Charged Scalars

$$\begin{aligned} (D_i^{++})^T &= (\Delta_L^{++} \ \Delta_R^{++}) \ , \\ (H_i^{++})^T &= (H_1^{++} \ H_2^{++}) \ . \end{aligned} \quad (2.57)$$

Gauge and physical eigenstates are related with unitary transformations which satisfy unitarity relations

$$\begin{aligned} H_i^0 &= (Z_S)_{ij} S_j^0 \quad , \quad (Z_S)(Z_S)^\dagger = \sum_{i,j,k=1}^4 [(Z_S)_{ik}(Z_S)_{jk}^*] = \delta_{ij} \ , \\ A_i^0 &= (Z_P)_{ij} P_j^0 \quad , \quad (Z_P)(Z_P)^\dagger = \sum_{i,j,k=1}^4 [(Z_P)_{ik}(Z_P)_{jk}^*] = \delta_{ij} \ , \\ H_i^+ &= (Z_C)_{ij} C_j^+ \quad , \quad (Z_C)(Z_C)^\dagger = \sum_{i,j,k=1}^4 [(Z_C)_{ik}(Z_C)_{jk}^*] = \delta_{ij} \ , \\ H_i^{++} &= (Z_D)_{ij} D_j^{++} \quad , \quad (Z_D)(Z_D)^\dagger = \sum_{i,j,k=1}^2 [(Z_D)_{ik}(Z_D)_{jk}^*] = \delta_{ij} \ . \end{aligned} \quad (2.58)$$

These rotation matrices ( $Z_S, Z_P, Z_C$  and  $Z_D$ ) are basically diagonalizing matrices of corresponding Higgs mass matrices which are constructed from the minimization of the Higgs potential. We will not give further details of rotation matrices and the minimization of the potential since they are out of the scope of this thesis.

# Chapter 3

## B DECAYS IN THE LRSM

Within the next decade, significant progress is expected in experimental high energy physics. Most of the hope rests on the LHC, expected to probe the SM of electroweak interactions and models beyond it. The experimental explorations would complement efforts made by theorists over the last decades. The common wisdom held that while the SM left some fundamental questions unanswered (such as stability of the Higgs mass, the origin of CP violation, the baryon asymmetry, or the presence of dark matter in the universe), it was experimentally sound. Several precision measurements have recently questioned the latter. First and foremost, there was evidence for the existence of neutrino masses and mixing, inconsistent with the SM predictions, where neutrinos are assumed massless. Some of recent experimental results, which might prove (at least) difficult to explain within the SM, and provide some hints of deviations from its predictions come mostly from  $B$  physics. The values of the angle  $\phi_1$  measured in some penguin process  $b \rightarrow sq\bar{q}$  and the precisely measured value in  $B \rightarrow J/\psi K_S^0$  differ by two to three standard deviations ( $B_0 \rightarrow \pi^0\pi^0 K_S^0, B_0 \rightarrow K^+K^-K^0$ , [10–12]) and may suggest the existence of a new CP phase in this penguin-dominated process; the lepton forward-backward asymmetry in  $B \rightarrow K^*l^+l^-$  is measured to be around two standard deviations higher than the SM prediction [13]; direct CP asymmetries in  $B_0 \rightarrow K^+\pi^-$  and  $B^+ \rightarrow K^+\pi^0$  differ significantly from each other, although naively one would expect them to be the same [14]; the branching fraction for  $B^+ \rightarrow \tau\nu$  is up to two standard deviations higher than expected, depending on the theoretical input chosen [10, 15]; in purely leptonic  $D_s^+ \rightarrow \mu\nu$  and  $D_s^+ \rightarrow \tau\nu$  decays the deviation of the branching ratios is even larger [16, 17] if one uses the recent lattice QCD

calculations of the meson decay constant; the measured production cross-section for  $c\bar{c}$  states is higher than the calculated one [18]. A careful analysis combining all the experimental data on  $B_s$  mixing [19] finds that the phase of the mixing amplitude deviates by about  $3\sigma$  from the SM prediction (or slightly less, if one does not use Gaussian error distributions) [20, 21].

Additionally, the CDF and DØ experiments have determined a sizable forward-backward asymmetry in top anti-top events, in which one top decays semileptonically, a measurement that is more than a  $2\sigma$  deviation from the SM prediction [22].

Taken together, these indicate that flavor and CP physics are highly non-trivial and that they may be governed by a new paradigm beyond the single CKM matrix of the SM. Possibilities for non-SM flavor violation are present in the  $b \rightarrow d, s$  non-leptonic decays. This justifies looking at rare B decays in new physics scenarios.

Perhaps the simplest such scenario of models beyond the SM is the left-right symmetric model [2, 3, 6, 23–25]. Motivated originally by the desire to understand parity violation in weak interactions [6, 26], it gathered some more support due to its simplicity. It appears to be a natural extension of the SM, as it treats both left- and right-handed fermions as doublets. Additionally the model gauges the  $B - L$  quantum number, left ungauged in the SM, and it provides an elegant explanation of neutrino masses through the see-saw mechanism [27–38].

In this thesis we are going to focus on a specific scenario proposed by Langacker and Sankar [5] in which the right CKM quark mixing matrix (RCKM) is formulated as in Equation (2.51). The authors assume the LR symmetry to be fundamental, superseding the Higgs, Yukawa or fermion structure, and analyze constraints on the charged gauge boson masses and mixings including a variety of constraints, coming from the Kaon system, the  $B_d^0 - \bar{B}_d^0$  mixing,  $b \rightarrow X\nu_e e$ , universality, muon decays and neutrinoless double beta decays. They consider several neutrino masses scenarios (Dirac or Majorana, light, intermediate or heavy) and allow for  $g_R \neq g_L$  as well as  $V_{CKM}^R \neq V_{CKM}^L$ . The form chosen for the  $V_{CKM}^R$  is not arbitrary, nor is it the most general form for a  $3 \times 3$  mixing matrix one could write down. The choice for right-handed quark mixings is particularly attractive, as it is motivated by the  $K^0 - \bar{K}^0$  mass difference, which is strongly affected by the right-handed quark mixing matrix, and it depends on one parameter only, making it highly predictive. Their requirement

is that  $M_{W_R}$  be as general as possible, and the form of  $V_{CKM}^R$  not be excessively fine-tuned. An additional reason to revisit this parametrization is that a recent analysis of CP violation in Pati-Salam type LR models [39] concludes that manifest/pseudo-manifest left-right models are disfavored, unless they include an unnaturally large CP violating phase.

The aim of this chapter is to investigate the consequences of the RCKM parametrizations in ALRM on  $b \rightarrow d, s$  transitions, concentrating at first on the CP-conserving, flavor violating processes  $b \rightarrow s\gamma$  ( $\Delta B = 1$ ) and  $B_{d,s}^0 - \bar{B}_{d,s}^0$  mixing ( $\Delta B = 2$ ). Although the experimental data for these agrees with the predictions of the SM, we use the analysis to establish consistency of the model parameters.

Our motivation is two-fold. First, flavor and CP violation in B decays have received a lot of theoretical and experimental interest recently, and careful analysis, as outlined before, show deviations from the SM predictions. Agreement with the branching ratio for  $b \rightarrow s\gamma$  is the cornerstone of any model beyond the SM. LHCb will uncover many new exciting results in B physics and may rule out certain models, as might a new (under discussion) Super KEKB factory. Second, strong flavor violation (which could come from the right-handed quarks in ALRM) has implications for new particles and interactions at the LHC, notable for new charged gauge bosons, which have received less attention than their neutral counterparts.

The analysis presented here follows several previous analysis of B decays in LR models [40–44]. Although many discussions of the manifest or pseudo-manifest model exist, very few are available for more general LR models. Our numerical analysis is more detailed and comprehensive than in previous works and clearly separates regions for all parameters of LR models that are ruled out by existing measurements. As we were unable to find equally extensive discussions of manifest or pseudo-manifest LRSM, we include a comparison with these models as well, and give the relevant values in the SM. Additionally, we have performed the analysis using well-established publicly available software, which allows exact numerical evaluations without using additional assumptions. As we had to modify the software to include evaluation of the box diagrams, we explain the modifications in Appendix D and give the relevant formulas.

In the ALRM, the LR symmetry of the Lagrangian is seen as more fundamental than the Higgs, Yukawa or fermion structure. The left- and right-handed quark



mixing are independent of each other and are fixed by experimental constraints from low energy physics. The mixing matrix for left-handed quarks is the known CKM matrix, while for right-handed quarks the mixing matrix is chosen to satisfy the Kaon ( $K^0 - \bar{K}^0$  mixing,  $\epsilon_K$ ) meson constraints. This fixes the mixing between the first two families (to be either minimal or maximal), allowing for arbitrary mixing between the second and third, or the first and third families, parametrized as  $U_A$  and  $U_B$  as in Equation (2.51). The consequences of the ALRM have received less attention [5], and we propose to investigate them here in  $b \rightarrow s, d$  transitions.

LR models are best constrained at low energies by flavor-changing mixings and decays as well as by the CP violating observables. In what follows, we will work with the  $U_A$  and  $U_B$  parametrizations (denoted simply by  $U$ ) and compare our results with the MLRSM where possible. The restrictions on these parametrizations in the  $K_L - K_S$  mixing have been thoroughly examined [5, 45–51], and the experimental limits imply

$$\left(\frac{g_R M_{W_1}}{g_L M_{W_2}}\right)^2 \leq 0.075, \quad \text{or} \quad \frac{g_L}{g_R} M_{W_2} \geq 300 \text{ GeV} \quad ,$$

with  $M_{W_1}, M_{W_2}$  the masses of the charged gauge bosons in Equation (2.33). These restrictions still hold, as the experimental data on Kaon physics did not change significantly over the years. However, we need to carefully re-examine the constraints on the model parameters coming from B physics, in light of the new measurements. We proceed first with the analysis of the  $\Delta B = 1$  flavor-changing decays, and follow in the next subsection with  $\Delta B = 2$  processes. Both  $\Delta B = 1$  and  $\Delta B = 2$  processes are generated by the same Lagrangian, which is responsible for flavor changing.

The charged current interactions for general B decays in the 't Hooft-Feynman gauge are,

$$\begin{aligned} \mathcal{L}_{CC}^W &= -\frac{1}{\sqrt{2}} \bar{u}_i \gamma^\mu [g_L c_\xi V_{ij} P_L + g_R e^{-i\omega} s_\xi U_{ij} P_R] d_j W_{1\mu}^+ \\ &\quad + \frac{1}{\sqrt{2}} \bar{u}_i \gamma^\mu [g_L e^{i\omega} s_\xi V_{ij} P_L - g_R c_\xi U_{ij} P_R] d_j W_{2\mu}^+ \quad , \end{aligned} \quad (3.1)$$

for the  $W_{1,2}$  bosons and for the charged Higgs fields

$$\begin{aligned} \mathcal{L}_{CC}^H &= -\frac{\sin 2\beta}{\cos 2\beta} N_H \bar{u}_i [M_{u_i} V_{ij} P_L - M_{d_j} V_{ij} P_R] d_j H^+ \\ &\quad - \frac{1}{\cos 2\beta} N_H \bar{u}_i [M_{u_i} U_{ij} P_R - M_{d_j} U_{ij} P_L] d_j H^+ \quad , \end{aligned} \quad (3.2)$$

with

$$N_H = \left[ v_u^2 + v_d^2 + \frac{(v_u^2 - v_d^2)^2}{2v_R^2} \right]^{-\frac{1}{2}}, \quad (3.3)$$

and  $\tan \beta = \frac{v_u}{v_d}$ . Note that there is a neutral Higgs boson which can violate flavor. This Higgs boson must be heavy to obey Flavor-Changing Neutral Currents (FCNC) bounds (of order 30–50 TeV or heavier [52], so we will *a-priori* neglect its contribution here). Finally the interactions corresponding to the charged Goldstone bosons  $G_{1,2}$  are

$$\begin{aligned} \mathcal{L}_{CC}^G = & - \frac{1}{\sqrt{2}M_{W_1}} \bar{u}_i \left[ (g_L c_\xi M_{u_i} V_{ij} - g_R s_\xi M_{d_i} U_{ij}) P_L \right. \\ & \left. - (g_L c_\xi M_{d_i} V_{ij} - g_R s_\xi M_{u_i} U_{ij}) P_R \right] d_j G_1^+ \\ & + \frac{1}{\sqrt{2}M_{W_2}} \bar{u}_i \left[ (g_L s_\xi M_{u_i} V_{ij} + g_R c_\xi M_{d_i} U_{ij}) P_L \right. \\ & \left. - (g_L s_\xi M_{d_i} V_{ij} + g_R c_\xi M_{u_i} U_{ij}) P_R \right] d_j G_2^+ . \end{aligned} \quad (3.4)$$

In all the above formulas  $u_i(d_i)$  denotes up(down)-type quarks,  $M_{u_i(d_i)}$  are their respective masses, and  $P_{L,R} = (1 \mp \gamma^5)/2$  are the left and right handed projection operators.

### 3.1 $b \rightarrow s\gamma$ Decay

The inclusive rate  $B \rightarrow X_s \gamma$  has been measured precisely to 10% [53,54]  $BR_{\text{Exp}}(B \rightarrow X_s \gamma) = (3.55 \pm 0.23) \times 10^{-4}$ . The rate has been calculated in SM to  $\mathcal{O}(\alpha_s^2)$  with the remaining uncertainty 7% [55]  $BR_{\text{SM}}(B \rightarrow X_s \gamma) = (3.15 \pm 0.23) \times 10^{-4}$ . While the difference is not too large, the window between the measurement and the SM can be used to severely constrain new physics.

The decay  $b \rightarrow s\gamma$  has been considered by numerous authors in the context of manifest or pseudo-manifest left-right models [40–44]. Basically, this is a one-loop flavor changing neutral current process, proceeding through an electromagnetic penguin diagram, with up-type quarks and charged bosons in the loop. The low-energy effective Hamiltonian for  $b \rightarrow s\gamma$  in the operator product expansion (OPE) is written as

$$\mathcal{H}_{eff}^{(\Delta B=1)} = \frac{4G_F}{\sqrt{2}} \left[ (V_{jb}V_{js}^*) C_L^7 O_L^7 + g_{RL}^2 (U_{jb}U_{js}^*) C_R^7 O_R^7 \right], \quad (3.5)$$

where the operators are

$$O_L^7 = \frac{e M_b}{16\pi^2} (\bar{s} \sigma^{\mu\nu} P_R b) F_{\mu\nu} \quad , \quad O_R^7 = \frac{e M_b}{16\pi^2} (\bar{s} \sigma^{\mu\nu} P_L b) F_{\mu\nu} \quad , \quad (3.6)$$

with  $F_{\mu\nu}$  the electromagnetic field tensor. All relevant one-loop Feynman diagrams are given in Figure 10.

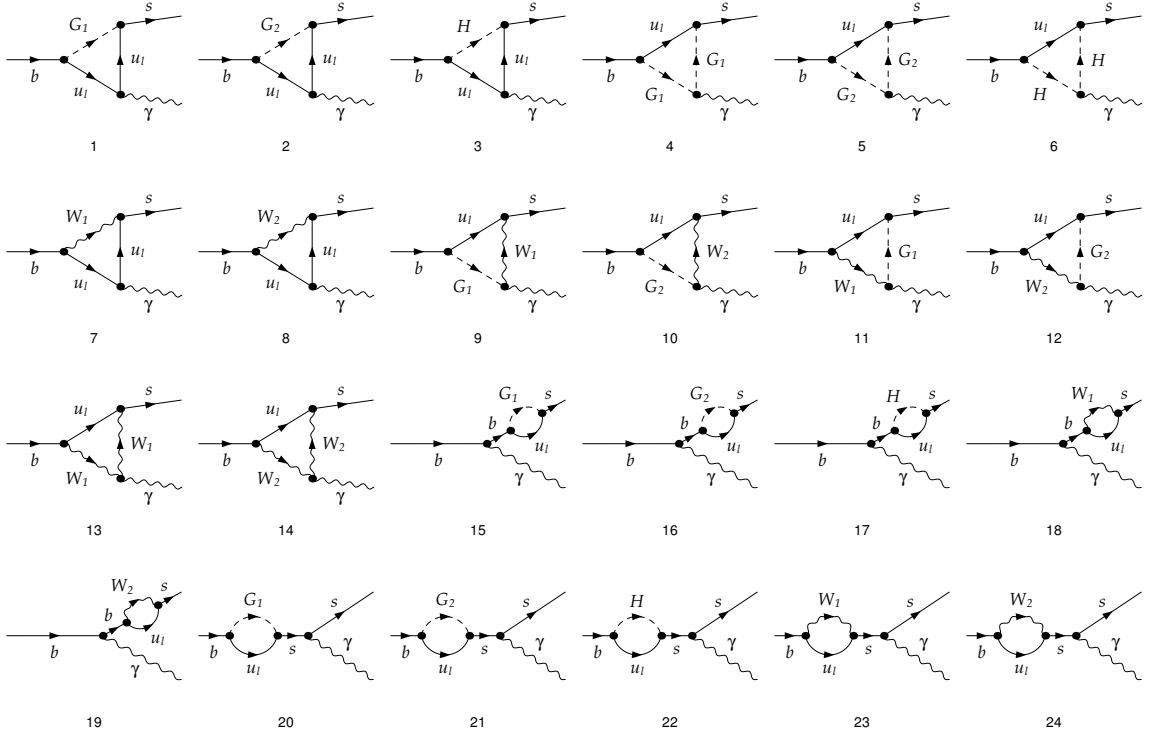


Figure 10: Triangle and self-energy diagrams contributing to the  $b \rightarrow s \gamma$  transition.

We used `FeynArts` [56, 57] for generating the amplitudes, then `FormCalc` and `LoopTools` [58, 59] packages to evaluate the loop contributions  $C_L^7$  and  $C_R^7$  numerically. The dominant contribution to  $\Gamma(b \rightarrow s \gamma)$  comes from the top-quark in the loop, so below we give the analytical expressions for the top-quark contribution. The coefficients of pure left, pure right, and LR interference are encoded in  $C_L^7$  and  $C_R^7$  ;

$$\begin{aligned}
C_L^7 &= c_\xi^2 A_{SM}(x_1) + s_\xi^2 A_{SM}(x_2) + s_{2\xi} g_{RL} \frac{M_t U_{tb}}{M_b V_{tb}} \sum_{i=1}^2 A_{LR}(x_i) \\
&+ \frac{s_{2\beta}}{c_{2\beta}^2} \frac{M_t U_{tb}}{M_b V_{tb}} A_{H^+}^1(y) + t_{2\beta}^2 A_{H^+}^2(y) \quad , \quad (3.7)
\end{aligned}$$

$$\begin{aligned}
C_R^7 &= s_\xi^2 g_{RL}^2 A_{RH}(x_1) + c_\xi^2 g_{RL}^2 A_{RH}(x_2) + s_{2\xi} g_{RL} \frac{M_t V_{tb}}{M_b U_{tb}} \sum_{i=1}^2 A_{LR}(x_i) \\
&+ \frac{s_{2\beta}}{c_{2\beta}^2} \frac{M_t V_{tb}}{M_b U_{tb}} A_{H^+}^1(y) + \frac{1}{c_{2\beta}^2} A_{H^+}^2(y) \quad , \quad (3.8)
\end{aligned}$$

where the arguments of the functions are  $x_i = (M_t/M_{W_i})^2$ ,  $y = (M_t/M_{H^\pm})^2$ . The loop integrals  $A_{SM}$ ,  $A_{RH}$ ,  $A_{LR}$  and  $A_{H^+}^{1,2}$  are calculated numerically in terms of scalar and tensor coefficient functions. The QCD corrections arising from the evolution of the effective Hamiltonian down to  $\mu = M_b$  scale are

$$\begin{aligned}
C_L^{7(eff)} &= \eta^{-16/23} \left[ C_L^7 + \frac{3}{10} X(\eta^{10/23} - 1) + \frac{3}{28} X(\eta^{28/23} - 1) \right] \quad , \\
C_R^{7(eff)} &= \eta^{-16/23} C_R^7 \quad , \quad (3.9)
\end{aligned}$$

with  $X = \frac{208}{81}$  and  $\eta = \frac{\alpha_s(M_b)}{\alpha_s(M_{W_1})} \simeq 1.8$ . In the calculation of the branching ratio we have followed the traditional method of scaling the decay width  $\Gamma(b \rightarrow s\gamma)$  with the semileptonic decay width  $\Gamma(b \rightarrow ce\bar{\nu})$  [60]

$$BR(b \rightarrow s\gamma) = \frac{\Gamma(b \rightarrow s\gamma)}{\Gamma(b \rightarrow ce\bar{\nu})} \times BR(b \rightarrow ce\bar{\nu}) \quad , \quad (3.10)$$

we calculated the width  $\Gamma(b \rightarrow ce\bar{\nu})$  in our model and for the branching ratio we used the well-established value  $BR(b \rightarrow ce\bar{\nu}) \simeq 11\%$  [17].

In Figure 11 we present the dependence of the branching ratio of  $b \rightarrow s\gamma$  in a contour plot in  $M_{W_2} - \sin \alpha$  plane, with  $U_{ts} = \sin \alpha$  in the  $V_{CKM}^R = U_A$  parametrization. (Note that in  $V_{CKM}^R = U_B$  the contribution to the right-handed quark mixings to  $b \rightarrow s$  processes is zero). Fixing the mass of the charged Higgs boson to  $M_{H^\pm} = 10$  TeV<sup>1</sup>, we consider various  $\tan \beta$  and  $g_{RL}$  values. While we allow the ratio of  $g_{RL}$  to vary, it is not allowed to have arbitrary values. As  $SU(2)_R \times U(1)_{B-L}$  breaks to  $U(1)_Y$ , the coupling constants of the three groups  $g_R$ ,  $g_{B-L}$  and  $g_Y$  are related (see Equation (2.28)), requiring  $g_{RL} > \tan \theta_W$ . For coupling ratios outside this interval, the  $Z_R f \bar{f}$  coupling becomes non-perturbative. We restrict the branching ratio

<sup>1</sup>As required by the  $B^0 - \bar{B}^0$  mixing, see discussion in the next subsection.

to be within the experimentally allowed values in the  $1\sigma$  range, and the allowed regions are shaded in yellow, with upper values in red. The lower bound value is always allowed by the parameter space chosen. As the SM value in our calculation is  $\text{BR}(b \rightarrow s\gamma) = 3.2 \times 10^{-4}$ , the region in which  $\sin \alpha = 0$ , which corresponds to no contribution from the right-handed side, is always included in the allowed parameter space.

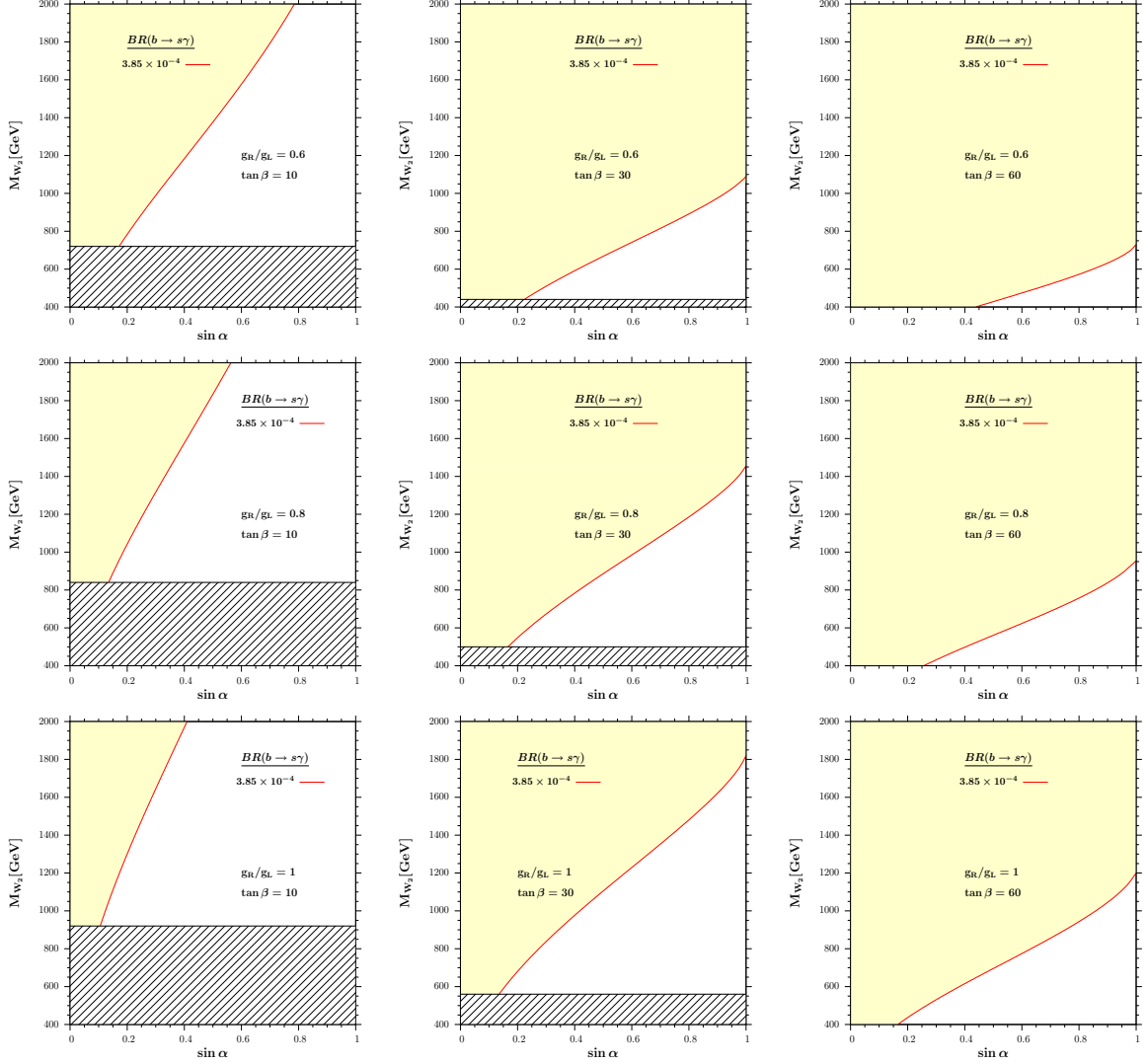


Figure 11: Contour plot of the  $M_{W_2}$  vs  $\sin \alpha$  constraint in the  $U_A$  parametrization, from  $b \rightarrow s\gamma$ . We fix the  $\text{BR}(b \rightarrow s\gamma)$  to be in the interval  $(3.20 - 3.85) \times 10^{-4}$ , and vary  $g_{RL}$  and  $\tan \beta$ , as indicated in the panels. We take  $M_{H^\pm} = 10$  TeV. Black-shaded regions represent areas excluded by the  $W_R - W_L$  mixing angle  $\xi \leq 3 \times 10^{-3}$ . Regions highlighted in yellow represent allowed parameter spaces.

The  $g_{RL}$  value is kept constant along the rows of the graphs in Figure 11. These values are  $g_{RL} = 0.6, 0.8$  and  $1$  for the first, second and third row, respectively. We vary  $\tan \beta$  between  $10$  and  $60$  among the panels. Increasing  $\tan \beta$  for a fixed  $g_{RL}$  value widens the allowed parameter space for  $U_{ts} = \sin \alpha$ . The reason is that, for  $\tan \beta \geq 5$ , the dominant Higgs contribution is proportional to  $1/\cos^2 2\beta$ . This contribution increases with  $\tan \beta$  and thus requires a larger compensating  $W_2$  contribution, thus enlarging the parameter space allowed to satisfy the experimental bounds. Taking  $\tan \beta \rightarrow 0$  and  $M_{W_2} \rightarrow \infty$  does not reduce the model to the SM for the chosen Higgs mass; one would also need to take  $M_{H^\pm} \rightarrow \infty$  limit to recover the SM. Going down the plots along the columns of Figure 11, we investigate the effects of varying the ratio  $g_{RL}$ . For low  $\tan \beta$ , the parameter regions available for  $U_{ts} = \sin \alpha$  are reduced because one effectively increases the contribution of  $W_2$  for a fixed Higgs contribution; while increasing  $\tan \beta$  increases the Higgs contribution, opening more parameter space for  $U_{ts} = \sin \alpha$ . The region shaded is excluded by the restriction on the  $W_R - W_L$  mixing angle,  $\xi < 3 \times 10^{-3}$ . In conclusion, Figure 11 shows that large values of  $\tan \beta$  insure that a large parameter space for  $V_{ts}^R = \sin \alpha$  is allowed as  $M_{W_2}$  gets larger; while smaller values of  $g_{RL}$  allow larger flavor violation in the right-handed sector, even for low  $W_2$  masses.

For comparison, we investigate the same dependence in the MLRSM in Figure 12. There is not  $\sin \alpha$  dependence there, as the flavor violation in the right-handed sector is fixed; and so is  $g_R = g_L$ . As in our model, large  $\tan \beta$  allows for a larger parameter space. The main difference lies in the fact that in MLRSM  $V_{ts}^R \sim \mathcal{O}(10^{-2})$  while in our model,  $U_{ts} = \sin \alpha$  is allowed to vary and be large. Thus in the MLRSM the contribution for  $W_2$  is relatively smaller, allowing for contributions from lighter charged Higgs. The  $W_2$  mass is required to be at least  $1$  TeV for  $\tan \beta = 10$ , while for  $\tan \beta = 60$ , the  $W_2$  mass is allowed to be as light as  $500$  GeV. Higgs masses of  $1$  TeV are ruled out for  $M_{W_2} < 2$  TeV for  $\tan \beta = 10$ , but not for  $\tan \beta = 60$ . In both cases, the Higgs contribution decouples for  $M_{H^\pm} \geq 5$  TeV, while no such statement can be made in our model when both  $U_{ts}$  and  $g_{RL}$  are allowed to vary.

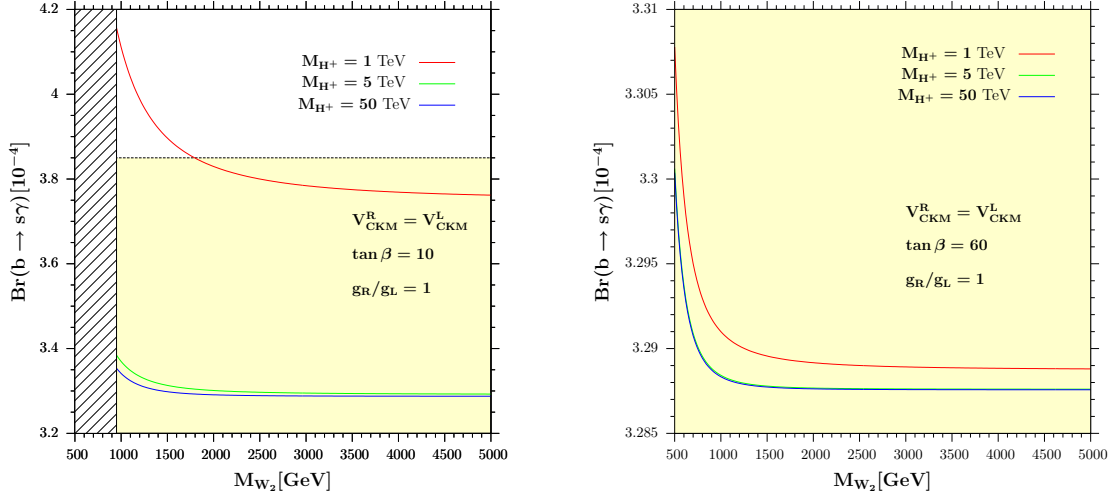


Figure 12:  $\text{BR}(b \rightarrow s\gamma)$  as a function of the  $W_2$  mass in the MLRSM,  $V_{CKM}^R = V_{CKM}^L$ . We take  $\tan\beta = 10$  in the left panel and  $\tan\beta = 60$  in the right panel. The curves in red, green and blue correspond to, respectively  $M_{H^\pm} = 1, 5$  and  $50$  TeV. Yellow highlighted regions represent allowed spaces; the black shaded region is excluded by the  $W_L - W_R$  mixing angle.

In Figure 13 we investigate the dependence of the branching ratio of  $b \rightarrow s\gamma$  on the  $H^\pm$  mass and  $\tan\beta$  in the  $U_A$  parametrization. We fix the mass  $M_{W_2} = 500$  GeV (as we are interested in the consequences of a light gauge boson) and vary  $U_{ts} = \sin\alpha$  and  $g_{RL}$ . We again restrict the branching ratio to be within  $1\sigma$  range and give contour plots for the allowed regions (highlighted in yellow, with upper values in red; as before, lower values are always allowed in the chosen parameter space). For each of the rows of plots in Figure 13 we keep  $g_{RL}$  constant and choose values for  $U_{ts} = \sin\alpha$ . For fixed ratios of  $g_{RL}$ , increasing  $\sin\alpha$  shifts the allowed parameter space to higher values of  $\tan\beta$ , and this result is independent of  $M_{H^\pm}$ . The result is in complete agreement with our observations on the  $\tan\beta$  influence in Figure 11, where the Higgs contribution was needed to compensate for a large flavor mixing in the right-handed sector. Going down the columns of Figure 13, we analyze the effects of varying  $g_{RL}$ . The second row shows that for larger  $g_{RL}$  ratio the allowed parameter regions are moving towards larger  $\tan\beta$ . For the last row, where  $g_{RL} = 1$ , the allowed region of the parameter space is extremely sensitive to  $\sin\alpha$ , and consistent with the data only for very small values for  $U_{ts} = \sin\alpha$ . Even for relatively small right-handed flavor violation,  $\sin\alpha = 0.25$ , most of the region of the parameter space is ruled

out. Here the contribution from the right-handed gauge boson is large, large flavor violation requires a very large Higgs term contribution, and even large values of  $\tan\beta$  are insufficient to generate compensating terms. Here again, the region shaded is excluded by the restriction of the  $W_R - W_L$  mixing angle  $\xi < 3 \times 10^{-3}$ ; this region depends only on the ratio  $g_{RL}$ .

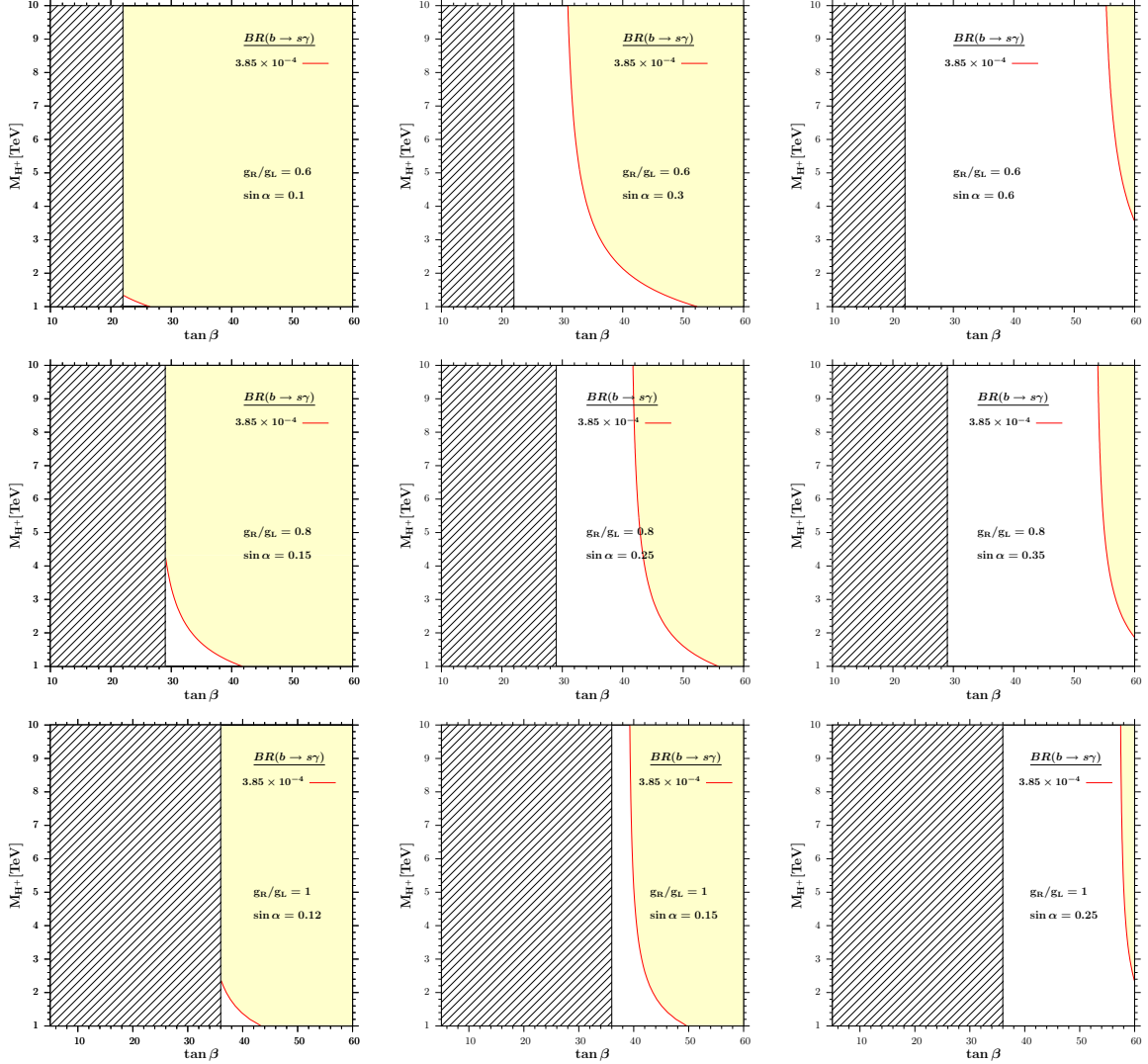


Figure 13: Contour plot of the  $M_{H^\pm}$  vs  $\tan\beta$  constraint in the  $U_A$  parametrization, for  $b \rightarrow s\gamma$ . We fix the branching ratio to be in the interval  $(3.20 - 3.85) \times 10^{-4}$ , and vary  $g_{RL}$  and  $\sin\alpha$ , as indicated in the panels. We take  $M_{W_2} = 500$  GeV. Shaded regions represent areas excluded by the  $W_R - W_L$  mixing angle  $\xi \leq 3 \times 10^{-3}$ . Regions highlighted in yellow represent allowed parameter spaces.



In conclusion, we see from Figure 13 that larger values of  $\tan \beta$  and smaller values of  $g_{RL}$  satisfy the  $b \rightarrow s\gamma$  branching ratio constraints for a wide parameter space for  $M_{H^\pm}$ , while low values for  $U_{ts} = \sin \alpha$  are required for low  $W_2$  masses.

Following previous studies, we do not analyze  $b \rightarrow d\gamma$  transitions. Finding new physics effects in the  $b \rightarrow d$  may be easier than in the  $b \rightarrow s$  one because the SM amplitude is suppressed in the  $b \rightarrow d$  transition. In the SM,  $b \rightarrow s\gamma$  and  $b \rightarrow d\gamma$  are both described by a common Wilson coefficient,  $C_L^7$ . This is also true in any model within a minimal flavor violating framework in which the flavor-changing interactions are determined by the left-CKM angles. However, the experimental measurement for  $b \rightarrow d\gamma$  is not very precise [61–63]  $BR_{\text{Exp}}(b \rightarrow d\gamma) = (1.63_{-0.24}^{+0.30} \pm 0.16) \times 10^{-6}$ . Since the SM predictions for exclusive modes such as  $B \rightarrow \rho\gamma$  or  $B \rightarrow \omega\gamma$  [61–63] suffer from large model-dependent uncertainties, it is necessary to measure the inclusive rate for  $B \rightarrow X_d\gamma$ . The largest experimental challenge is the huge background due to  $b \rightarrow s\gamma$ . The only possible way is probably to sum up exclusive  $b \rightarrow d\gamma$  modes, perhaps from Belle and KEKB.

### 3.2 $B_{d,s}^0 - \bar{B}_{d,s}^0$ Mixing

The  $\Delta B = 2$  flavor-changing decays have been studied in the context of minimal left-right symmetric models [64–68]. The mass difference between  $B_q^0$  and  $\bar{B}_q^0$  is defined by

$$\Delta m_q = \frac{|\langle B_q^0 | H_{eff}^{\Delta B=2} | \bar{B}_q^0 \rangle|}{m_{B_q}} . \quad (3.11)$$

The effective Hamiltonian  $H_{eff}^{(\Delta B=2)}$  for the  $B^0 - \bar{B}^0$  transition is obtained by integrating out the internal loop in the box diagrams responsible for this process.

$$H_{eff}^{(\Delta B=2)} = \sum_i^6 C_i Q_i + \sum_i^3 \tilde{C}_i \tilde{Q}_i , \quad (3.12)$$

with the following four-quark operators

$$\begin{aligned}
Q_1 &= (\bar{q}^\alpha \gamma^\mu P_L b^\alpha) \otimes (\bar{q}^\beta \gamma_\mu P_L b^\beta) , & \tilde{Q}_1 &= (\bar{q}^\alpha \gamma^\mu P_R b^\alpha) \otimes (\bar{q}^\beta \gamma_\mu P_R b^\beta) , \\
Q_2 &= (\bar{q}^\alpha P_L b^\alpha) \otimes (\bar{q}^\beta P_L b^\beta) , & \tilde{Q}_2 &= (\bar{q}^\alpha P_R b^\alpha) \otimes (\bar{q}^\beta P_R b^\beta) , \\
Q_3 &= (\bar{q}^\alpha P_L b^\beta) \otimes (\bar{q}^\beta P_L b^\alpha) , & \tilde{Q}_3 &= (\bar{q}^\alpha P_R b^\beta) \otimes (\bar{q}^\beta P_R b^\alpha) , \\
Q_4 &= (\bar{q}^\alpha P_L b^\alpha) \otimes (\bar{q}^\beta P_R b^\beta) , \\
Q_5 &= (\bar{q}^\alpha P_L b^\beta) \otimes (\bar{q}^\beta P_R b^\alpha) , \\
Q_6 &= (\bar{q}^\alpha \gamma^\mu P_L b^\alpha) \otimes (\bar{q}^\beta \gamma_\mu P_R b^\beta) , 
\end{aligned} \tag{3.13}$$

where the superscripts  $\alpha, \beta$  denote color indices, and  $q$  stands for either  $d$  or  $s$  quark. We used the parametrization of the matrix elements of the operators in terms of the bag parameters in Vacuum Insertion Approximation

$$\langle B^0 | Q_1(\mu) | \bar{B}^0 \rangle = \frac{1}{3} M_{B_q}^2 f_{B_q}^2 B_1^q(\mu) , \tag{3.14}$$

$$\langle B^0 | Q_2(\mu) | \bar{B}^0 \rangle = -\frac{5}{24} \left( \frac{M_{B_q}}{M_b + M_q} \right)^2 M_{B_q}^2 f_{B_q}^2 B_2^q(\mu) , \tag{3.15}$$

$$\langle B^0 | Q_3(\mu) | \bar{B}^0 \rangle = \frac{1}{24} \left( \frac{M_{B_q}}{M_b + M_q} \right)^2 M_{B_q}^2 f_{B_q}^2 B_3^q(\mu) , \tag{3.16}$$

$$\langle B^0 | Q_4(\mu) | \bar{B}^0 \rangle = \frac{1}{4} \left( \frac{M_{B_q}}{M_b + M_q} \right)^2 M_{B_q}^2 f_{B_q}^2 B_4^q(\mu) , \tag{3.17}$$

$$\langle B^0 | Q_5(\mu) | \bar{B}^0 \rangle = \frac{1}{12} \left( \frac{M_{B_q}}{M_b + M_q} \right)^2 M_{B_q}^2 f_{B_q}^2 B_5^q(\mu) , \tag{3.18}$$

$$\langle B^0 | Q_6(\mu) | \bar{B}^0 \rangle = -\frac{1}{6} \left( \frac{M_{B_q}}{M_b + M_q} \right)^2 M_{B_q}^2 f_{B_q}^2 B_6^q(\mu) , \tag{3.19}$$

where  $M_{B_q}$  is the mass of the  $B_q$  meson,  $M_b$  and  $M_q$  are the masses of  $b$  quark and  $d$  or  $s$  quark respectively. And the same expressions for the operators  $Q_{1,2,3}$  (Equation (3.14), Equation (3.15) and Equation (3.16)) are valid for the operators  $\tilde{Q}_{1,2,3}$ . Performing the renormalization group (RG) evolution down to  $M_b$  scale, the associated Wilson coefficients  $C_i$ 's acquire next-to-leading (NLO) QCD correcting factors

$$C_i(M_b) = \eta_i(M_b) C_i(M_t) , \tag{3.20}$$

where  $\eta_i(M_b)$  are the QCD correction factors at NLO [69],

$$\eta_i(M_b) = \eta_i^{(0)}(M_b) + \frac{\alpha_s(M_b)}{4\pi} \eta_i^{(1)}(M_b) . \tag{3.21}$$

We took  $\alpha_s(M_b) = 0.22$  and listed the QCD correction parameters  $\eta_i(M_b)$  at NLO for all operators in Appendix C. For the meson masses and decay constants, we used the following values

$$\begin{aligned} M_{B_d} &= 5.28 \text{ GeV} & , & & M_{B_s} &= 5.37 \text{ GeV} & , \\ f_{B_d} &= 0.21 \text{ GeV} & , & & f_{B_s} &= 0.25 \text{ GeV} & , \end{aligned} \quad (3.22)$$

and the bag-parameters at the  $\mu = M_b$  scale given in Table 3.

$B_1^d(M_b)$	0.87	$B_1^s(M_b)$	0.86
$B_2^d(M_b)$	0.82	$B_2^s(M_b)$	0.83
$B_3^d(M_b)$	1.02	$B_3^s(M_b)$	1.03
$B_4^d(M_b)$	1.16	$B_4^s(M_b)$	1.17
$B_5^d(M_b)$	1.91	$B_5^s(M_b)$	1.94
$B_6^d(M_b)$	1.00	$B_6^s(M_b)$	1.00

Table 3: Bag-parameter values taken from lattice-improved calculations in the RI-MOM renormalization scheme [1], with the running quark masses  $M_b(M_b) = 4.5$  GeV and  $M_d(M_b) = 5.4$  MeV. Notice that we took  $B_6 = 1$  for both cases since the bag parameters for the relevant operator is not known yet.

In Figure 14 we show all box diagrams contributing to the  $B_{d,s}^0 - \bar{B}_{d,s}^0$  mixing, with  $q = d, s$ . All the contributions from  $W_{1,2}, G_{1,2}$  and charged Higgs bosons are encoded in the Wilson coefficients ( $C_i$  and  $\tilde{C}_i$ ) in terms of reduced Passarino-Veltman functions. We do not give explicit expressions for the different contributions, in the interest of brevity, as some have been presented before. For the analytical evaluation of the diagrams we again used the `FeynArts` to generate the amplitudes in the 't Hooft-Feynman gauge with the approximation of neglecting external momenta. However, in the limit of vanishing external momenta, all four-point functions in `LoopTools` are known to be ill-defined, so when using them in numerical calculations we introduced analytical expressions for all the relevant four-point functions and listed them in Appendix D.

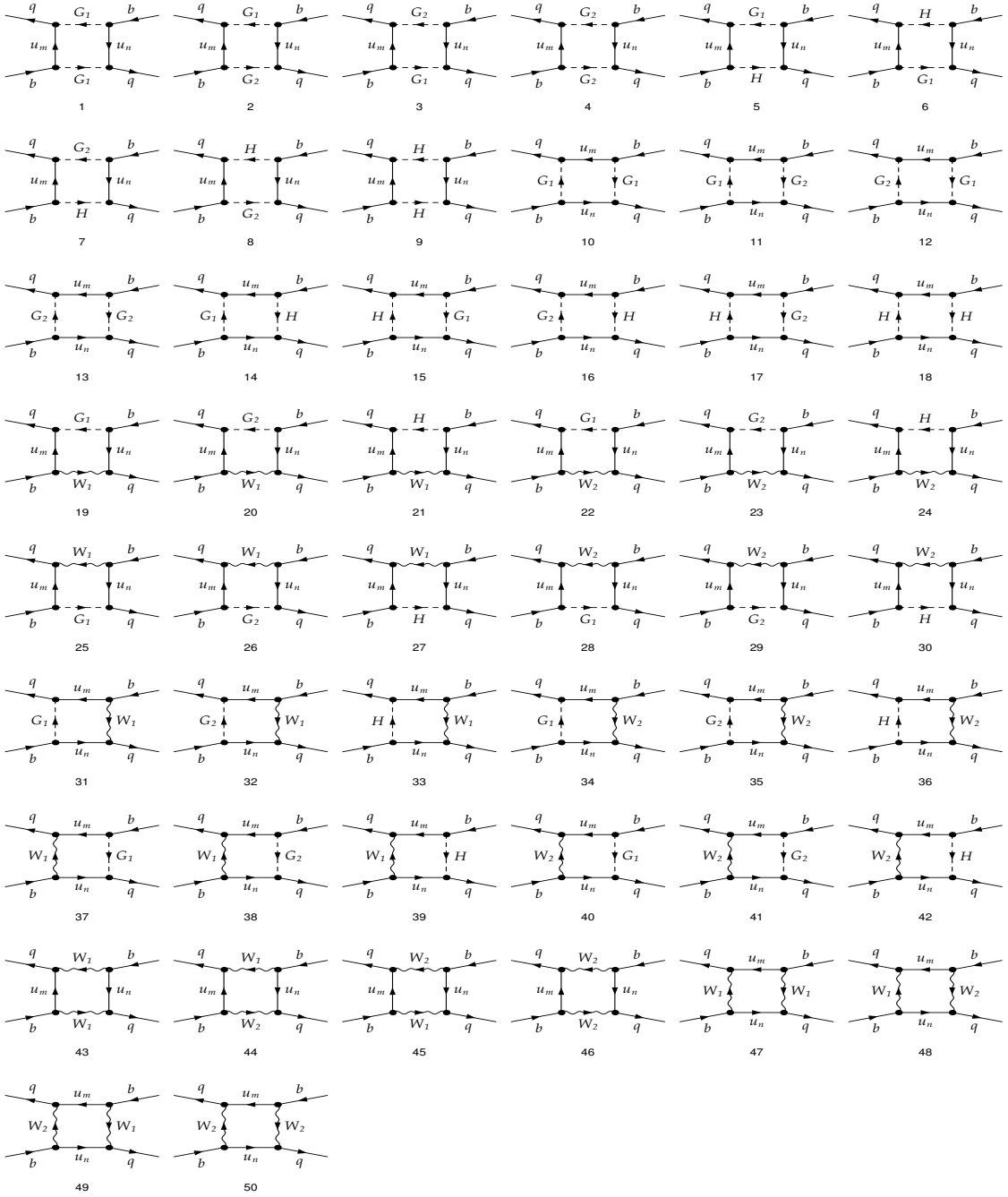


Figure 14: Box diagrams contributing to  $B^0 - \bar{B}^0$  transition. Here  $q = d$  for  $B_d^0 - \bar{B}_d^0$  and  $q = s$  for  $B_s^0 - \bar{B}_s^0$  mixing;  $u_{m,n}$  represent up-type quarks and are summed over.

Experimentally the mass differences are known with high precision [22, 70, 71]

$$\Delta M_d = (0.508 \pm 0.004) \text{ ps}^{-1} \quad , \quad \Delta M_s = (17.77 \pm 0.10 \pm 0.07) \text{ ps}^{-1} \quad . \quad (3.23)$$

However, the evaluation of the SM contributions is less precise [72]. The measured

value can be explained by the SM within 20% of theoretical uncertainty  $\Delta M_d$  is  $(0.53 \pm 0.08) \text{ ps}^{-1}$ , the error arising from uncertainties in  $\overline{MS}$  mass values, bag parameters and the decay constant [73]. This is consistent with our results. If we were to strictly impose the experimental constraints, we might incorrectly omit an important part of the parameter space. Estimating the theoretical errors conservatively at 15%<sup>2</sup>, we restrict the parameter space for  $\Delta M_d = (0.43 - 0.58) \text{ ps}^{-1}$  and  $\Delta M_s = (15 - 20) \text{ ps}^{-1}$ . We evaluate the SM contributions as  $\Delta M_d = 0.48 \text{ ps}^{-1}$  and  $\Delta M_s = 17.66 \text{ ps}^{-1}$ . As before, the parameters are  $M_{W_2}$ ,  $M_{H^\pm}$ ,  $\tan \beta$ ,  $g_{RL}$  and  $\sin \alpha$ , the measure of flavor violation in the right-handed quark sector.

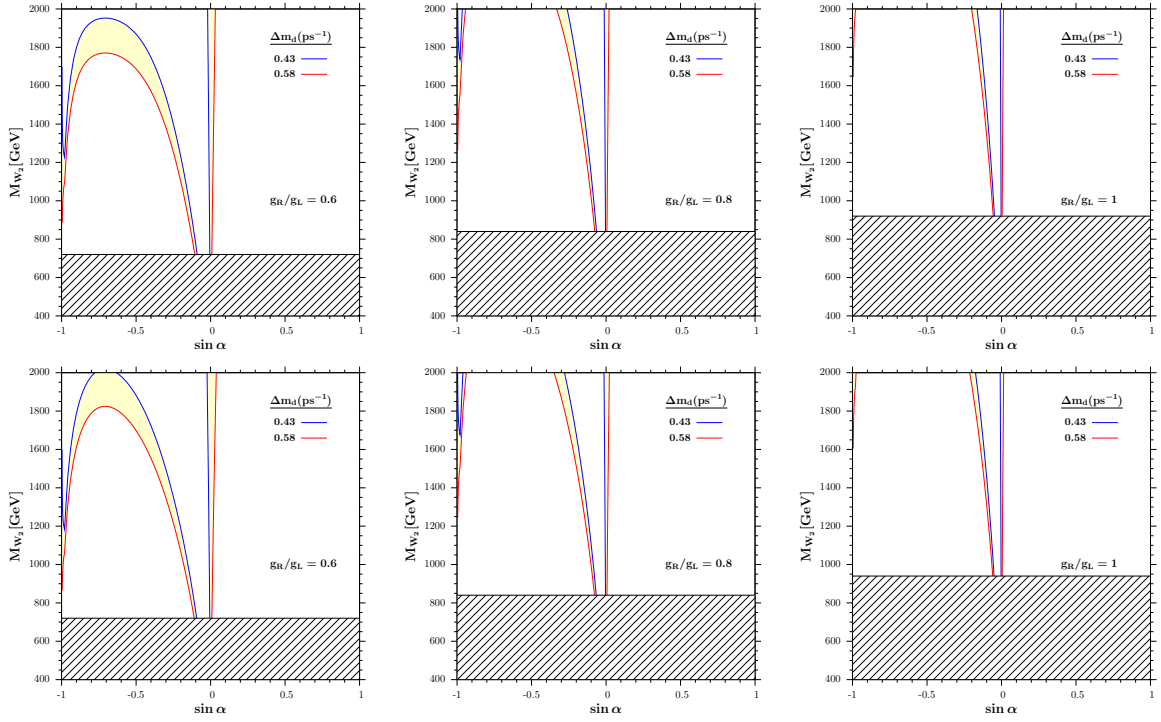


Figure 15: Contour plot of the  $M_{W_2}$  vs  $\sin \alpha$  constraint in the  $U_B$  parametrization, for the  $B_d^0 - \bar{B}_d^0$  mass difference. We fix  $\Delta M_d$  mass difference to be in the interval  $(0.43 - 0.58) \text{ ps}^{-1}$  (represented by blue and red curves, respectively) and vary  $g_{RL}$ , as indicated in the panels. We take  $M_{H^\pm} = 10 \text{ TeV}$  in upper panels and  $M_{H^\pm} = 20 \text{ TeV}$  in lower panels and  $\tan \beta = 10$ . Regions shaded are restricted by the  $W_L - W_R$  mixing angle  $\xi \leq 3 \times 10^{-3}$ . Regions highlighted in yellow represent the allowed parameter spaces.

<sup>2</sup>This is the same as assuming a Gaussian distribution and calculating the total error from the experimental and theoretical ones.

In Figure 15 we show contour plots of the  $M_{W_2}$  versus  $U_{td} = \sin \alpha$  in the  $U_B$  parametrization for the  $B_d^0 - \bar{B}_d^0$  mass difference and several values of  $g_{RL}$ . The results are very sensitive to this ratio, and we can satisfy the mass difference for any  $W_2$  mass in the 500 GeV to 2 TeV range consistently only for small  $\sin \alpha$ . Increasing  $g_{RL}$  restricts the parameter space further from  $W_L - W_R$  mixing. While the Higgs contribution compensates for some of the contributions from  $W_2$ , the  $W_2$  contribution to the mass difference appears dominant for the chosen values  $M_{H^\pm} = 10$  TeV and  $M_{H^\pm} = 20$  TeV for  $g_{RL} = 0.6, 0.8$  and 1. The interplay between the  $W_2$  and  $H^\pm$  contributions is responsible for allowed regions of parameter space away from  $\sin \alpha = 0$ , for regions around  $M_{W_2} \sim 1.8$  TeV. Note that, as the SM value is within the range considered, the region around  $\sin \alpha = 0$  is always allowed, and in fact, increasing the ratio  $g_{RL}$ , this is the parameter region that consistently survives, corresponding to a very small flavor violation in the right quark system. The sign of  $\sin \alpha$  is relevant, with more parameter regions available for  $\sin \alpha < 0$ . As before, the shaded regions are restricted by the  $W_L - W_R$  mixing angle  $\xi \leq 3 \times 10^{-3}$ .

Similarly, in Figure 16 we show the contour plot for the  $B_s^0 - \bar{B}_s^0$  mass difference, with restrictions on  $M_{W_2} - \sin \alpha$  plane in the  $U_A$  parametrization. The difference is that in this case the constraints on the parameter space are slightly less stringent and a larger region of  $(M_{W_2}, \sin \alpha)$  is allowed than in the  $\Delta M_d$  case. In the allowed range, the experimental bounds allow a significant region of the parameter space around  $\sin \alpha \in (-0.1, 0.1)$  even for  $g_{RL} = 1$ , and increasing for  $g_{RL} = 0.6$  and 0.8. The interplay between  $H^\pm$  and  $W_2$  contributions is more pronounced for  $g_{RL} = 1$ , where a region of the parameter space opens for  $M_{W_2} \sim 1.2 - 1.6$  TeV. (This region is present, to a lesser extent, for  $g_{RL} = 0.8$  in the  $M_{W_2} \sim 1 - 1.2$  TeV region.)

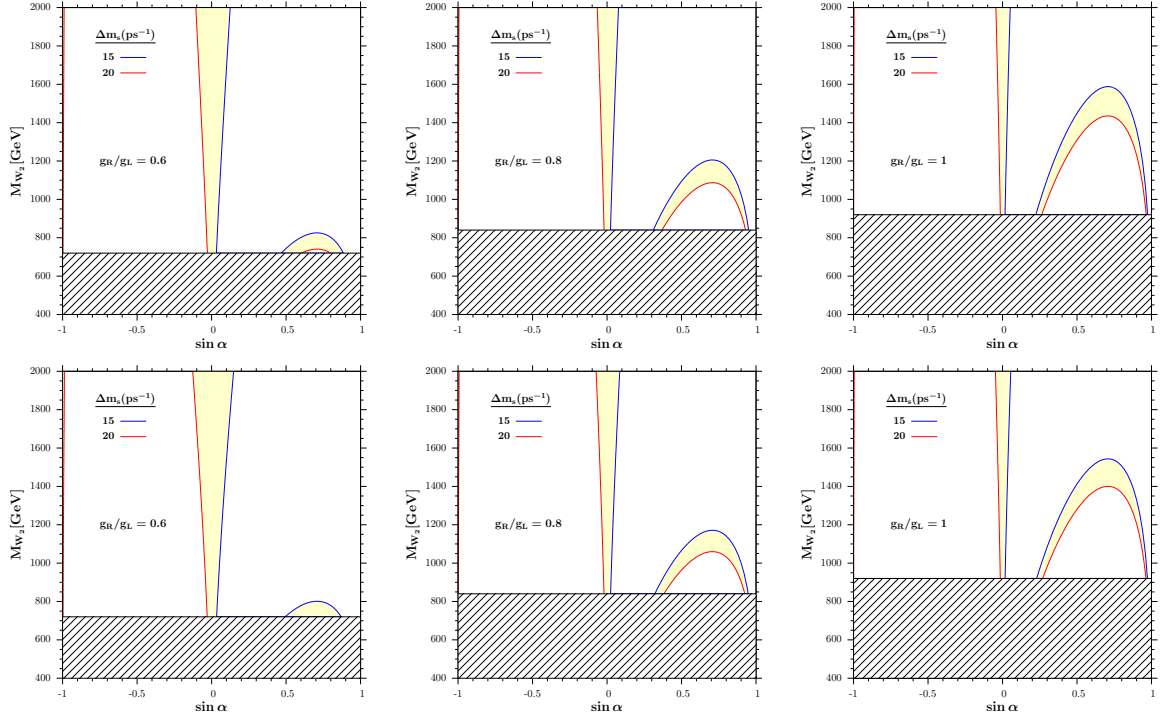


Figure 16: Contour plot of the  $M_{W_2}$  vs  $\sin \alpha$  constraint in the  $U_A$  parametrization, for the  $B_s^0 - \bar{B}_s^0$  mass difference. We fix  $\Delta m_s$  mass difference to be in the interval  $(15 - 20) \text{ ps}^{-1}$  (represented by blue and red curves, respectively) and vary  $g_{RL}$ , as indicated in the panels. We take  $M_{H^\pm} = 10 \text{ TeV}$  in upper panels and  $M_{H^\pm} = 20 \text{ TeV}$  in lower panels, and  $\tan \beta = 10$  throughout. Regions shaded are restricted by the  $W_L - W_R$  mixing angle  $\xi \leq 3 \times 10^{-3}$ . Regions highlighted in yellow represent the allowed parameter spaces.

In Figure 17, we show the dependence of  $\Delta M_d$  (upper row) and  $\Delta M_s$  (lower row) on the charged Higgs mass, for two values of  $g_{RL} : 0.6$  and  $0.8$ . We include a sample of significant plots, for two values of  $M_{W_2}$ ,  $M_{W_2} = 1$  and  $2 \text{ TeV}$ , for values of  $\sin \alpha$  chosen to fit within the allowed experimental range. One can see, comparing the top panels, that the  $B_d^0 - \bar{B}_d^0$  mass difference is sensitive to both the  $M_{W_2}$  mass and to the measure of CKM flavor violation in the right-handed quark sector,  $\sin \alpha$ . For  $g_{RL} = 0.6$  and  $M_{W_2} = 1 \text{ TeV}$ , the charged Higgs mass must be  $M_{H^\pm} \geq 10 \text{ TeV}$  for  $\sin \alpha \in (-0.17, 0.01)$  interval. This constraint is relaxed for  $g_{RL} = 0.8$  and  $M_{W_2} = 2 \text{ TeV}$ , when  $\sin \alpha \in (-0.3, 0.02)$  for  $M_{H^\pm} \geq 7 \text{ TeV}$ ; while outside this  $\sin \alpha$  interval the bounds are not satisfied for any charged Higgs masses, and one would need to increase the  $W_2$  mass to reproduce the data. In the bottom row, we perform the same analysis

for  $\Delta M_s$ . The constraints for  $M_{W_2} = 1$  TeV,  $g_{RL} = 0.6$  (left panel) are satisfied for  $M_{H^\pm} \geq 7$  TeV, but in a smaller region, for  $\sin \alpha \in (-0.04, 0.05)$ , than those for  $\Delta M_d$ . For  $M_{W_2} = 2$  TeV, to remain within the bounds for  $g_{RL} = 0.8$  (right panel) requires  $M_{H^\pm} \geq 10$  TeV for  $\sin \alpha \in (-0.07, 0.08)$ . The horizontal region highlighted in yellow corresponds to the allowed region between the bounds,  $\Delta M_d = (0.43 - 0.58)$  ps<sup>-1</sup>, and  $\Delta M_s = (15 - 20)$  ps<sup>-1</sup>. As in the  $b \rightarrow s\gamma$ , our model requires heavier Higgs bosons especially for larger flavor violation in the right-handed quark sector.

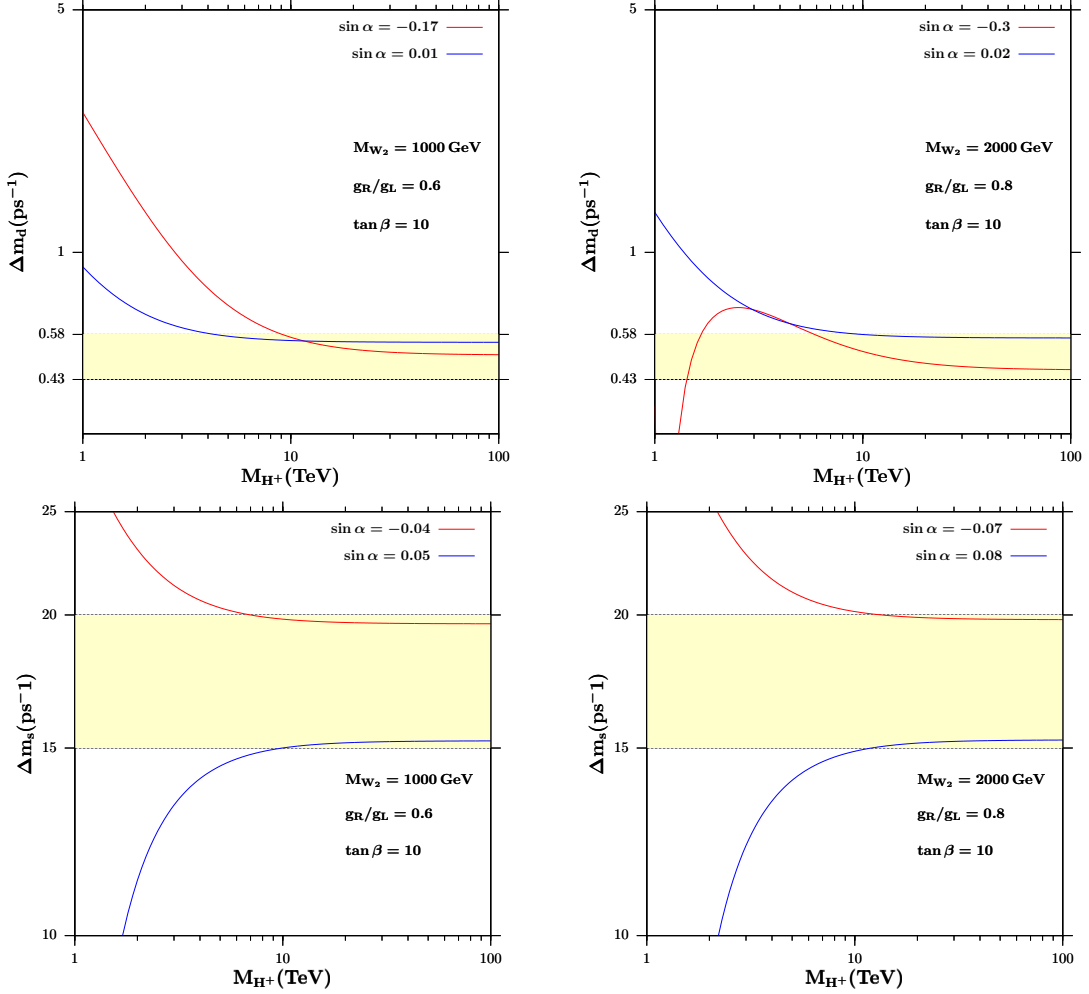


Figure 17:  $\Delta M_{d,s}$  dependence on the charged Higgs mass  $M_{H^\pm}$ . We fix  $\tan \beta = 10$  and show curves for negative and positive values of  $\sin \alpha$ , in red and blue respectively, chosen in each panel to fit within the experimental range. The yellow highlighted regions represent allowed parameter regions between  $\Delta M_d = (0.43 - 0.58)$  ps<sup>-1</sup> and  $\Delta M_s = (15 - 20)$  ps<sup>-1</sup>.



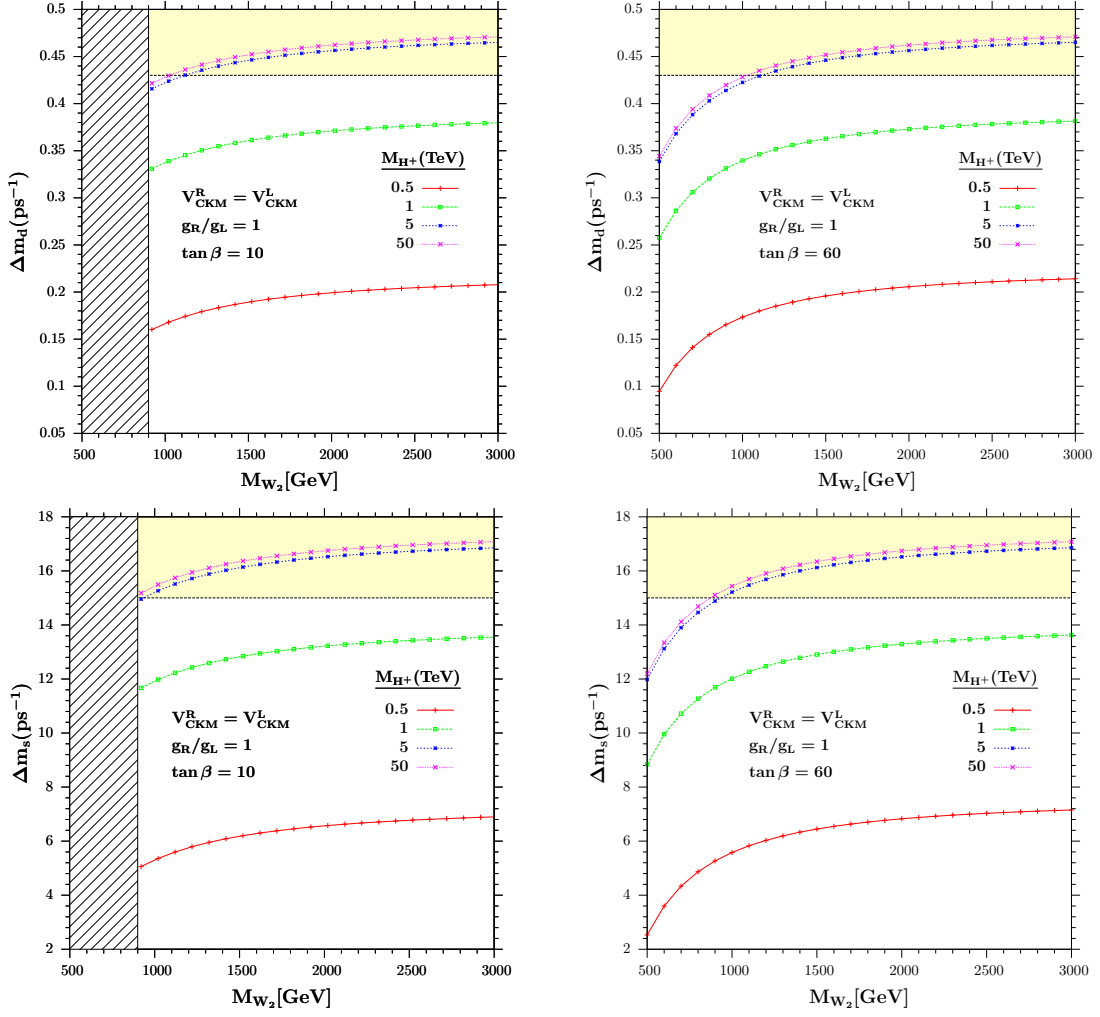


Figure 18:  $\Delta M_{d,s}$  dependence on the  $W_2$  mass in MLRSM for  $M_{H^\pm} = 0.5, 1, 5$  and  $50$  TeV. We show  $\Delta M_d$  in the upper panels, and  $\Delta M_s$  in the lower ones. The left row corresponds to  $\tan \beta = 10$ , the right one to  $\tan \beta = 60$ . Regions shaded are restricted by the  $W_L - W_R$  mixing angle  $\xi \leq 3 \times 10^{-3}$ . Regions highlighted in yellow represent the allowed parameter spaces.

In the MLRSM case, with  $V_{CKM}^R$  and  $g_R = g_L$  fixed, Higgs masses are required to be 5 TeV or larger for both  $\tan \beta = 10$  and  $60$ , while  $M_{W_2} > 1$  TeV, as shown in Figure 18, where we study the dependence of  $\Delta M_{d,s}$  on  $W_2$  mass for four values of the charged Higgs mass, 0.5, 1, 5 and 50 TeV. Note that there is no new information provided by  $\Delta M_s$  data and that the manifest LR contribution is also largely insensitive to  $\tan \beta$ .

### 3.3 Summary

With the advent of the data from LHC, we expect to observe physics beyond the SM. The LRSM is perhaps the simplest such scenario, with the right-handed quarks belonging to doublets and participating in charged flavor violating interactions. Models in which the right-handed sector mimics exactly the left-handed one, such as the manifest or the pseudo-manifest LR model, have been explored thoroughly and are very restrictive. Motivated by the possibility of additional gauge bosons that may be observed at the LHC, as well as some shortcomings of a LR symmetric quark flavor sector, we investigated here an asymmetric LR parametrization for the quark mixing matrix (Langacker and Sankar) in the context of B physics [8]. This parametrization has several attractive features: while respecting family unitarity, it is general. It allows for variations in the right-handed coupling constant and it is simple, thus predictive (the right handed quark mixing matrix depends on one additional parameter only).

Note that our results are quite general, if we restrict ourselves to parametrizing two family mixings only, in the CP conserving case, since setting  $U_{ts} = \sin \alpha$  in the  $U_A$  parametrization, and  $U_{td} = \sin \alpha$  in the  $U_B$  parametrization, satisfies general unitarity constraints.

We include existing restrictions on the  $W_L - W_R$  mixing angle  $\xi$  coming from  $K^0 - \bar{K}^0$  mixing, while not restricting ourselves to any particular scenario for the nature or masses of the neutrinos. We provide additional constraints from  $\text{BR}(b \rightarrow s\gamma)$  and  $B_{d,s}^0 - \bar{B}_{d,s}^0$  mixing. Defining the parametrizations as  $U_A$  ( $U_{ts} \neq 0, U_{td} = 0$ ) and  $U_B$  ( $U_{td} \neq 0, U_{ts} = 0$ ), we set constraints on  $\sin \alpha, M_{W_2}, g_{RL}, \tan \beta$ , and  $M_{H^\pm}$ . We have used exact numerical evaluations and the existing packages `FeynArts` for generating the amplitudes, then `FormCalc` and `LoopTools` packages to evaluate the loop contributions, and added modifications as needed.

For the branching ratio  $b \rightarrow s\gamma$ , all parameters play an important role. Smaller values for the ratio  $g_{RL}$  allow for more flavor violation in the right quark sector (larger  $\sin \alpha$ , smaller  $W_2$  masses, wider range for  $M_{H^\pm}$ ).  $\text{BR}(b \rightarrow s\gamma)$  also depends on  $\tan \beta$ . Increasing  $\tan \beta$  opens larger parameter spaces for both  $M_{H^\pm}$  and  $M_{W_2}$ . In  $\Delta M_{d,s}$  splitting, we find the results to be sensitive to the  $W_2$  mass,  $\sin \alpha$  and the ratio  $g_{RL}$ . In the regions allowed by the experimental constraints, the results are practically independent of  $\tan \beta$ .

While a lot of restrictions are interconnected, they share a few general characteristics. First, the restrictions on  $U_B$ , coming from  $B_d^0 - \bar{B}_d^0$  are more stringent than the combined bounds on  $U_A$  coming from  $b \rightarrow s\gamma$  and  $B_s^0 - \bar{B}_s^0$ . As these two parametrizations are independent, the larger parameter space available for  $U_A$  indicates that in that scenario, lighter gauge bosons are more likely to be produced. Second, for any significant regions of parameter space we have  $g_{RL} < 1$ . While decreasing  $g_R$  decreases the strength and cross section for right-handed particles, it allows for larger flavor violation in the right-handed sector. It is a delicate balance, as decreasing the amount of right-handed flavor violation makes the model more like the MLRSM, and decreasing it even further takes the model to the SM. We restrict  $g_{RL} > \tan\theta_W$  to reproduce correctly the  $U(1)_Y$  coupling constant. On the other hand,  $g_{RL} < 1$  allows for more flavor violation and smaller  $W_2$  masses, while requiring heavy charged Higgs boson masses,  $M_{H^\pm} \geq 10$  TeV. The results obtained are consistent with manifest or pseudo-manifest left-right symmetric models, while allowing more flexibility in the parameter space and opening the possibility of observing light gauge bosons at the LHC. However, even allowing for more variations of model parameters, the allowed parameter space in  $M_{W_2}, \sin\alpha, M_{H^\pm}$  is quite constrained, making the ALRM very predictive.

After scanning the parameter space of ALRM and constraining the model parameters, at the next chapter we investigate the production and decay of  $W_R$  gauge boson and its signatures in hadron colliders including the restriction on model parameters.

# Chapter 4

## PRODUCTION AND DECAY OF $W_R$ BOSON AT THE LHC

While the SM has provided a compelling picture of low-energy interactions, it has been plagued by theoretical inconsistencies. More recently, experimental deviations from the predictions of the model such as signals of neutrino masses and mixing [74] have given further justification to building of BSM physics. Additionally, the experimental outlook on testing these scenarios looks very promising. LHC data is expected to provide ample material for analysis. When the data become available, it would be probably difficult to disentangle expectations for different models. The task of theorists is to provide viable scenarios for BSM physics and to predict the signals which distinguish them from the SM and from each other.

A large variety of models is available, all of which attempt to resolve some theoretical inconsistency of the SM. Of these, a particularly simple model is the LRSM [2, 3, 6, 23–25]. Originally introduced to resolve the parity and neutrino mass problems, it remains one of the simplest extensions of the SM, and it is a natural scenario for the see-saw mechanism [27]. The Higgs sector of the LRSM and its signals at accelerators have been thoroughly analyzed by theorists [28–38], and experimentalists have been particularly keen to search for doubly charged Higgs bosons, predicted in most versions of the model [75–77]. Less attention has been paid to the vector boson sector. The LRSM extends the gauge group of the SM to  $SU(2)_L \times SU(2)_R \times U(1)_{B-L}$ , and thus predicts the existence of two extra gauge bosons: a neutral  $Z_R$  and a charged  $W_R$ . While an extra neutral gauge boson  $Z'$  is predicted by several extensions of the

SM, all containing an extra gauged  $U(1)$  symmetry group, a charged gauge boson would be a more likely indication of LR symmetry<sup>1</sup>.

Several other models predict the existence of extra  $W'$  bosons, such as extra dimensional models (both Randall-Sundrum (RS) [78–80] and Universal Extra Dimensions (UED) model [81, 82]), Little Higgs models [83–85] and Composite Higgs models [86–88]. The  $W'$  predicted in these models have features which distinguish them from those of the LRSM, which we will discuss after our analysis.

Production of extra charged vector bosons at colliders has received less interest than that of  $Z'$ , although one study exists for the Tevatron [89]. However, recent papers analyzing chiral couplings of a  $W'$  at the LHC indicate how to disentangle left or right handed bosons [90, 91]. In this thesis, we follow a different procedure. Assuming the extra charged vector boson to come from a version of the LRSM and thus be right-handed, we analyze the production mechanism, decay rates, and possible signals at the LHC.

$W_R$  bosons are predicted to be heavy, of the order of  $\mathcal{O}(\text{TeV})$  and thus the signal is expected to be much below the  $W_L$  production signal. But this is only the case if the quark mixing matrix in the right-handed sector ( $V_{CKM}^R$ ) is either identical, or equal up to a diagonal matrix, to the one in the left-handed sector the usual  $V_{CKM}^L$  –the so-called *manifest* and *pseudo-manifest* LRSM, respectively. This does not have to be the case, as was discussed at length by Langacker and Sankar [5], who allow right-handed mixing matrices  $V_{CKM}^R$  with large off-diagonal elements. They perform a thorough investigation of the constraints on the mass of  $W_R$  and its mixing with  $W_L$  under these circumstances and find out that the  $W_R$  mass can be a lot lighter,  $M_{W_R} \gtrsim 300 \text{ GeV}$  [17].

In the age of the LHC there is another immediate advantage of the ALRM: such a  $W_R$  boson can be produced at rates larger, by orders of magnitude, than for models in which  $V_{CKM}^R = V_{CKM}^{L*} K$ , where  $K$  is a diagonal phase matrix. One could see this by looking at the signal  $pp \rightarrow W_{L,R} t$ . This single-top production cross section is known to be important in identifying and distinguishing between different new physics models, as these can have different effects ( $s$ -channel or  $t$ -channel) on the production process [92, 93]. The partonic cross section at the LHC is dominated by  $qg$ , with  $q = d, s$ . However, for  $W_L$  production one must rely on the process  $gb \rightarrow b \rightarrow tW$ ,

---

<sup>1</sup>While  $W_R$  is present in several gauge unification scenarios, models with extra  $W_L$  bosons also exist.

and thus be disadvantaged by the small amount of  $b$  quarks in the proton; or rely on  $gd(s) \rightarrow d(s) \rightarrow tW$ , which is suppressed by the  $V_{ts}^L$  or  $V_{td}^L$  element of the  $V_{CKM}^L$ . However, if the off-diagonal  $V_{ts}^R$  or  $V_{td}^R$  elements of the  $V_{CKM}^R$  are large, one could produce  $W_R$  copiously. Additionally, if there are less stringent restrictions on the  $W_R$  mass, one can envisage that  $W_R$  production could be observable and, if so, a clear distinguishing signal for LRSM. At the Tevatron, the production cross section is dominated at the partonic level by  $q\bar{q}$ , with  $q = u, d, s, c$ . Even for a light  $W_R$  boson, we would not expect any enhancements due to the non-diagonal entries in the  $V_{CKM}^R$ ; the same is true for linear colliders.

The sensitivity of the Tevatron to  $W_R$  searches has been thoroughly discussed in Reference [89]. Mass limits from the existing data depend on the ratio of the coupling constants for  $SU(2)_R$  and  $SU(2)_L$ ,  $g_{RL}$ , on the nature and mass of the right-handed neutrinos  $\nu_R$ , on the leptonic branching ratio for  $W_R$ , and on the form of the right-handed CKM matrix  $V_{CKM}^R$ . The most stringent experimental bounds from Tevatron searches are  $M_{W_R} \geq 1$  TeV, under very specific assumptions (looking for  $W_R$  decays into an electron and a neutrino, for SM-like couplings to fermions) [94, 95]. As their assumptions would not apply to our model, we investigate the possible signals and mass bounds at the Tevatron in *dijet* production before proceeding with the LHC signal analysis.

The LHC thus presents a unique opportunity to observe such a  $W_R$  boson. We propose to investigate this possibility in this thesis. In Chapter 3 we have laid the foundation of flavor-changing studies in LR models by analyzing the most general restrictions on the parameter space of the model ( $M_{W_R}$ ,  $M_{H^\pm}$ ,  $V_{CKM}^R$ , and  $g_{RL}$ ) coming from  $b \rightarrow s\gamma$ ,  $B_d^0 - \bar{B}_d^0$  and  $B_s^0 - \bar{B}_s^0$  mixings [8]. For consistency, we include here these parameter space restrictions as well as those coming from the Kaon physics.

## 4.1 Production and Decays

In this section we investigate the single production cross section at the LHC of a  $W_R^\pm$  boson,  $pp \rightarrow tW_R$ , and decay branching ratios of the right-handed  $W$  boson in the scenarios in which the RCKM matrix is  $U_A$  or  $U_B$  as, in Equation (2.51), and compare the results to those obtained in the MLRSM. In the MLRSM the CKM matrices in the left- and right-handed quark sectors are the same and so are the coupling constants for

$SU(2)_L$  and  $SU(2)_R$ . The only unknown parameter is the  $W_R$  mass; while in  $U_A$  and  $U_B$  the production and decay rates are also functions of  $\sin \alpha$ , the RCKM parameter, as well as the ratio  $g_{RL}$  of  $SU(2)_L$  and  $SU(2)_R$  coupling constants. The dominant partonic level Feynman diagrams are shown in Figure 19. The index  $i$  indicates that we sum over the three generations.

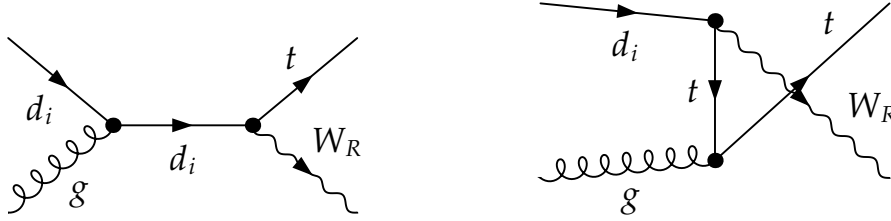


Figure 19: Feynman diagrams of the  $W_R$ -top associated production at the LHC.

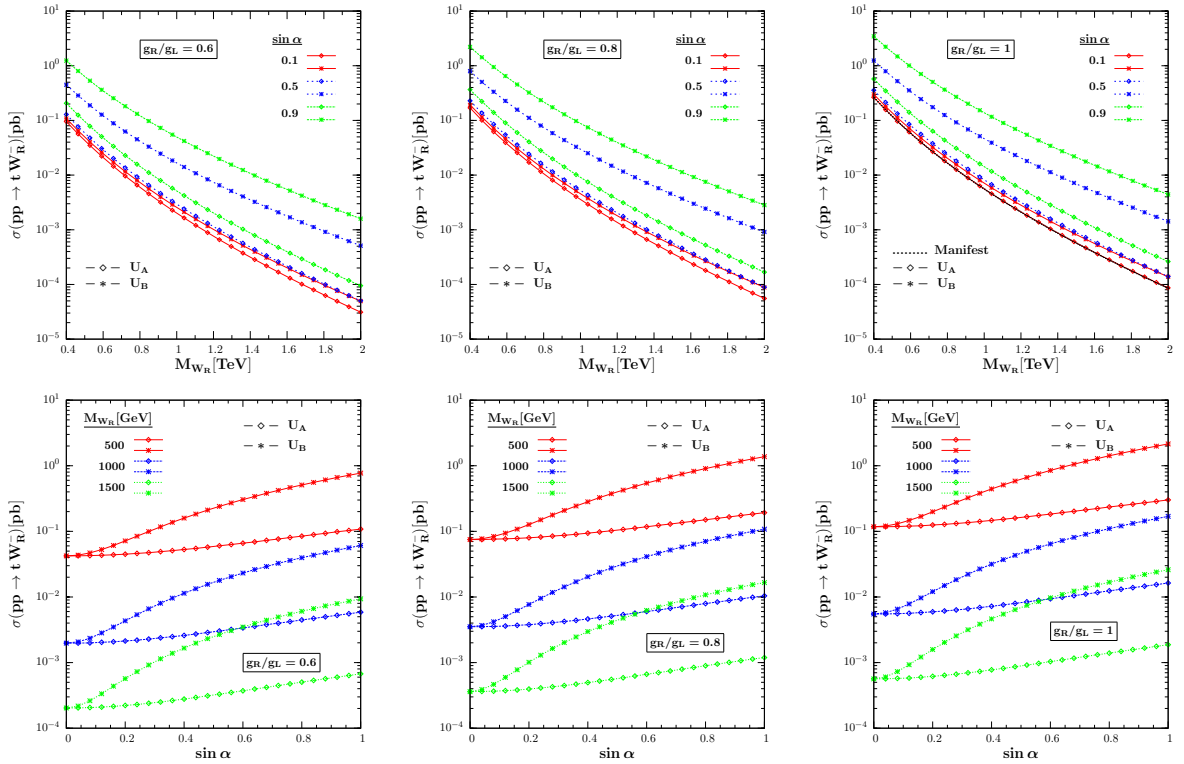


Figure 20:  $W_R$  production cross-section as a function of the  $W_R$  mass (upper panels) and RCKM matrix parameter  $\sin \alpha$  (lower panels), for the three models described in the text ( $U_A$ ,  $U_B$  and MLRSM).

In Figure 20, top row, we present the single  $W_R$  production cross section as a function of the  $W_R$  mass (in the 400-2000 GeV range) for three values of  $\sin \alpha$ . The

three panels correspond to three values allowed for  $g_{RL}$  : 0.6, 0.8 and 1. When  $\sin \alpha$  is large, the off diagonal RCKM mixing element  $U_{td}$  or  $U_{ts}$  becomes large. As there are more  $d$  and  $s$  quarks than  $b$  in the proton, this enhances the hadronic contribution to the cross section for  $U_A$  and  $U_B$  cases. The production cross section decreases when  $W_R$  mass increases, or  $\sin \alpha$  decreases. Similarly, the production cross section is enhanced by larger  $g_{RL}$ . The MLRSM cross section overlaps with that of model  $U_A$  in the case of  $\sin \alpha = 0.1$  (the right panel in the top row).

In the bottom row of Figure 20 we explore the dependence of the cross section in  $U_A$  and  $U_B$  on  $\sin \alpha$  for three values of  $M_{W_R}$ . The three panels again represent cross sections for  $g_{RL} = 0.6, 0.8$  and 1. Figure 20 shows that in the region of large  $\sin \alpha$  and low  $M_{W_R}$  we can expect large enhancements in the production cross section. For suitable choices of  $\sin \alpha$  and  $M_{W_R}$  (light  $W_R$  mass and large  $\sin \alpha$  region), the cross section can reach 1 pb or more. The slight difference between  $U_A$  and  $U_B$  cross sections is attributed to the relative abundance of  $d$  over  $s$  quarks in the proton.

In Figure 21 we give a contour plot in the  $M_{W_R} - \sin \alpha$  parameter space, including constraints from  $b \rightarrow s\gamma$ ,  $B_d^0 - \bar{B}_d^0$ , and  $B_s^0 - \bar{B}_s^0$  processes. This plot correlates restrictions on  $\sin \alpha$ ,  $M_{W_R}$ ,  $g_{RL}$  and production cross sections. In the top row, we show the plot for the  $U_A$  parametrization. This parametrization is constrained by  $b \rightarrow s\gamma$  branching ratio (in yellow) and  $B_s^0 - \bar{B}_s^0$  mixing (dashed). The three panels represent increasing values of coupling constants ratio  $g_{RL} = 0.6, 0.8$  and 1. The dark shaded parameter region at the bottom (increasing with larger  $g_{RL}$ ) represents restrictions due to the  $W_L - W_R$  mixing angle  $\xi < 3 \times 10^{-3}$ . The most stringent phenomenological inputs which restrict the  $W_L - W_R$  mixing angle  $\xi$  are: weak universality for light neutrinos, partial conservation of axial-vector-current in  $K \rightarrow 2\pi$  and  $K \rightarrow 3\pi$  and constraints on  $W_L$  mass, which is reduced by increasing  $\xi$  [5]. The parameter space is overall very restricted. For smaller  $g_{RL}$  there is a stable allowed region around  $\sin \alpha = 0$ , which is decreasing with increasing  $g_{RL}$ . However, for all coupling ratios, there is a parameter space allowed, where  $\sin \alpha$  is large and positive, and the  $W_R$  mass can be relatively light ( $M_{W_R} = 600 - 700$  GeV for  $g_{RL} = 0.6$ ) or intermediate ( $M_{W_R} = 1400 - 1500$  GeV for  $g_{RL} = 1$ ). For these cases the cross section can be of order  $10^{-2}$  pb.



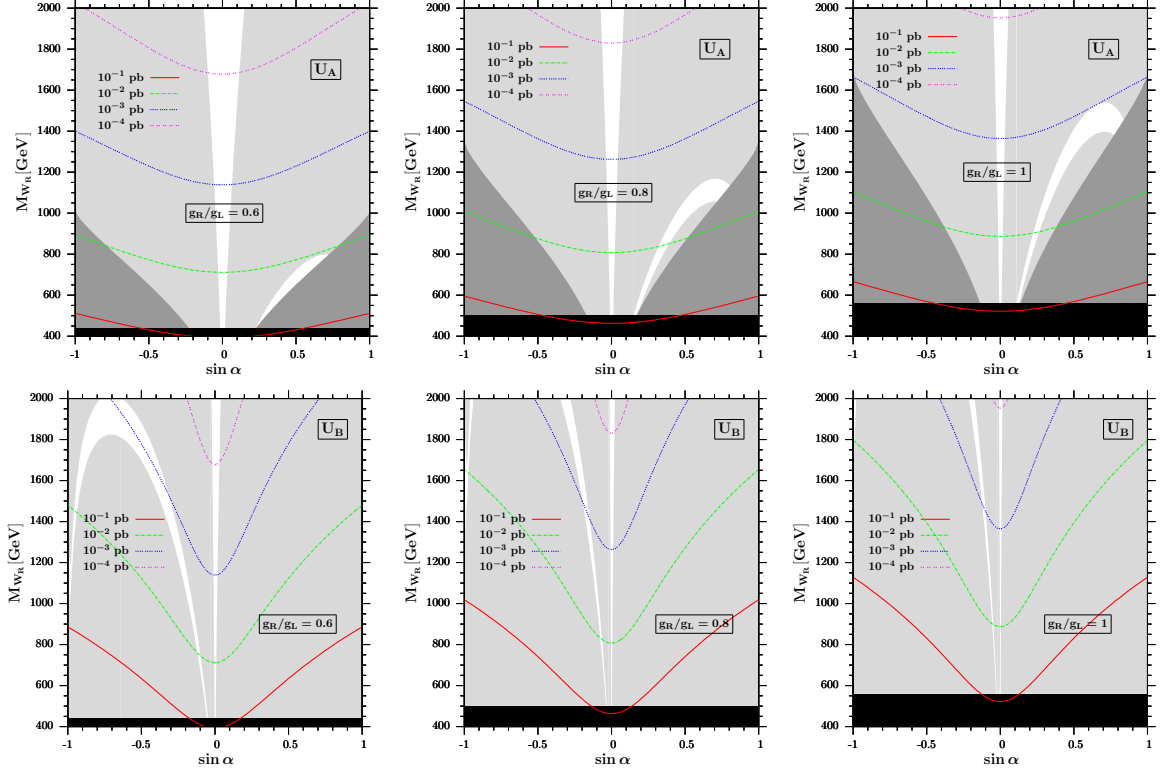


Figure 21: Contour plot of  $M_{W_R}$  vs  $\sin \alpha$ . The upper row is for the  $U_A$  parametrization in which the  $W_R$  production cross-sections are constrained by both  $b \rightarrow s\gamma$  and  $B_s^0 - \bar{B}_s^0$  processes. Dark-gray shaded regions are excluded from  $b \rightarrow s\gamma$  and light-gray shaded regions from  $B_s^0 - \bar{B}_s^0$ . Black shaded region indicates the exclusion by L-R mixing angle violation ( $\xi < 3 \times 10^{-3}$ ). The lower row is for the  $U_B$  parametrization where only  $B_d^0 - \bar{B}_d^0$  mixing constrains the production cross-section. In both parametrizations we take  $M_{H^\pm} = 20$  TeV and  $\tan \beta = 30$ .

The bottom row of Figure 21 presents the same restrictions on the  $M_{W_R} - \sin \alpha$  parameter space in the  $U_B$  parametrization. The three panels again represent restrictions for  $g_{RL} = 0.6, 0.8$  and  $1$ . The restrictions come from  $B_d^0 - \bar{B}_d^0$  (light-gray shaded) and the  $W_L - W_R$  mixing angle  $\xi < 3 \times 10^{-3}$  (black shaded—this constraint is the same as in the upper row). The  $U_B$  parametrization is much more restricted, reflecting the stringent restrictions from  $B_d^0 - \bar{B}_d^0$  mixing. While the same region around  $\sin \alpha = 0$  exists in all graphs, it is shrunk very close to zero, especially for  $g_{RL} = 1$ . The region for  $\sin \alpha$  away from zero (in this case negative) is significant only for  $g_{RL} = 0.6$  and larger values of the  $W_R$  mass. Still, there is a small parameter space available for  $M_{W_R} = 1.8 - 2$  TeV. But the cross section expected in this region is of order of  $10^{-3}$

pb, smaller by a factor of 10 than that for the  $U_A$  parametrization.

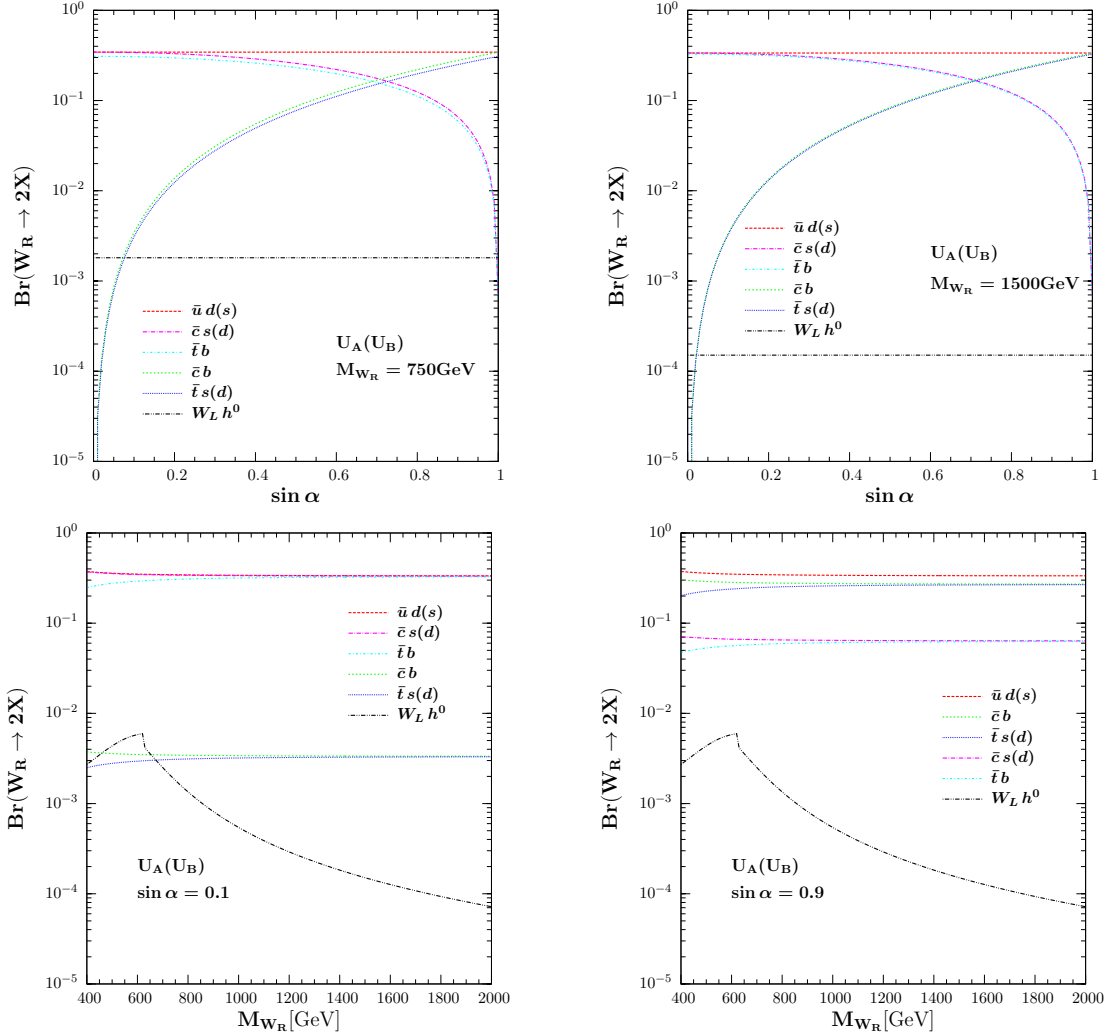


Figure 22: Branching ratios of  $W_R$  decays as functions of  $\sin \alpha$  (upper panels) and  $W_R$  mass (lower panels). The  $W_R$  mass is fixed at 750 GeV in the top left and 1500 GeV in the top right panel, while  $\sin \alpha$  is fixed to 0.1 in the bottom left panel and 0.9 in right one.

In Figure 22 we present the branching ratios of  $W_R$  decays into quarks, and a representative one into  $W_L h^0$ , assuming this decay has the phase space required to proceed in the ALRM. In the top panels, we analyze the decay width into quarks, as a function of  $\sin \alpha$ , for both  $U_A$  and  $U_B$  scenarios. The left panel corresponds to  $M_{W_R} = 750$  GeV, the right one to  $M_{W_R} = 1.5$  TeV. It is possible to include both parametrizations in one plot because, between these two scenarios, the CKM matrix

elements involving  $s$  and  $d$  quark mixing with  $t$  quarks are switched, and although the masses of these quarks are not identical, it does not significantly impact the branching ratios. While  $W_R^- \rightarrow d(s)\bar{u}$  is the dominant decay for both cases, for large  $\sin\alpha$  the branching ratios to  $b\bar{c}$  and  $d(s)\bar{t}$  become comparable; while for low  $\sin\alpha$  the branching ratios to the same-generation pairs,  $b\bar{t}$  and  $s\bar{c}$ , are large. The leptonic decays  $W_R^- \rightarrow l^-\bar{\nu}_R$ , ( $l = e, \mu$ ) are not presented here, as we wanted to avoid extra assumptions on the nature of the neutrinos and their masses. Many other decay channels are possible, but we have chosen to only illustrate  $W_L h^0$ . It is possible that, for a range of the parameters, there is sufficient phase space for other decays (to leptons,  $h^0 H^\pm$ ,  $Z_L H^\pm, \dots$ ) to proceed, but all require further assumptions. In our analysis, charged Higgs and all other neutral Higgs bosons except for  $h^0$  are heavy, so these channels are not open. The branching ratio to  $W_L h^0$  is independent of  $\sin\alpha$  and always dominated by branching ratios to quarks.

The panels in the bottom row show the dependence on the same branching ratios as a function of  $M_{W_R}$ , for  $\sin\alpha = 0.1$  (left panel) and  $\sin\alpha = 0.9$  (right panel). The dominance of the  $d(s)\bar{u}$  decay mode persists, and is independent of  $\sin\alpha$ , a consequence of the form chosen for  $V_{CKM}^R$  to agree with Kaon phenomenology. The branching ratios are independent of the mass of the  $W_R$ , with the exception of  $W_L h^0$ . Note that the branching ratios also do not depend on the coupling constant for  $SU(2)_R$  (or  $g_{RL}$ ), as it appears as an overall factor in both the partial decay width and total width formula.

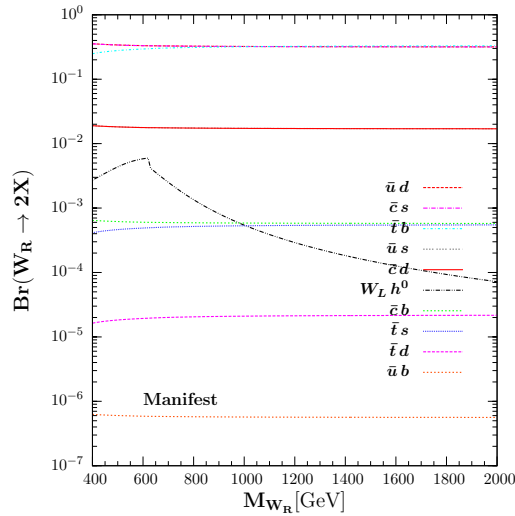


Figure 23: Branching ratios of  $W_R$  decays as functions of the  $W_R$  mass in the MLRSM.

Figure 23 illustrates the branching ratios of all decay modes of the  $W_R$  boson in the MLRSM. The main difference from the point of view of observability is that in the  $U_A, U_B$  scenarios there are 5  $q\bar{q}'$  decay modes with branching ratios in the range  $5 \times 10^{-2} - 2 \times 10^{-1}$ , while in MLRSM there are only 3 (for  $M_{W_R} > 500$  GeV). In both cases, all other branching ratios are much smaller and very similar in all three scenarios. For the purpose of explicit branching ratio calculations, we considered the case in which the bi-doublet Higgs boson is supplemented by triplet Higgs bosons. Under this assumption we diagonalized the Higgs mass matrix and calculated the Feynman rules. We expect the case with doublet Higgs bosons to yield very similar results when we impose experimental constraints.

## 4.2 Signal and Background for $W_R$ Production at the LHC

Before proceeding with the analysis of the  $W_R$  production signal at the LHC, we consider the signal at the Tevatron, from  $p\bar{p} \rightarrow W_R \rightarrow dijet$ . The *dijet* data is already available from CDF Run II [96] and the analysis shows no significant evidence for a narrow resonance. This is used to put mass constraints on several beyond the SM particles, including the  $W'$ . To compare the data with our model, we used the `CalcHEP 3.1` software [97] and implemented the model into it. To obtain the *dijet* spectrum we used the following detector cuts at  $\sqrt{s} = 1.96$  TeV:  $p_T > 40$  GeV,  $|y| < 1$ ,  $|\eta| < 3.6$  and  $R_{\text{cone}} = 0.7$  (jet cone angle). The parameters used to generate Figure 24 are  $M_{W_R} = 750$  GeV,  $g_{RL} = 1$ ,  $\sin \alpha = 0.2(-0.05)$  for  $U_A(U_B)$ . The *dijet* process is dominated by  $s$ -channel contributions. From the figure we see that under these conditions, the  $W_R$  signal falls below the CDF data and would not be observable at the Tevatron. Thus we cannot expect to extract meaningful mass bounds for  $W_R$  even for a relatively light gauge boson.

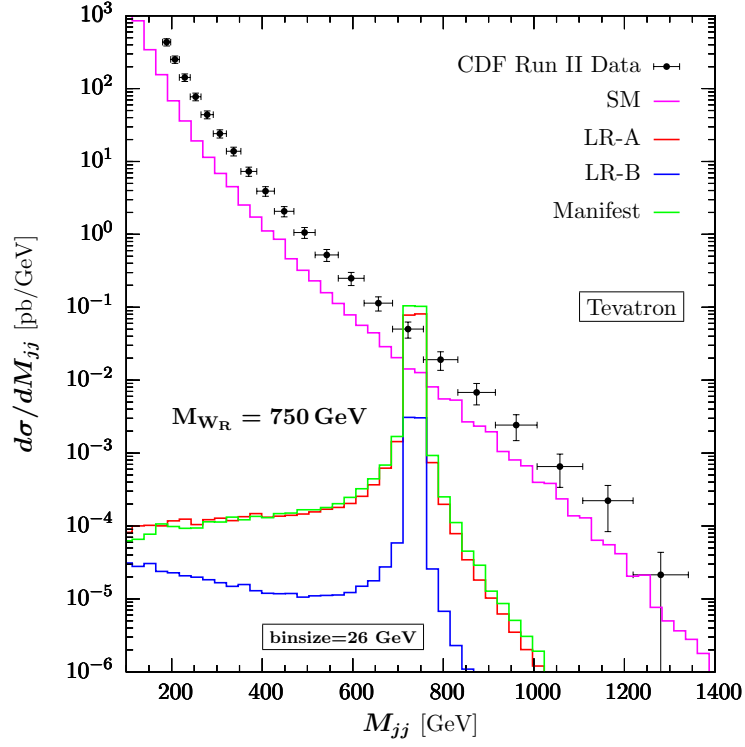


Figure 24: Differential cross section for the *dijet* mass spectrum for  $W_R$  decays in the  $U_A$ ,  $U_B$  parametrizations and in the MLRSM, compared to the SM background and the CDF data. It is possible to show that the SM curve agrees very well with the CDF Run II data after including NLO perturbative QCD corrections. Our SM curve should be taken as a rough estimation.

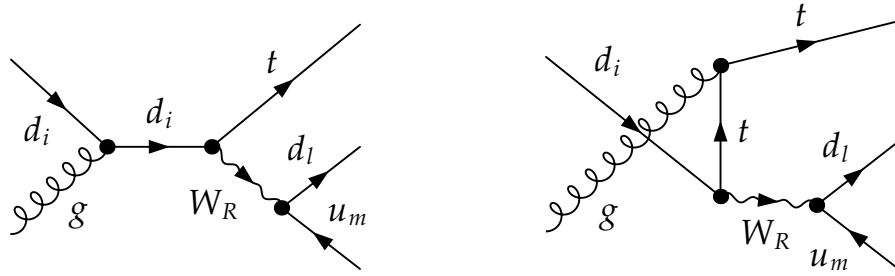


Figure 25: The signal  $pp \rightarrow t W_R \rightarrow t(\text{jet jet})$

We now proceed with the investigation of the  $W_R$  production signal at the LHC. We simply considered a single *top* production associated with a *dijet* through a  $W_R$  exchange in both *s*- and *t*-channel processes as in Figure 25. Assuming *b*-jets are tagged and further *top* decays are reconstructed, we selected only light quarks ( $u, c, d$

and  $s$ ) in jets. In order to compare our signal with the background we accounted all the possible  $top + dijet$  processes in the SM final state. For the signal analysis we used again the implementation of our model into the CALCHEP software [97]. We also introduced some basic detector cuts on the pseudo-rapidity ( $|\eta| < 2$ ) and on the transverse energy ( $p_T > 30\text{GeV}$ ). We assume that in both our model and in the SM, the top quark will decay as predicted, and it can be reconstituted. We have chosen  $W_R$  decays to quarks, rather than leptons, because we wanted to avoid assumptions on the nature and masses of neutrinos. Also, jets can be easily identified and this decay mode does not involve any missing energy, making it easier to detect a  $W_R$  resonance. We also restricted the decay products to jets (light quarks only) to avoid  $t\bar{t}$  production. In the case of considering  $W_R \rightarrow \bar{t}d_i$ , the SM background would be  $t\bar{t}j$  and could be significant.

In Figures 26 and 27 we present  $W_R$  production signal at 14 TeV with different CKM parametrizations and compare it with the SM background. We choose the bin-size to be 20 GeV, and plot the differential cross section with respect to the invariant  $dijet$  mass  $M_{jj}$ . It is clear that for all the parametrizations, the  $W_R$  signal can be observed as a resonance in the  $dijet$  invariant mass distribution at the LHC and is quite distinguishable from the SM background. The diagrams for the SM background are very similar to the ones in Figure 25,  $W_R$  replaced with  $W_L$  as well as some other exchange diagrams. Signatures in  $U_A$  and  $U_B$  parametrizations are in the left and right columns of Figure 26. In first two rows we kept  $W_R$  mass at an intermediate value ( $M_{W_R} = 1.5$  TeV) and changed the ratio of gauge coupling constants ( $g_{RL}$ ) as well as the RCKM matrix element ( $\sin \alpha$ ) between the panels. The numerical values of these parameters are chosen according to the constraints from low energy phenomenology in Figure 21. In the last row we showed the signal of a lighter  $W_R$  ( $M_{W_R} = 750$  GeV) with bin-size= 10 GeV and equal gauge coupling constants ( $g_R = g_L$ ) in the region allowed by the constraints. By comparison, in Figure 27 we show signatures for the  $W_R$  production and decay to  $dijets$  in the MLRSM model for the intermediate (left panel) and the light (right panel)  $W_R$  (the last for comparison only, as light  $W_R$  masses are largely excluded by Kaon phenomenology in the absence of extreme fine tuning). It is inferred from these figures that a new right handed charged gauge boson signal of LR symmetry is very clear, distinct and accessible within the LHC's discovery limits. For a luminosity of  $100 \text{ fb}^{-1}$  at 14 TeV and a light  $W_R$  boson (both

very optimistic assumptions), the signal can reach 100 events per year.

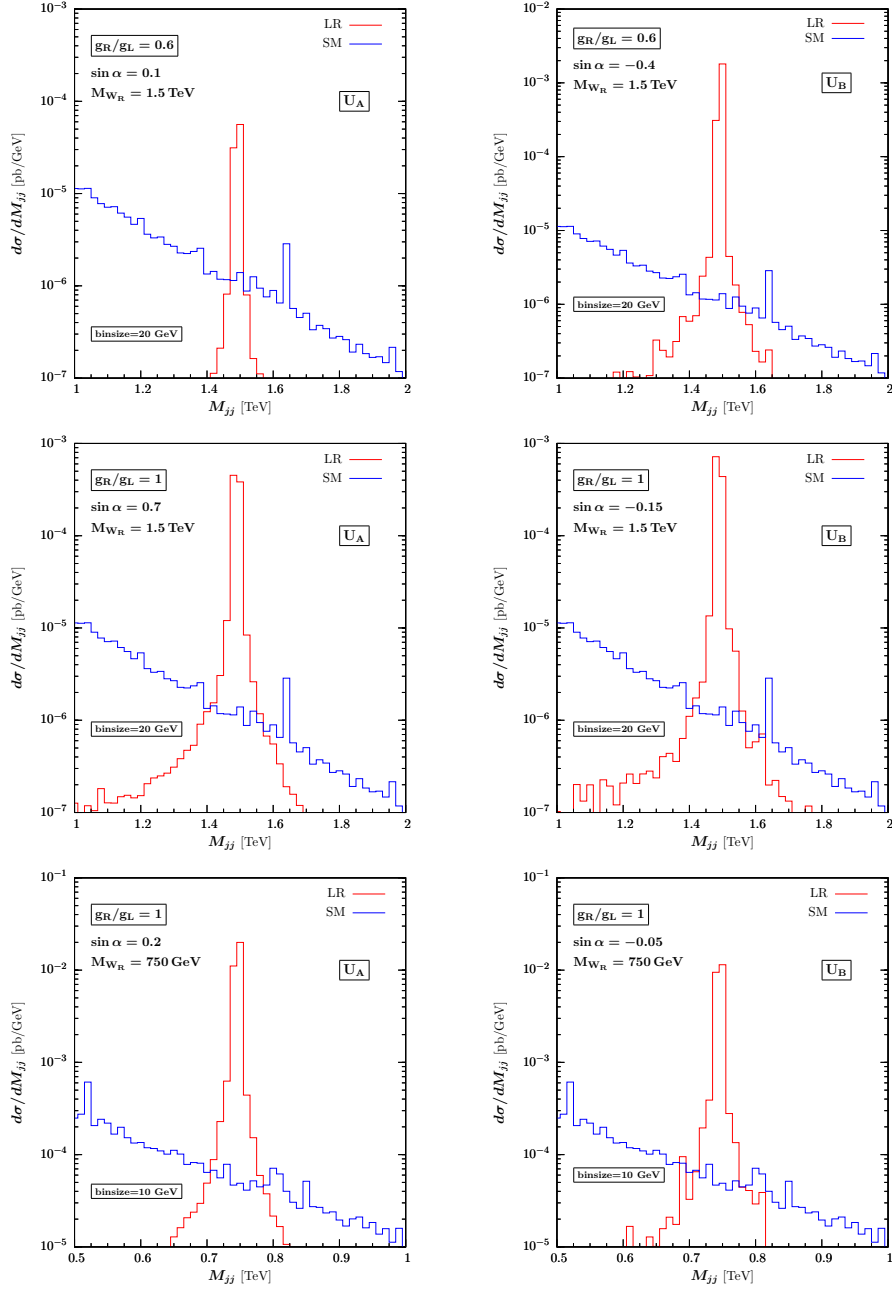


Figure 26:  $W_R$  signal as a resonance in  $dijet$  mass distribution at the LHC ( $\sqrt{s} = 14$  TeV) with  $U_A$  (left column) and  $U_B$  (right column) RCKM parametrizations. The signal is observed in  $p, p \rightarrow t, dijet$  process where only the light quarks are counted as jets. We choose  $binsize = 20$  GeV for intermediate  $M_{W_R} = 1500$  GeV and  $binsize = 10$  GeV for light  $M_{W_R} = 750$  GeV.

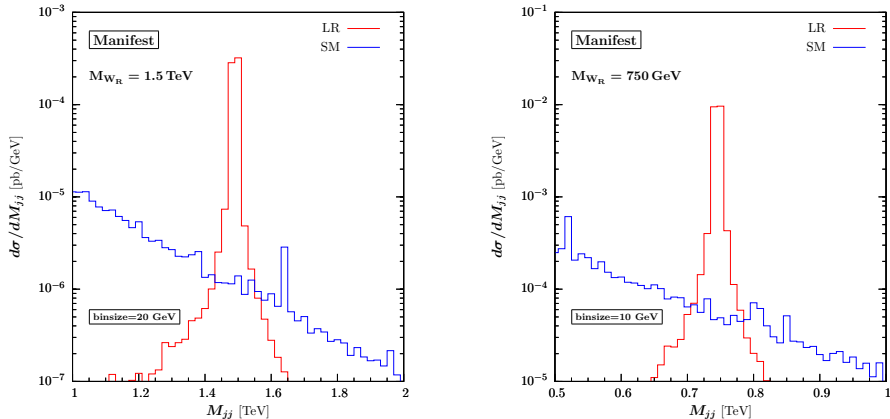


Figure 27: The resonance  $W_R$  signal in the LHC ( $\sqrt{s} = 14$  TeV) with Manifest model. The intermediate  $W_R$  (on left panel) and light  $W_R$  (on right panel) signals are presented. Again the same *binsize* choice with Figure 26.

Whatever the model is, the cross-sections are robust, that is, they are roughly of the same order of magnitude, independent of the model used. The reason is the following: in  $U_A$  and  $U_B$  models there are fewer diagrams contributing to the differential cross sections, but the flavor violation from the right-handed quarks is stronger, whereas in the MLRSM there are more Feynman diagrams contributing to the differential cross section, but the flavor violating interactions in the right-handed sector are weaker. This explains the resemblance of the signals between  $U_A(U_B)$  and the MLRSM. To distinguish among the LR models and to finely pinpoint the origin of the signal requires further detailed analysis with more realistic detector simulations.

### 4.3 Summary

We analyzed the single production, decay and collider signals of  $W_R$  bosons produced in LR symmetric models [98]. We considered models with a general right-handed quark mixing structure (which we call the ALRM), but constrained by the Kaon and B-meson flavor physics. We also compared the results with those of the MLRSM, where  $V_{CKM}^R = V_{CKM}^L$  and the coupling constants in the left and right sectors are equal. In the ALRM there is only one free parameter in the RCKM mixing matrix. Additionally, the charged Higgs and  $W_R$  masses, as well as the ratio of the  $SU(2)_L$  and  $SU(2)_R$  coupling constants, are also free parameters. We included restrictions



on the same parameter space coming from  $B_{d,s}^0 - \bar{B}_{d,s}^0$  mixing and the branching ratio for  $b \rightarrow s\gamma$  [8].

The dominant production mode is in association with a top quark and this has a large background from the single top production (in association with  $W_L$ ) from the SM. However, looking at events in the 500-2000 GeV mass range for  $W_R$ , we show that the SM background is always below the  $W_R$  signal, and we expect a significant peak above the SM background around the  $W_R$  mass (assumed to be in the range considered). Even with a luminosity of  $10 \text{ fb}^{-1}$ , achievable at the LHC within the next 3 years, we expect several events a year, while with  $\mathcal{L} = 100 \text{ fb}^{-1}$ , the events could reach 100 per year. We concentrated our analysis in the  $W_R \rightarrow dijet$  decay mode, where *dijets* are the light quarks  $u, d, s$  and  $c$ .

The cross section for the single  $W_R$  production can reach 10 fb, including all parameter restrictions, and the dominant decay modes are to light quarks,  $\bar{u}d(s)$  being favored by the choice of parametrization, and  $\bar{c}s(d)$  and  $\bar{t}b$  by the restrictions on the RCKM.

Models which predict extra  $W'$  bosons all have features that distinguish them from  $W_R$  bosons in the LRSM. In warped extra-dimensional models [78], the coupling of the extra charged gauge bosons to light quarks and leptons is suppressed relative to those in SM. By contrast, in the LRSM, the decays to leptons might be suppressed for heavy right-handed neutrinos, whereas  $W \rightarrow jet jet$  has no missing energy so the signal can be reconstructed in full. The irreducible SM background from the electroweak process (single top production) is shown to be smaller than the signal inside the resonance region. Warped RS models need luminosities of  $\mathcal{L} = 100$  (1000)  $\text{fb}^{-1}$  for a  $W'$  to reach a statistically significant signal, and expected  $W'$  masses are in the 2-3 TeV region. Technicolor or Composite Higgs [86–88] models are expected to give very similar signals, as the warped extra dimensional model is dual to the 4D strong dynamics involved in electroweak symmetry breaking. In the Little Higgs Models [83–85], the heavy  $W_H$  is left-handed and the partial width to each fermion species is almost the same (for massless fermions). In UED, the additional Kaluza-Klein (KK) W and Z bosons expected to have masses in the 100-200 GeV region [81,82], have their hadronic decays closed, so they decay democratically to all lepton (one KK and one ordinary) flavors.

A clear signal for a charged vector boson will be much more significant than one

for a neutral  $Z'$  boson, as it would restrict the extension of the gauge sector. Our analysis is complementary to previous analysis which indicate how to find whether the extra charged  $W'$  boson is left- or right-handed, by presenting the signals expected for  $W_R$  in the LRSM, both manifest with  $V_{CKM}^R = V_{CKM}^L$  and in a case where  $V_{CKM}^R$ , constrained by B and K phenomenology, is independent of the mixing in the left-handed quark sector and characterized by a single parameter. The signal for such a charged gauge boson is significantly different from that in other scenarios with extra  $W'$ s, and would be an irrefutable signal of LR symmetry.

## Chapter 5

# TOP QUARK PAIR PRODUCTION AND ASYMMETRIES AT THE TEVATRON AND THE LHC IN THE LRSM

Measurements of top production and decays are of particular interest for particle theorists as they likely will shed light on the mechanism of electroweak symmetry breaking. The Tevatron has produced such measurements and more is expected to come from the LHC. For instance, the  $t\bar{t}$  total cross section, as well as the differential cross section with respect to the  $t\bar{t}$  invariant mass, both of which are sensitive to a variety of BSM scenarios of particles decaying into  $t\bar{t}$  pairs, are completely consistent with the SM [99–103].

But recently both the CDF and DØ collaborations have measured the forward-backward asymmetry of the top quark pairs,  $A_{FB}^{t\bar{t}}$  [104–107]. Based on a data sample of  $5.3 \text{ fb}^{-1}$  [105, 106], the asymmetries evolved to the parton level <sup>1</sup> are

---

<sup>1</sup>Here and throughout the chapter, parton-level is used in the meaning described in Reference [105]. It refers to the deconvolution from the data, like detector efficiencies, jet algorithm, selection efficiencies, background etc. See Reference [105] for more details.

$$\begin{aligned}
A^{t\bar{t}}(|\Delta_y| < 1) &= 0.026 \pm 0.118 \quad , \\
A^{t\bar{t}}(|\Delta_y| \geq 1) &= 0.611 \pm 0.256 \quad , \\
A^{t\bar{t}}(M_{t\bar{t}} < 450 \text{ GeV}) &= -0.116 \pm 0.153 \quad , \\
A^{t\bar{t}}(M_{t\bar{t}} \geq 450 \text{ GeV}) &= 0.475 \pm 0.114 \quad ,
\end{aligned}
\tag{5.1}$$

in the  $t\bar{t}$  rest frame (with  $M_t = 175$  GeV). In the SM the asymmetry is produced mainly through one-loop QCD corrections, with a smaller contribution from electroweak  $t\bar{t}$  production, and is stable with respect to corrections from QCD threshold resummation [108]. The NLO SM predictions are, by comparison [109–113]

$$\begin{aligned}
A_{\text{SM}}^{t\bar{t}}(|\Delta_y| < 1) &= 0.039 \pm 0.006 \quad , \\
A_{\text{SM}}^{t\bar{t}}(|\Delta_y| \geq 1) &= 0.123 \pm 0.008 \quad , \\
A_{\text{SM}}^{t\bar{t}}(M_{t\bar{t}} < 450 \text{ GeV}) &= 0.040 \pm 0.006 \quad , \\
A_{\text{SM}}^{t\bar{t}}(M_{t\bar{t}} \geq 450 \text{ GeV}) &= 0.088 \pm 0.013 \quad .
\end{aligned}
\tag{5.2}$$

We note that there has been a recent calculation of the asymmetry including electroweak corrections to  $\mathcal{O}(\alpha^2)$  terms, as well as interferences with the QCD diagrams [114]. It seems that SM asymmetry receives non-negligible same-sign contributions from the electroweak sector so that, except the region with  $M_{t\bar{t}} > 450$  GeV, the observed deviation between theory and experiment diminishes.

As the deviation from the expected and the measured asymmetry is large, this has been interpreted as a signal for New Physics (NP), in particular a signal for a below-TeV scale physics. A large variety of models has been employed to resolve the discrepancy. These models invoke new particles and new interactions to explain the discrepancy. In general, one can classify these models according to the new mediators of the new physics as (1)  $t$ -channel bosons mediators (scalars or vectors, such as  $W'$  or  $Z'$ ) with flavor-violating couplings to right-handed up quarks [115–132], or (2)  $s$ -channel mediators, color sextet or color anti-triplet scalar particles coupling with flavor-violating couplings to up and top quarks, such as [133–153] or (3) new flavor multiplets which coupling to quarks in a flavor-symmetric way [125, 127, 129, 154, 155]. Comparative studies of various models also exist, and it was shown that  $s$ -channel particles used to explain the anomaly have maximal axial couplings, while  $t$ -channel

particles exhibit maximal flavor violating couplings [126, 147, 156–169]. As well, a number of analysis have appeared, which study the implications of models which predict large asymmetry for LHC phenomenology [162, 170–175]. These models have been studied individually, or in a group, to extract some global features which would insure generating a large asymmetry while contributing a negligible amount to the cross section, and to classify general features. A recent analysis [176] concludes that, among scalar mediated-processes, only the  $t$ -channel exchange of a QCD-singlet, weak doublet scalar is consistent with flavor and electroweak constraints, and does not conflict with the collider data obtained so far.

Although these models have been shown to produce a large asymmetry, since all appear designed specifically to resolve this problem, they are sometimes insufficiently justified and thus they seem disconnected from other low energy phenomenology constraints. In all models, the large flavor violation in the  $t-u$  or  $t-d$  quark sectors is enhanced, while flavor changing in the other sectors is suppressed. The question remains of whether such asymmetry can be obtained by employing a known and well-studied NP model. In particular, what the prediction is of such a model (allowing for maximum flexibility) and how important it is for the prediction of the asymmetry to impose the requirement that the model satisfies known phenomenological constraints. We propose to investigate here the effect on the asymmetry and  $t\bar{t}$  production cross section emerging from  $W_R$  and  $Z_R$  bosons in the LRSM. This model satisfies some definite conditions:

- It is one of the simplest and most natural extensions of the SM.
- It contains additional particles in both the  $s$ - and  $t$ -channels which could enhance the forward-backward asymmetry, but also the  $t\bar{t}$  cross section.
- It has been thoroughly investigated and constrained through many analysis, and in particular CDF and DØ have put limits on extra boson masses.
- More information and testing of the model will be provided soon by LHC (some recent bounds from colliders are discussed later).

We first perform an analysis of the  $t\bar{t}$  pair production and forward-backward asymmetry at the Tevatron, then we explore the signal at LHC, for both the cross section and possible asymmetries testable at the LHC. As we wish to allow the model to be as

general as possible, we rely on a generic model, without constraining masses, mixing parameters or gauge couplings, but impose constraints coming from low-energy phenomenology, mainly  $K$  and  $B$  physics, but also collider restrictions coming from the Tevatron. As the LHC data would be available fast, and the constraints on particular models are rapidly changing, we are motivated by the fact that the LHC collaborations are now analyzing unprecedented amounts of top data that will clearly rule out models. Thus a clear expectation of model predictions for the LHC is timely.

The constraints on the parameter space of the left-right model, mostly from flavor violating processes, which are relevant to the study of  $W_R$  phenomenology, come from  $K^0 - \bar{K}^0$  mixing,  $B_d^0 - \bar{B}_d^0$  and  $B_s^0 - \bar{B}_s^0$  mixing, and  $b \rightarrow s\gamma$ . These constraints depend on several parameters and are difficult to summarize analytically; however, they are included in the evaluation of the  $t\bar{t}$  cross section and forward-backward asymmetry, analyzed in the next section.

We also include restrictions imposed by the available data from ATLAS which seems to rule out a  $Z'$  resonance with  $M_{Z'} < 950$  GeV, with the exact limit depending on specific models and specific assumptions [177]. A recent talk at the European Physics Society meeting [178] reports new bounds on  $Z'$  mass, with 50 times more data ( $\sim 2 \text{ fb}^{-1}$ ) and with new bounds varying from 1.5 TeV to 1.8 TeV depending on the models. Similarly there are new bounds from the CMS and DØ collaborations [179, 180] with total integrated luminosity  $1.1 \text{ fb}^{-1}$  and  $5.4 \text{ fb}^{-1}$ , respectively. While the bounds from CMS are very similar to the ones from ATLAS, DØ bounds are somewhat weaker. A relevant study by Nemevsek et al [181–183] on the bound on  $W_R$  mass using the  $33 \text{ pb}^{-1}$  LHC data at 7 TeV reports  $M_{W_R} > 1.4$  TeV, but is also spectrum specific and depends on whether the right-handed neutrino is Majorana or Dirac and whether it is lighter or heavier than  $M_{W_R}$ . We assume the right-handed neutrino heavier than  $M_{W_R}$  so that the above bound is evaded.

For the evaluation of the cross section and the asymmetry, we have chosen two benchmark parameter sets for each of Model A, Model B and MLRSM, defined as previously. To select particular benchmark points, we used the results of our previous parameter scans over  $M_{W_R}$ ,  $\sin \alpha$ ,  $M_{H^\pm}$  and  $g_R/g_L$  in [8, 98] where we have presented restrictions over the parameter space obtained by imposing low energy constraints from meson mixings and  $b \rightarrow s\gamma$  branching ratio, as well as collider constraints on production of extra gauge bosons. The parameter scan leaves very small allowed

regions where the  $W_R$  is light, and/or the flavor violation from the right-handed sector is significant. These points are chosen to maximize flavor-violation in the right-handed quark sector, for both light and heavy  $M_{W_R}$  scenarios. The parameter sets for each model, namely Set I and Set II, that are used in our calculations in accordance with those constraints are given in Table 4. We include, in addition to the Set I and Set II, a left-right scenario for each of the three models which is not subjected to experimental constraints, which we call the *Unconstrained LR Set*. We require that this model is roughly consistent with collider limits on the  $t\bar{t}$  cross section. Our aim is to show the effects of experimental restrictions on the parameter space and highlight that “relaxing” them can produce large asymmetries.

	Manifest			Model A			Model B		
	Set I	Set II	Uncons	Set I	Set II	Uncons	Set I	Set II	Uncons
$M_{W_R}(\text{GeV})$	700	1500	500	700	1000	500	1100	1300	500
$M_{Z_R}(\text{GeV})$	1172	2511	837	2189	1674	734	3441	2176	734
$g_R/g_L$	1	1	1	0.6	1	2	0.6	1	2
$\sin \alpha$	-	-	-	0.5	0.25	0.7	-0.2	-0.1	0.7

Table 4: Benchmark points Set I, Set II and Unconstrained for left-right symmetric models: Manifest, Model A, and Model B, used throughout the analysis. Note that  $M_{Z_R}$  is fixed when a value for  $M_{W_R}$  is chosen but the  $M_{Z_R}$  values are included for reference.

## 5.1 $t\bar{t}$ Cross Section and Forward-Backward Asymmetries at the Tevatron

The top quark pair production in  $p\bar{p}$  collisions is mostly accomplished through  $s$ -channel quark-antiquark annihilation (about 90%) and much less so through  $gg$  and  $qg$  processes. The latest CDF and DØ measurements of the cross section [100–102] agree with the SM at the next-to-next-to-leading order (NNLO) prediction [184–186],

$$\sigma_{(p\bar{p} \rightarrow t\bar{t})}^{\text{CDF II}} = 7.50 \pm 0.48 \text{ pb} \quad , \quad (5.3)$$

$$\sigma_{(p\bar{p} \rightarrow t\bar{t})}^{\text{NNLO}} = 7.39 \pm 0.55 \text{ pb} \quad . \quad (5.4)$$

We proceed to analyze the top-pair cross sections in the left-right models. For consistency, we evaluate here the cross section in the SM, as well as in the LR models under scrutiny: the MLRSM, Model A and Model B, for the Set I and Set II for each model and, by comparison, for the Unconstrained set. Any new model must predict a cross section which agrees with the experimental data, as the cross section is particularly sensitive to  $s$ -channel exotic resonances, thus restricting the mass of the  $Z_R$  boson in LR models.

In the calculation of  $t\bar{t}$  production cross-sections we proceed as follows. We first calculate the LO cross-sections at  $\sqrt{s} = 1.96$  TeV with  $m_t = 172.5$  GeV, using CTEQ6M parton distribution function (PDF) set to go from parton to  $p\bar{p}$  cross sections. We then calculate the NNLO cross section by multiplying the LO result with the  $K$  factor ( $K = 1.3$  for Tevatron [184–186]) as in the SM. We assume for simplicity that the  $K$ -factors are universal, so that the NP/SM ratios at LO and NNLO are the same, minimizing the impact of the NNLO corrections to the LR model contributions (See our comments in the next paragraph). We list the cross sections obtained in Table 5.

$\sigma_{\text{SM}}(\text{pb})$	$7.36 \pm 0.007$		
	Set I	Set II	Uncons.
$\sigma_{\text{Man}}(\text{pb})$	$7.37 \pm 0.007$	$7.37 \pm 0.007$	$7.43 \pm 0.008$
$\sigma_{\text{ModA}}(\text{pb})$	$7.36 \pm 0.007$	$7.37 \pm 0.007$	$8.35 \pm 0.008$
$\sigma_{\text{ModB}}(\text{pb})$	$7.36 \pm 0.007$	$7.36 \pm 0.007$	$8.17 \pm 0.008$

Table 5: The NNLO  $t\bar{t}$  production cross-sections at the Tevatron ( $\sqrt{s} = 1.96$  TeV) for the SM, and Left-Right models: Manifest, Model A and Model B, for the benchmark points chosen.

The CDF and  $D\bar{O}$  results impose that in addition to the total production cross section of  $t\bar{t}$ , the differential cross section with respect to the invariant mass of  $t\bar{t}$  should also agree with the SM prediction. Thus, in Figure 28 we graph the differential cross sections in LR models with respect to the  $t\bar{t}$  invariant mass distributions and compare our calculation with the CDF II measurement. In the three panels of Figure 28 we show in sequence the differential cross sections for the Manifest, Model A and Model B for the two parameter sets Set I (red), Set II (green) as well as the



Unconstrained Set (blue). The CDF data is given as black lines, and includes uncertainties in each bin. Note that care must be taken when comparing the new physics cross-sections against the SM cross-section, as the selection efficiencies for NP models can be lower. The predicted NNLO SM cross-section requires a SM  $K$ -factor of 1.3, while the NNLO corrections to the new physics have not been calculated, so any comparison between the observed cross-section and the  $t\bar{t}$  production cross-section is subject to some uncertainty [187]. Comparing our results to the central value of the combined CDF  $t\bar{t}$  production cross-section to the cross-section of SM plus new physics for all three parameters sets show fairly good agreement with the  $M_{t\bar{t}}$  distribution measured by CDF II, and given our comments above, it probably may yield even better agreement. Thus we insured that, for the parameters chosen, both the total and the differential cross sections are consistent with the data. Note, however, the slight enhancement of the differential cross section in the Unconstrained set for  $M_{t\bar{t}} > 500$  GeV, due to low  $M_{Z_R} = 734$  GeV for Models A and B. The increase is shifted and (not seen due to an uneven bin choice) for the Unconstrained set of the Manifest model, where  $M_{Z_R} = 837$  GeV.

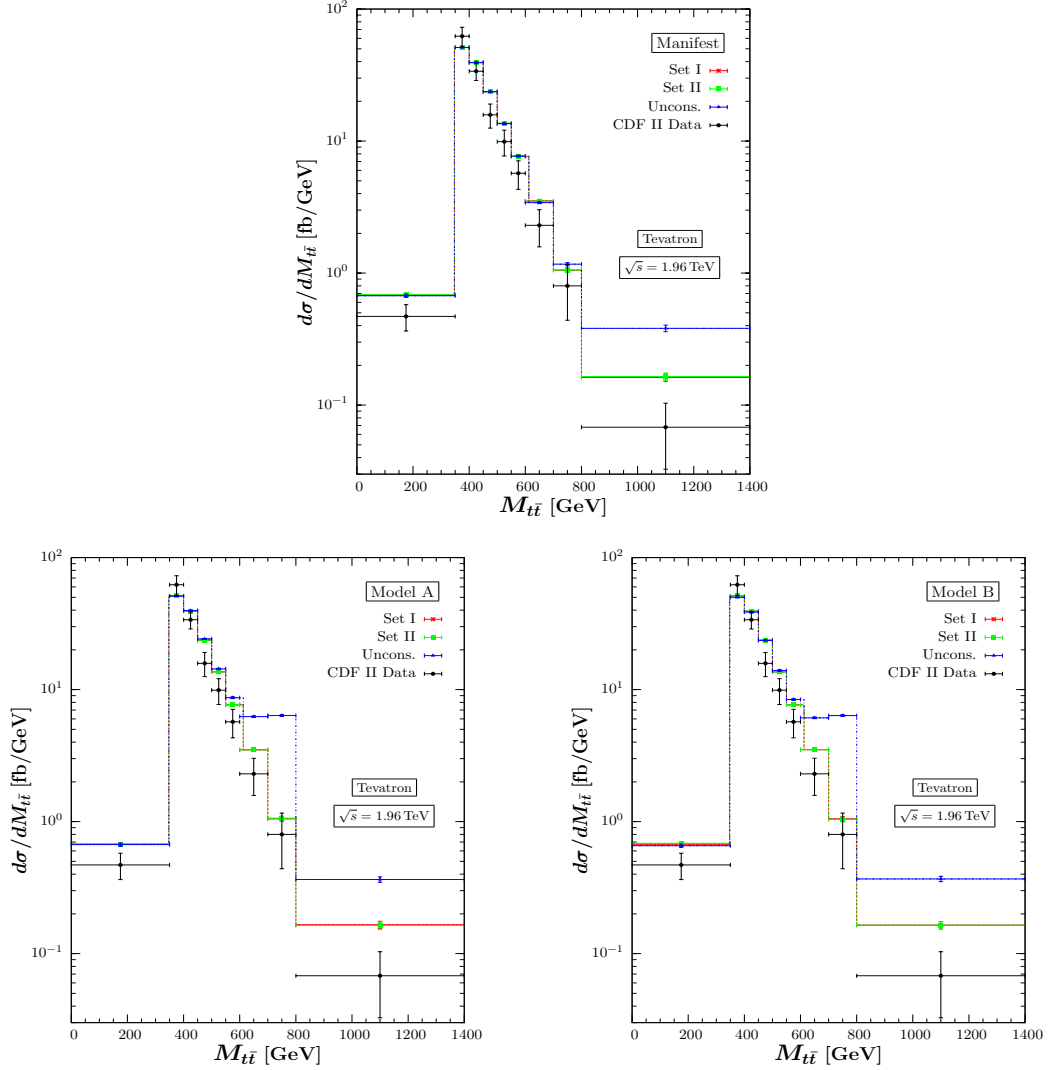


Figure 28:  $t\bar{t}$  invariant mass distribution of differential cross section in Manifest LR model (upper panel), Model A (lower left panel) and Model B (lower right panel) in comparison with CDF II  $5.3 \text{ fb}^{-1}$  data. The parameter sets (Set I, Set II and Unconstrained Set) for each model are given in Table 4.

We proceed next by examining the asymmetry in the production and decays of the  $t\bar{t}$  system. The forward-backward asymmetry of top quark pairs ( $\mathcal{A}_{FB}^{t\bar{t}}$ ) in  $p\bar{p}$  collisions is seen as a precision test of the SM. The  $t\bar{t}$  pair production in SM at the lowest order is symmetric under charge conjugation. At NLO, the interference of QCD processes involving initial and final state gluon emission  $q\bar{q} \rightarrow t\bar{t}g$  and  $qg \rightarrow t\bar{t}q$  will exhibit a small forward-backward asymmetry. The NLO calculations in the SM yield an asymmetry due to virtual corrections arising from interference effects, which

are opposite in sign and larger than the real emission component.

The forward-backward asymmetry is defined in terms of top quark rapidities as

$$\mathcal{A}_{FB} = \frac{N(\Delta_y > 0) - N(\Delta_y < 0)}{N(\Delta_y > 0) + N(\Delta_y < 0)} \quad , \quad (5.5)$$

where  $\Delta_y = y_t - y_{\bar{t}}$  is the difference of top and anti-top rapidities and  $N$  is the number of events in the forward ( $\Delta_y > 0$ ) and backward ( $\Delta_y < 0$ ) regions. While the cross sections measured by CDF and DØ agree with the SM expectations, the measured asymmetries deviate from the NLO SM calculation, by as much as 50% in the large  $M_{t\bar{t}}$  invariant mass bin. It is the challenge of any new BSM to generate the asymmetry without disturbing the cross section; it is our intention to verify if this is possible for a realistic left-right model.

We proceed as follows. Since the kinematical cuts in Tevatron analysis are very restrictive, we generate 5 million signal events in order to minimize the statistical errors. We generate events with CalchEP 3.1 [97] using CTEQ6M PDFs. The factorization and renormalization scales  $\mu_F = \mu_R = m_t$  are used, and we take the top quark mass  $m_t = 172.5$  GeV. We use Pythia 6.4.18 [188] for showering and PGS 4 [189] for jet reconstruction,  $b$ -tagging and a rough detector simulation.

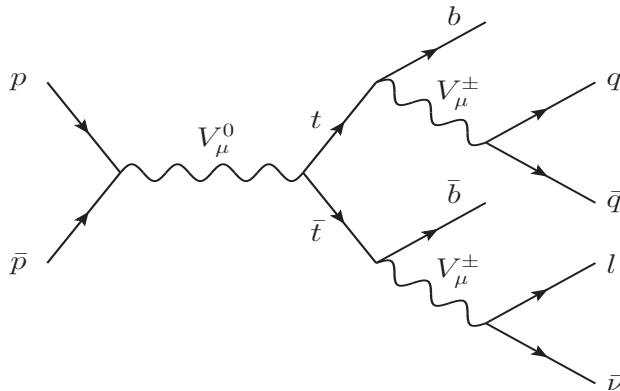


Figure 29:  $t\bar{t}$  production and decay topology in hadronic and semileptonic events.  $V_\mu^0$  represents neutral gauge bosons  $\gamma, g, Z, Z_R$  and  $V_\mu^\pm$  the charged ones,  $W_L^\pm, W_R^\pm$ . The diagram with the top quark decaying hadronically is shown but both possibilities are included.

We start the analysis by producing the  $t\bar{t}$  pair, then decaying top quarks semileptonically and hadronically. We concentrate our analysis on the *lepton + jets* topology, where one top quark decays semileptonically ( $t \rightarrow b\nu$ ) and the other hadronically

( $t \rightarrow bq\bar{q}'$ ), as in Figure 29. We select events with one single lepton (electron or muon) plus missing energy to account for the associated neutrino and a minimum of 4 jets with one jet  $b$ -tagged and with the following kinematical cuts,

$$\begin{aligned}
|\eta^l| < 1 & \quad , \quad |\eta^j| < 2 \quad , \\
p_T^l > 20 \text{ GeV} & \quad , \quad p_T^j > 20 \text{ GeV} \quad , \\
\not{E}_T \geq 20 \text{ GeV} & \quad , \quad |\eta^b| < 1 \quad ,
\end{aligned}
\tag{5.6}$$

where  $l, j, b$  denote lepton ( $e, \mu$ ), jet ( $u, d, c, s$ ) and  $b$ -quark parameters, respectively. The jets are reconstructed using a cone algorithm with  $\Delta R = \sqrt{\Delta\phi^2 + \Delta\eta^2} < 0.4$ . Here  $b$ -jets, tagged with the loose **SECVTX** algorithm, are restricted to  $|\eta^b| < 1$ . We used the default  $b$ -tagging efficiency and functions for Tevatron given in **PGS 4**. The efficiency of the signal to pass through the cuts (after showering, clustering and detector simulations) allows only 2% signal events to survive the kinematical cuts to yield the forward-backward asymmetries.

The number of events are scaled to the NNLO cross sections using the standard  $K$ -factor for the Tevatron. We have calculated left-right contribution at the LO (including the LO SM, LR and the interference between the two) to the asymmetries. We have listed asymmetries obtained for the four different regions, for all models studied in Table 6. The first two rows are parton level asymmetries, the first row obtained by unfolding the CDF data and the second for the MCFM. The remaining rows compare the CDF signal data to our various models<sup>2</sup>. As it is seen from the Table 6, the LO left-right contributions to the asymmetries are relatively small. The results might have been enhanced if the left-right contributions were calculated at the NLO which is beyond the scope of this work. We have chosen to compare our results, simulated to the final states, with the CDF signal. The reason is that the errors in the signal results are much smaller than the ones evolved to parton level, and thus this comparison gives a better measure of the deviation of our results from the data. We include a reduced  $\chi^2$  analysis as a measure of how well the models perform.

It is apparent from Table 6 that, while the models yield a slightly enhanced forward-backward asymmetry in one region, and others in different regions, none of the phenomenologically viable LR models can reproduce large enough anomaly seen at the Tevatron. The results for the benchmark points chosen for Manifest,

---

<sup>2</sup>In fact, the signal level data for the regions  $|\Delta_y| \geq 1$  or  $|\Delta_y| \leq 1$  are not presented in [105]. So, we have used the data-level values including the background.

Model A and Model B are however fairly consistent in the both sign and size of the anomaly. Moreover the asymmetry seems to depend sensitively on  $M_{W_R}$  and on the ratio  $g_R/g_L$ , but to a lesser extent on  $\sin\alpha$ , the measure of flavor violation in the right-quark sector. From our previous investigations of the parameter space we know that  $M_{W_R}$  and  $g_R/g_L$  are closely correlated, as a decrease or increase in one forces a decrease or increase in the other to satisfy low energy constraints. We are thus confident that results the sets chosen are a true indication LR model predictions. As sets I and II represent very different regions of the parameter space, and different variants of the model, this is further confirmation that our results are robust and do not depend on the specific points chosen in the parameter space of the LR model. One can obtain higher asymmetries (consistent with the data) in a LR model not subjected to experimental constraints (last three rows in Table 6), as indeed is the case for models constructed specifically to explain the asymmetry.

		$A_{FB}^{t\bar{t}}$ $ \Delta_y  < 1$	$A_{FB}^{t\bar{t}}$ $ \Delta_y  \geq 1$	$A_{FB}^{t\bar{t}}$ $M_{t\bar{t}} < 450 \text{ GeV}$	$A_{FB}^{t\bar{t}}$ $M_{t\bar{t}} \geq 450 \text{ GeV}$	$\chi_{red}^2$ (4 d.o.f.)
CDF(parton-level)		$0.026 \pm 0.118$	$0.611 \pm 0.256$	$-0.116 \pm 0.153$	$0.475 \pm 0.114$	
MCFM(parton-level)		$0.039 \pm 0.006$	$0.123 \pm 0.008$	$0.040 \pm 0.006$	$0.088 \pm 0.013$	
CDF(signal-level)		$0.021 \pm 0.031$	$0.208 \pm 0.062$	$-0.022 \pm 0.043$	$0.266 \pm 0.062$	
LR	Manifest-I	0.0025	0.0174	0.0030	0.0086	6.8
	Manifest-II	0.0098	0.0162	0.0091	0.0137	6.7
	Model A-I	0.0063	0.0143	0.0065	0.0096	6.9
	Model A-II	0.0043	0.0131	0.0051	0.0072	7.0
	Model B-I	0.0077	0.0121	0.0062	0.0118	6.9
	Model B-II	0.0035	0.0038	0.0029	0.0044	7.3
Uncons. LR	Manifest	0.0065	0.0280	0.0024	0.0222	6.1
	Model A	0.0532	0.2400	0.0078	0.1832	0.9
	Model B	0.0444	0.2189	-0.0084	0.1751	0.7

Table 6: The Forward-Backward Asymmetry at the Tevatron in the SM, and in LR models: Manifest, Model A and Model B, compared with the CDF data. We include, in the first two rows, the unfolded CDF results and the MCFM calculation. Parameter sets (Set I, Set II and Unconstrained) for each model are given in the Table 4.

We proceed to investigate the features of the signal in LR models. In Figure 30 we show the distributions of rapidity differences  $\Delta_y$  in the upper row, and top quark rapidity  $y_t$  in lower row, for three different LR models. In order to generate a large asymmetry in the high invariant mass bin, the rapidity must be increased and

skewed significantly with respect to the SM distribution. Additional high mass gauge bosons could sometimes produce this effect. We show the Manifest model (left panel), Model A (middle panel) and Model B (right panel) with Set I (blue) Set II (green) the Unconstrained (red) and the SM (black) in each panel. We did not perform a global fit to the data, as our results do not agree with the CDF measurements. The Unconstrained Set shows only modest increases with respect to the other models. The results are however consistent among the different models obeying low energy constraints, and parameters sets chosen, at least making the left-right model very predictable.

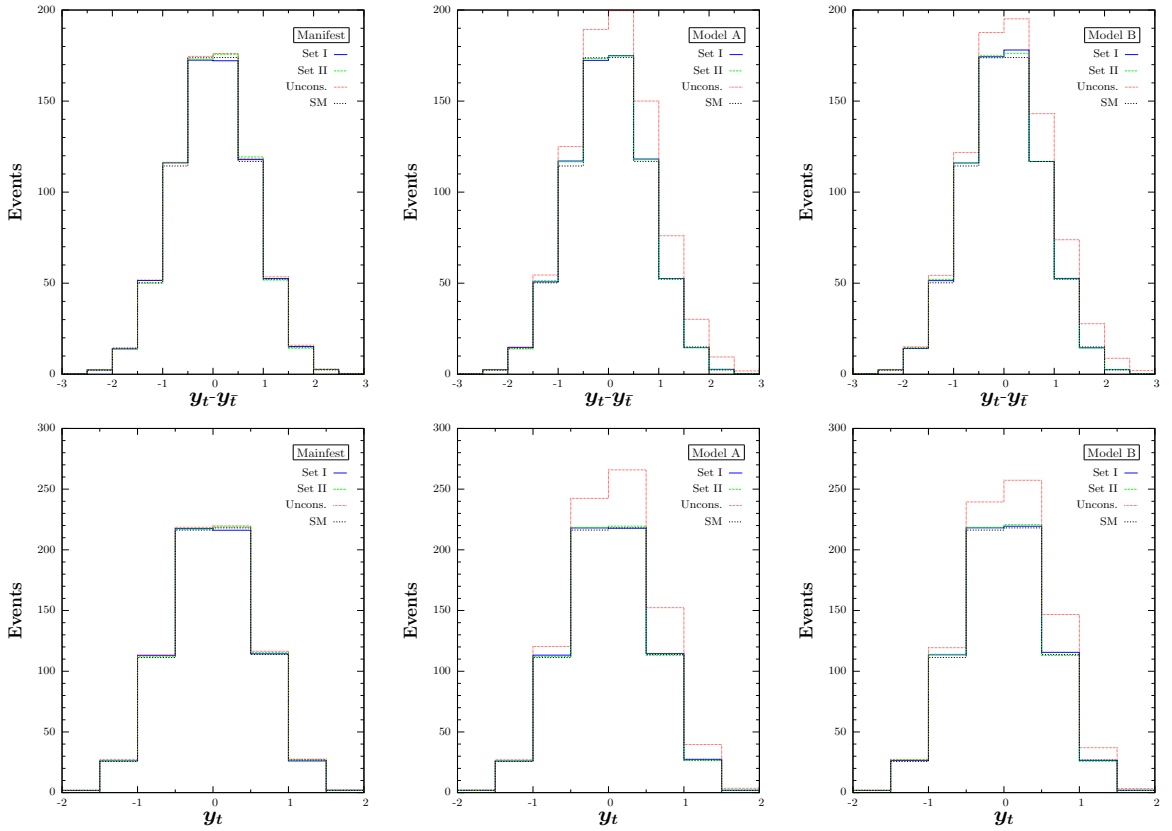


Figure 30:  $\Delta_y$ (upper row) and  $y_t$ (lower row) distributions in Manifest LR model (left panel), Model A (middle panel) and Model B (right panel) at the Tevatron. Parameter sets (Set I, Set II and Unconstrained) for each model are given in the Table 4.

In Figure 31 we give invariant mass distributions in *Pythia* of LR models at the Tevatron, for the Manifest LR model (left panel), Model A (middle panel) and

Model B (right panel). The number of events are scaled to NNLO cross sections with standard  $K$ -factor. Comparison with the SM expectations again shows consistency.

Both this figure and the previous one show that realistic LR models, which obey low-energy constraints, cannot yield the measured CDF asymmetry. The Unconstrained model shows an increase in the differential cross section, corresponding to a  $Z_R$  peak around 734 GeV in Models A and B, and a less pronounced one at 837 GeV in the Manifest left-right case. These are close to the experimental limit at the Tevatron and the first two are likely already ruled out. Changing the ratio  $g_R/g_L$  and lowering the  $W_R$  mass may be able to achieve consistency of left-right models with the asymmetry data, but these models do not satisfy other phenomenological constraints and are thus unrealistic.

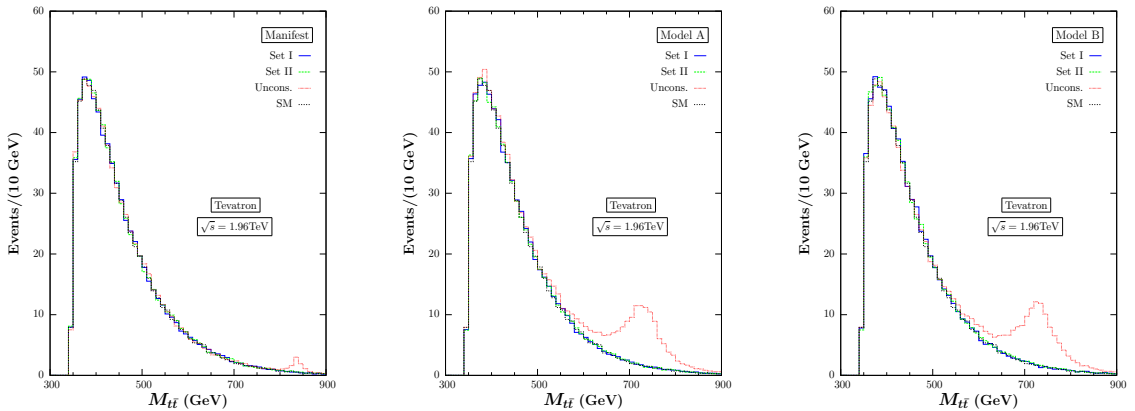


Figure 31:  $t\bar{t}$  invariant mass distributions at the Tevatron in Manifest LR model (left panel), Model A (middle panel) and Model B (right panel) in comparison with the SM. Parameter sets (Set I, Set II and Unconstrained) of each model are given in the Table 4.

## 5.2 $t\bar{t}$ Cross Section and Forward-Central Charge Asymmetries at the LHC

As the Tevatron results show interesting discrepancies with the SM expectation, it is important to evaluate the asymmetries and cross sections for  $t\bar{t}$  production at the LHC. Naturally one might ask is such a pursuit is worthwhile, as we have shown in the previous section that the model cannot explain the Tevatron asymmetries. The large forward-backward asymmetry at the Tevatron, although an exciting signal

for new physics, may not arise from new interactions or new particles. It could arise from a kinematical enhancement of the  $t\bar{t}$  pair, or from a hidden sector. Even the experimental situation at the Tevatron is not yet clear, as the errors on the measurements are significant; also the CDF results show a strong mass dependence of the asymmetry not confirmed by the  $D\bar{O}$  measurements. At LHC different production mechanisms dominate and other asymmetries are at play. Measurements of the charge asymmetry at CMS and ATLAS at the LHC (which appear to be small and negative, though perhaps the uncertainties are too large to make a firm statement) are hard to reconcile with the Tevatron results. Predictions for both colliders are important to understand the dynamics of different gauge symmetries and their effect on different asymmetries. This is particularly interesting for our model, which can reproduce the Tevatron cross section but not the asymmetry. The natural question is: what is the prediction for the LHC? While the Tevatron has collected about a thousand tops, the LHC, even with  $\mathcal{L} = 1 \text{ fb}^{-1}$  has amassed almost an order of magnitude more, making the errors in the production cross section at  $\sqrt{s} = 7 \text{ TeV}$  already competitive with those at the Tevatron with  $\mathcal{L} = 5.3 \text{ pb}^{-1}$ , while the invariant mass  $M_{t\bar{t}}$  investigated extends to 2.5 TeV (with  $200 \text{ pb}^{-1}$ ), versus 1.8 TeV for the Tevatron. LHC will provide measurements of top quark properties, shedding light on models on NP and electroweak symmetry breaking. Agreement or disagreement with this data would open (or perhaps narrow) questions about the validity or restrictions of the model. For example, the CMS Collaboration has recently presented the first measurement of charge asymmetry in  $t\bar{t}$  production [190]

$$\begin{aligned} A_C^\eta &= -0.016 \pm 0.030(\text{stat})_{-0.019}^{+0.010}(\text{syst}) \quad , \\ A_C^y &= -0.013 \pm 0.026(\text{stat})_{-0.021}^{+0.026}(\text{syst}) \quad . \end{aligned} \quad (5.7)$$

The first one based on pseudo-rapidities ( $\eta$ ), the second on the rapidity ( $y$ ) of the two top quarks, while the combined ( $e + jets$  and  $\mu + jets$  channels) ATLAS [191] result is

$$A_C = -0.024 \pm 0.016(\text{stat}) \pm 0.023(\text{syst}) \quad . \quad (5.8)$$

As seen, the result has so far large statistical uncertainties, but this uncertainty is expected to decrease with more data, while the systematic one will improve with improved detector simulation.



The Tevatron, however, is a better machine for measuring the forward-backward asymmetry. At the Tevatron, the forward-backward asymmetry measures the tendency of the top quark (in the  $t\bar{t}$  pair) to move along the direction of the incoming quark rather than along the direction of the incoming anti-quark. At LHC, the measurement of any asymmetry is very subtle. Its charge-symmetric initial state ( $pp$ , or the dominant  $gg, qq$  partonic level channels) does not provide a framework to differentiate between initial partons in the  $t\bar{t}$  production. To define an asymmetry one must rely on sub-leading contributions to the  $t\bar{t}$  production cross section from  $q\bar{q}$  and  $qg$ , with different partons in the initial state. In this case, the forward backward asymmetry represents a charge asymmetry in the decay  $q\bar{q}, qg \rightarrow t\bar{t} + X$  [162,170–175], though several other types of asymmetries have been defined [192] and used to discriminate between BSM models.

We proceed to analyze the properties of the left-right model in top pair production and decays. We evaluate the  $t\bar{t}$  production at the LHC following the same procedure used in the previous section to analyze the signal at the Tevatron. First, we estimate the total and differential cross section for  $t\bar{t}$  production for the models under investigation, then we proceed to define and analyze the charge asymmetry.

At the LHC, the  $t\bar{t}$  production is dominated by gluon fusion in  $pp$  collisions. In our calculation we implement the models in `CalcHEP 3.1` for the evaluation of production cross sections at LO level. We normalize the cross sections to NNLO using the NNLO K-factor ( $K = 1.6$  for LHC) and we present them in Table 7 for both  $\sqrt{s} = 7$  TeV and  $\sqrt{s} = 14$  TeV, for the same parameter sets and models as discussed in the previous section and given explicitly in Table 4. While the SM and Manifest LR model are completely consistent for both Set I and Set II parameters, Models A and B predict a slightly smaller (about 8%) production cross section (but consistent for both Set I and II), all of which agree with the measured value (including errors) at ATLAS at  $\sqrt{s} = 7$  TeV [193] and with the SM predictions at NNLO [184–186],

$$\begin{aligned}\sigma_{t\bar{t}}^{ATLAS} &= 145 \pm 31_{-27}^{+42} \text{ pb} \ , \\ \sigma_{t\bar{t}}^{NNLO} &= 150 \text{ pb} \ ,\end{aligned}\tag{5.9}$$

while the prediction for the cross section in the SM at NNLO at  $\sqrt{s} = 14$  TeV is  $\sigma_{t\bar{t}}^{NNLO} = 919 \pm 4$  pb [184–186]. A complete analysis of the production cross section should include subsequent decays of the top quark, as only a detailed analysis would

be able to conclude if one can distinguish various scenarios. We present below some details of our analysis.

$\sigma_{\text{SM}}(7 \text{ TeV})(\text{pb})$	$167 \pm 0.17$		
$\sigma_{\text{SM}}(14 \text{ TeV})(\text{pb})$	$921 \pm 1.20$		
	Set I	Set II	Uncons.
$\sigma_{\text{Man}}(7 \text{ TeV})(\text{pb})$	$168 \pm 0.23$	$168 \pm 0.20$	$169 \pm 0.19$
$\sigma_{\text{ModA}}(7 \text{ TeV})(\text{pb})$	$168 \pm 0.12$	$168 \pm 0.14$	$179 \pm 0.11$
$\sigma_{\text{ModB}}(7 \text{ TeV})(\text{pb})$	$168 \pm 0.15$	$168 \pm 0.12$	$178 \pm 0.10$
$\sigma_{\text{Man}}(14 \text{ TeV})(\text{pb})$	$924 \pm 1.99$	$923 \pm 2.30$	$926 \pm 1.41$
$\sigma_{\text{ModA}}(14 \text{ TeV})(\text{pb})$	$922 \pm 1.33$	$921 \pm 1.46$	$967 \pm 1.82$
$\sigma_{\text{ModB}}(14 \text{ TeV})(\text{pb})$	$919 \pm 1.31$	$921 \pm 1.04$	$962 \pm 1.52$

Table 7:  $t\bar{t}$  production cross-sections at the LHC for both  $\sqrt{s} = 7 \text{ TeV}$  and  $\sqrt{s} = 14 \text{ TeV}$ .

In Figure 32 we show the number of events in the invariant mass distributions for  $t\bar{t}$  obtained after imposing detector cuts and passing through the detector simulation, in the Manifest LR model (left panel), Model A (middle panel) and Model B (right panel) at the LHC with  $\sqrt{s} = 7 \text{ TeV}$  (upper row) and  $\sqrt{s} = 14 \text{ TeV}$  (lower row), where we distinguish between Sets I, II, Unconstrained and the SM as before. These events are then used to evaluate the charge asymmetries at the LHC. The events generated are consistent among the models studied, and show a modest bump for the unconstrained model corresponding to the  $Z_R$  resonance production. It is evident from the figure that the  $M_{t\bar{t}}$  invariant mass distribution for all models chosen is the same, and indistinguishable from the one in the SM. The important distinction lies in the possible discovery of a  $Z' = Z_R$  boson, which in the Manifest LR model Set I has a mass of 1200 GeV, as well as the ones around 730-830 GeV for the Unconstrained sets (depending on the model considered). These appear as a resonance bump in  $t\bar{t}$  production. For the Set I and Set II of Model A and Model B, the resonances are heavier and out of the  $M_{t\bar{t}}$  range presented.

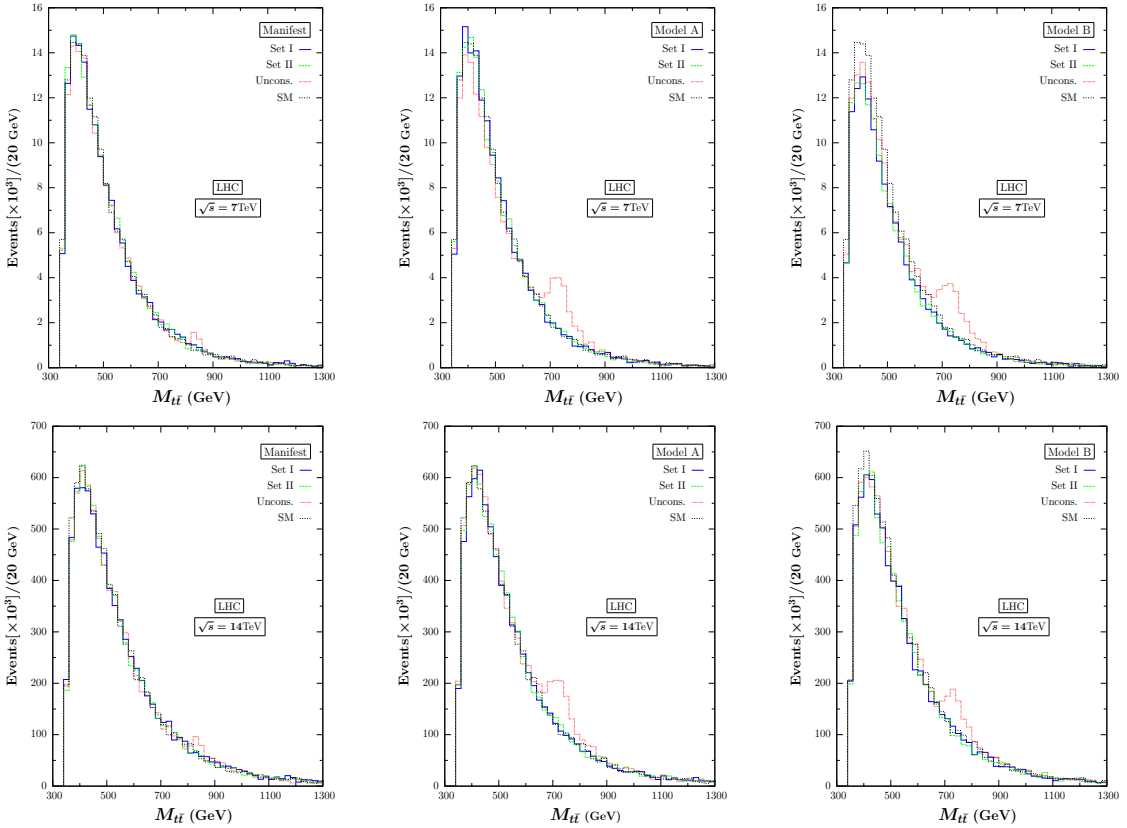


Figure 32: Events in the  $t\bar{t}$  invariant mass distributions at LHC in MLRSM (left panel), Model A (middle panel) and Model B (right panel) in comparison with the SM. Top row shows the distribution for  $\sqrt{s} = 7$  TeV, the bottom row is for  $\sqrt{s} = 14$  TeV. Parameter sets (Set I, Set II and Unconstrained) for each model are given in the Table 4.

We proceed to the evaluation of the asymmetries at the LHC. As previously mentioned, due to the  $pp$  initial state,  $t\bar{t}$  asymmetries at the LHC can be defined as forward and central charge asymmetries. The division of top quark rapidity  $y_t$  between forward and central regions of the detector distinguishes the two asymmetries. The separation parameter  $y_0$  defines the forward  $|y_t| > y_0$  and central  $|y_t| < y_0$  regions of the detector. As an optimum choice of separation parameter we use  $y_0 = 1.5$  [162, 170–175]. We define the forward charge asymmetry by

$$\mathcal{A}_F(y_0) = \frac{N_t(y_0 < |y| < 2.5) - N_{\bar{t}}(y_0 < |y| < 2.5)}{N_t(y_0 < |y| < 2.5) + N_{\bar{t}}(y_0 < |y| < 2.5)}, \quad (5.10)$$

and the central charge asymmetry by

$$\mathcal{A}_C(y_0) = \frac{N_t(|y| < y_0) - N_{\bar{t}}(|y| < y_0)}{N_t(|y| < y_0) + N_{\bar{t}}(|y| < y_0)} , \quad (5.11)$$

where  $N_{t(\bar{t})}$  represent the number of top (anti-top) quarks with given asymmetry. To calculate the asymmetries, we used the same procedure as in the case of the Tevatron, employing `CalcHEP-Pythia-PGS` for event generation, parton showering, jet reconstruction and detector simulation. For the analysis we used the same *lepton + jets* topology with one semileptonic and one hadronic top decays. We proceed by selecting single lepton events with an associated neutrino and a minimum 2 jets with at least one  $b$ -quark tagged. We imposed the following kinematical cuts for event selection at the LHC (using the same symbols as before)

$$\begin{aligned} |\eta^l| < 2.5 & \quad , & |\eta^j| < 2 , \\ p_T^l > 15 \text{ GeV} & \quad , & p_T^j > 20 \text{ GeV} , \\ \cancel{E}_T \geq 20 \text{ GeV} & \quad , & |\eta^b| < 1 . \end{aligned} \quad (5.12)$$

The jets are reconstructed using a cone algorithm with  $\Delta R = \sqrt{\Delta\phi^2 + \Delta\eta^2} < 0.5$ . Here again  $b$ - jets, tagged with the loose `SECVTX` algorithm, are restricted to  $|\eta^b| < 1$ . Please note that  $b$ -tagging efficiency and functions given in `PGS 4` are based on Tevatron parameters. Thus we follow the procedure given in [194] to update the  $b$ -tagging functions according to the Equation (2) of [194]. In the LHC analysis jet events are much more energetic due to the high center of mass energy of the collision, and thus the jet reconstruction algorithm in `PGS 4` consumes huge amount of computing time. Since the kinematical cuts are fairly relaxed in the LHC case, we have chosen lesser amount of events ( $2 \times 10^5$ ) simulated for every asymmetry evaluation with reasonable statistical errors. After imposing all the detector cuts, the asymmetries are calculated using the 10% signal events surviving. The calculation for the LHC asymmetry in the SM as well as LR models is based on simulating events normalized to the cross sections at NNLO level by using the standard K-factor. The results are shown in Table 8. The asymmetries are very small, and the asymmetries in LR models can have different signs than in the SM, although unfortunately this seems highly parameter-dependent. At this point, these asymmetries appear consistent (of the same size) with the ATLAS and CMS measurements and most tend to be small and negative. To make a more definite statement, one must wait for more precise

experimental data. The LHC results are obtained over the whole rapidity parameter values, while our results are divided into regions for better understanding of model dynamics. The experimental results have large uncertainties, making them not yet very predictable; a higher luminosity might change that. The charge asymmetry changes sign when measured in the forward region from the one measured in the central region of the detector in both SM and LR models.

		$A_C^{t\bar{t}}(7 \text{ TeV})$ $0 <  y  < 1.5$	$A_F^{t\bar{t}}(7 \text{ TeV})$ $1.5 \leq  y  < 2.5$	$A_C^{t\bar{t}}(14 \text{ TeV})$ $0 <  y  < 1.5$	$A_F^{t\bar{t}}(14 \text{ TeV})$ $1.5 \leq  y  < 2.5$
SM		-0.0024	0.0157	0.0011	-0.0028
LR	Manifest-I	-0.0014	0.0097	-0.0035	0.0050
	Manifest-II	0.0013	-0.0091	-0.0031	0.0133
	Model A-I	-0.0045	0.0236	0.0002	-0.0035
	Model A-II	-0.0020	0.0127	0.0033	-0.0234
	Model B-I	0.0021	-0.0142	-0.0002	0.0003
	Model B-II	-0.0001	-0.0038	-0.0053	0.0179
Uncons LR	Manifest	-0.0013	0.0063	-0.0084	0.0260
	ModelA	-0.0117	0.0650	-0.0063	0.0217
	ModelB	-0.0087	0.0469	-0.0075	0.0158

Table 8: Forward and Central Charge Asymmetries at LHC. Parameter sets (Set I, Set II and Unconstrained) for each model are given in Table 4.

In Figures 33 and 34 we show the top and anti-top rapidity distributions in LR models at the LHC for  $\sqrt{s} = 7 \text{ TeV}$  and  $\sqrt{s} = 14 \text{ TeV}$ , in Manifest LR model (left panel), Model A (middle panel) and Model B (right panel). Parameter sets (Set I, Set II and Unconstrained) for each model are distinguished (by blue, green and red curves). The SM distributions are given by black curves. These figures should be compared to Figure 30 from the Tevatron section. By comparison, the LHC asymmetries are even more dominated by events at, or near zero charge asymmetry for both top and anti-top quarks and do not show measurable deviations in LR models. Thus a significant charge asymmetry for top or anti-top quarks at the LHC would be indicative of BSM scenarios other than left-right models. It may be difficult to use the charge asymmetry to distinguish between various models, even those which

predict large asymmetries at the Tevatron, as a comprehensive analysis of their predictions at the LHC shows that they seem to be small, though some models may differ when evaluated at high invariant masses, which are especially sensitive to the  $q\bar{q}$  contribution [195].

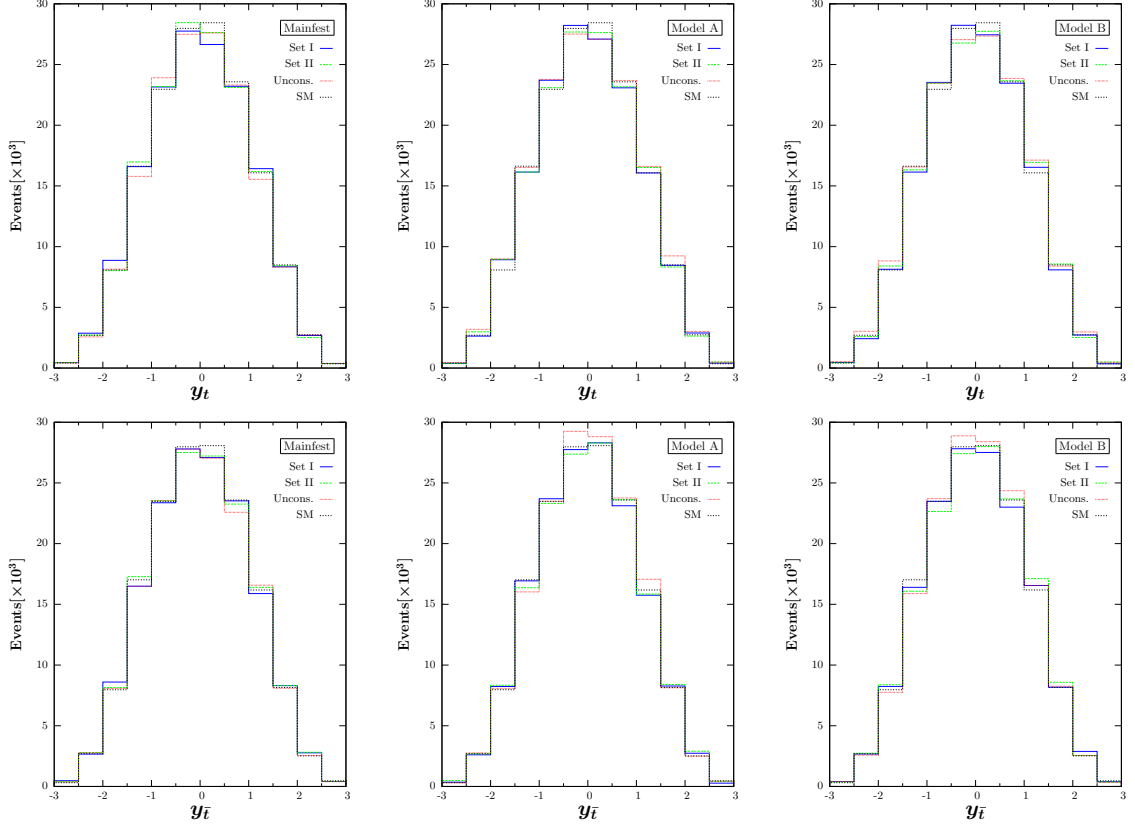


Figure 33: Top (upper row) and anti-top (lower row) rapidity distributions in Manifest LR model (left panel), Model A (middle panel) and Model B (right panel) at LHC ( $\sqrt{s} = 7$  TeV). The parameter sets (Set I, Set II and Unconstrained) for each model are given in Table 4.

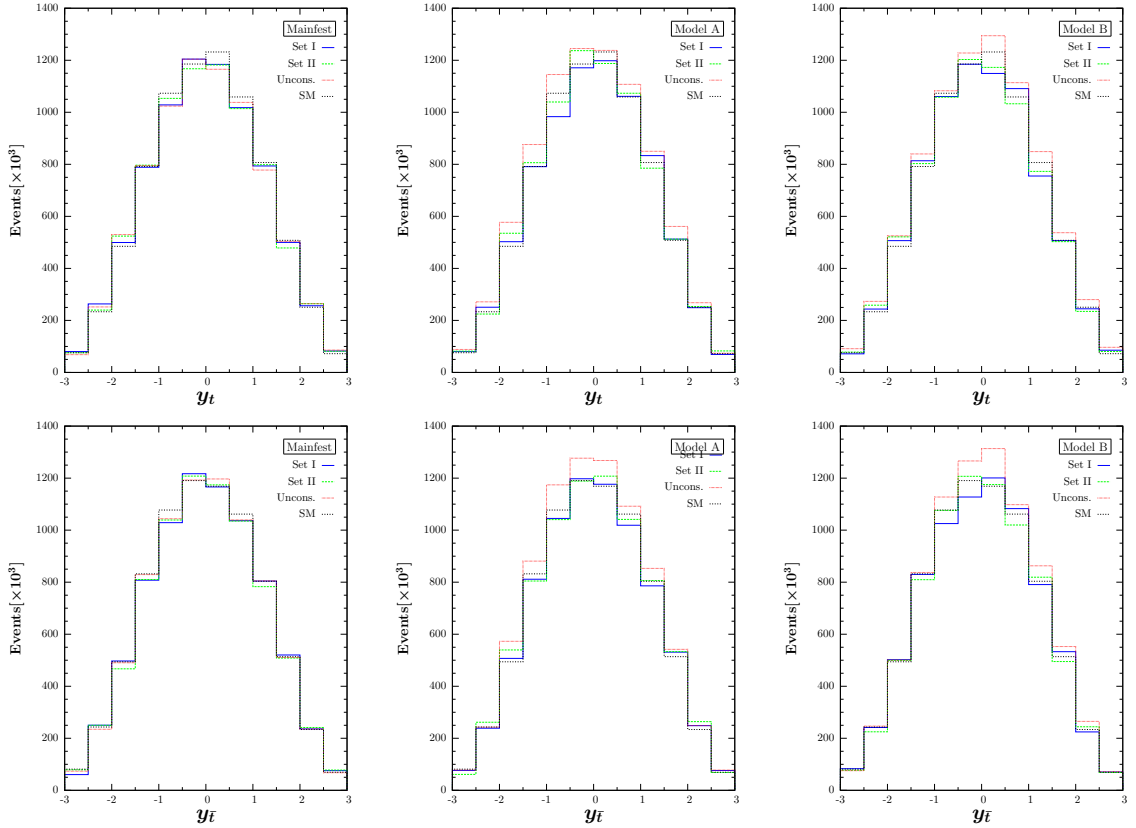


Figure 34: Top (upper row) and anti-top (lower row) rapidity distributions in Manifest LR model (left panel), Model A (middle panel) and Model B (right panel) at LHC ( $\sqrt{s} = 14$  TeV). The parameter sets (Set I, Set II and Unconstrained) for each model are given in Table 4.

### 5.3 Summary

The observation of a large forward-backward asymmetry in  $t\bar{t}$  production at the Tevatron offers tantalizing signals of BSM physics. For large rapidities and large invariant  $t\bar{t}$  mass distributions, the measurements deviate by  $3\sigma$  or more from the SM expectations. This seems to indicate that the phenomenology of the top quark, which has a mass of the order of electroweak symmetry breaking, may offer a window into new much anticipated BSM. Several models have been produced specifically to deal with the measurements. Though instructive, they seem like a band-aid solution. In addition, recent investigation of whether the increase in the asymmetry at large invariant mass  $M_{t\bar{t}}$  can be accounted for by a tree-level scalar exchange indicates that the range

of models who remain consistent with other top-related measurements, flavor violation constraints, electroweak precision measurements and collider data, is far more restricted than initially thought. There are at present other measurements which indicate deviations from the SM, which are not explained by most of the *ad-hoc* models that provide a fix for the forward- backward asymmetry.

One can then ask, what about the BSM scenarios favored on theoretical grounds, and already analyzed and subjected to relevant phenomenological and experimental tests. In this work, we analyzed the left-right model, in fact a general version of this model, where left and right coupling constants are not equal, and the quark mixing matrices in the left and right sectors are unrelated. The model is subjected to constraints coming from meson mixing ( $K^0 - \bar{K}^0$ ,  $B_d^0 - \bar{B}_d^0$  and  $B_s^0 - \bar{B}_s^0$ ) and  $b \rightarrow s\gamma$ . The production of  $W_R$  has been previously studied in this model and limits on the masses, coupling constants and right-handed quark mixing have been included. It is worthwhile to ask whether such a model can explain the deviation of the predicted asymmetry from the observed one at the Tevatron. The LR model has the features desired for a resolution: a  $W_R$  in the  $t$ -channel which can be responsible for the asymmetry, and a heavier  $Z_R$  in the  $s$ -channel, which may affect the observed cross section.

Our comprehensive analysis shows that, if the cross section agrees with the SM model one, as confirmed by the CDF data, the model is not able to generate sufficient asymmetry at the Tevatron to explain the observed discrepancy. We should add that this result survives variations in coupling constants, boson masses and right-handed CKM mass mixing parameters in the allowed parameter space determined by low-energy data. Relaxing these constraints would definitely yield bigger asymmetries and would provide large enough asymmetries to agree with the Tevatron data, as the Unconstrained version of LR models shows. This model is thus unlike models which explain the asymmetry through exchange of a light  $W'$  in the  $t$ -channel, coupling with a large coupling to only the  $t - d$  quark sector, and which requires additional fermions for anomaly cancellation.

We analyze the  $t\bar{t}$  cross section and asymmetries at the LHC. The cross section agrees with the one predicted by SM and measured at  $\sqrt{s} = 7$  TeV. One would expect to see the  $Z_R$  resonance for increased center of mass energy: so far, the indications are negative, pushing the  $Z'$  mass into the TeV range (although the precise values



depend on the model and parameters chosen). It is also likely that the LHC, looking for top jet resonances, would either validate or rule out at  $> 3\sigma$  level any extra  $Z'$  or  $W'$  models which can reproduce the Tevatron asymmetry. The left-right models predict a negligible charge asymmetry (the relevant defined parameter at the LHC), in either forward or central regions, at both  $\sqrt{s} = 7$  and 14 TeV. The predictions for the asymmetry are not even well-defined in sign, but the LR models are consistent with the SM predictions and so far, with the experimental results from ATLAS and CMS. The forward and central charge asymmetry have opposite signs. The arbitrariness in sign is unfortunate as it was shown that a definite positive (central-value) charge asymmetry at the LHC would strengthen the Tevatron results, while a definite negative (central-value) asymmetry would be unexpected and its explanation conflict with models that pass the Tevatron requirements [195]. One can draw two conclusions. One is that while the LR models predictions for the cross sections at the Tevatron and LHC *and* the asymmetry at LHC agree with the experimental data, these models cannot provide an explanation for the observed Tevatron forward-backward asymmetry. We can ascertain this with confidence, as it is valid for a large region of the parameter space and is valid independent of whether we chose Manifest, Model A or Model B. The questions still remain: are the Tevatron and LHC results inconsistent with each other (this will become clear with more precise LHC data), and what is the origin of the large forward-backward asymmetry. The second conclusion is that, while predictions for charge and forward-backward asymmetries are important in comparing models to experimental data, they are not good indicators of left-right models because they are very small. A more promising alternative would be to search for  $W_R$  bosons, predicted to be lighter than  $Z_R$ ; measuring top quark polarization which could indicate right-handed physics; and measuring left-right, rather than forward-backward, asymmetries. These tests are beyond the scope of this work and will be presented elsewhere.

There is however another issue that arises. Except for the *ad-hoc* models (some of which are already ruled out by a more careful analysis), it appears likely that none of the better-known BSM scenarios can produce such large asymmetries. Should negative asymmetries survive at LHC, consistency with Tevatron measurements would be challenging and demonstrate that top quark physics has subtleties not fully yet understood. Should asymmetries at the LHC be found to be small and positive, the

challenge would be in how to understand their enhancement in  $p\bar{p}$  but not  $pp$  (within normal expectations of symmetries in  $pp$  initial states). But before measurements, one must know what results to expect from established BSM scenarios. As many such scenarios are plagued by uncertainties due to a large parameter space, a clear result is important, as it would restrict BSM possibilities.

# Chapter 6

## CONCLUSION AND OUTLOOK

In this thesis we have studied the basics of left right symmetry in an asymmetric class of  $SU(2)_L \times SU(2)_R \times U(1)_{B-L}$  models. Focusing on the model with a particular choice of CKM matrix in the right-handed quark sector, we first investigated the allowed parameter space of the model by imposing well-known and accurately observed low energy phenomenology of B-meson mixing ( $B_d^0, B_s^0$ ) and  $b \rightarrow s\gamma$  transition. We followed an asymmetric parametrization of the RCKM quark mixing matrix where an arbitrary mixing between either second and third generations (scenario A with  $U_A$  mixing) or first and third generations (scenario B with  $U_B$  mixing) are allowed. Using various high-energy software packages for analytical and numerical evaluations, we set constraints on the RCKM matrix element ( $\sin \alpha$ ),  $W_R$  mass ( $M_{W_R}$ ), gauge couplings ratio ( $g_R/g_L$ ), electroweak scale VEVs ratio ( $\tan \beta$ ) and charged Higgs mass ( $M_{H^\pm}$ ). We found that these parameters are strongly correlated and while all parameters play an important role in the  $b \rightarrow s\gamma$  transition, the results for B-meson mixing are practically independent of  $\tan \beta$ . We concluded that with those stringent constraints on model parameters, ALRSM is very predictive. We presented our results in [8].

After that, we studied the production of  $W_R$  gauge boson and its consecutive decays at the LHC with the constraints on parameter space coming from low energy phenomenology. After investigating the single production cross section of  $W_R$  gauge boson ( $pp \rightarrow tW_R$ ) and branching ratios of decay channels ( $W_R \rightarrow 2X$ ) at the LHC, we analyzed the  $W_R$  production signal as a resonance in *dijet* mass distribution in both Tevatron ( $p\bar{p} \rightarrow t, W_R \rightarrow t, dijet$ ) and LHC ( $pp \rightarrow t, W_R \rightarrow t, dijet$ ). Top quark associated  $W_R$  production has a large background from top associated  $W_L$

production in SM, we showed that the  $W_R$  signal falls below the SM background in Tevatron which means that Tevatron is not a sufficiently powerful machine to discover such an extra gauge boson. However, we showed that at the LHC, the  $W_R$  resonance is always above the SM background which makes the model very predictive even in the early stages of the LHC. We published our results in [98].

Finally, we studied asymmetries in the top-anti-top pair production at both Tevatron and LHC in the context of ALRSM. The large discrepancy between SM prediction and experimental observation of forward-backward asymmetry in  $t\bar{t}$  production at the Tevatron offers signals of BSM physics. With this motivation, there are several models specifically built to deal with the experimental measurements. The main challenge in these models is to enhance the forward-backward asymmetry without disturbing the  $t\bar{t}$  production cross section which the SM prediction is already consistent with the experimental measurement. Thus we first investigated the effects of ALRSM to the forward-backward asymmetry in  $t\bar{t}$  production at the Tevatron, with an extra neutral gauge boson ( $Z_R$ ) in s-channel, contributing to the production cross section and not disturbing it by being relatively heavier, and with an extra charged gauge boson ( $W_R$ ) in t-channel which can be responsible for the asymmetry. We showed that, incorporating the low-energy constraints on model parameters and keeping the production cross section in agreement with the CDF observation, the ALRSM is not able to generate sufficiently large asymmetries at the Tevatron. Relaxing the constraints on model parameters, however, provides large enough asymmetries to agree with the Tevatron data but destroys the consistency in the cross section. We then carried out an analysis of the measurement of  $t\bar{t}$  production cross section and charge asymmetries at the LHC. We found that the cross section agrees with the one predicted by the SM and measured at  $\sqrt{s} = 7$  TeV and it is also consistent with the SM prediction at  $\sqrt{s} = 14$  TeV. We noticed that it would be possible to observe a  $Z_R$  resonance with increased center of mass energy at the later stages of LHC run. However, the charge asymmetries predicted by the model either in forward or central regions are negligibly small which actually are consistent with the SM predictions and earlier experimental results from ATLAS and CMS. We reported our results in [196].

More work remains to be done on  $W_R$  production and decays. If we introduce a model for neutrino decays of  $W_R$  to leptons (a possible signal, with less background, for  $W_R$ ), including supersymmetry, new decay modes might become available and the

whole production-decay signals would have to be re-analyzed. A comparison between  $W_R$  in the LRSM with  $W'$  in other models will pinpoint characteristics of signals and how to distinguish between models, thus offering a window into BSM gauge symmetries. All of these would have to be pursued in the light of data becoming available from LHC.

# Appendix A

## Notations and Conventions

This Appendix specifies the notations and conventions that are used through out the thesis. The four-vector position and momentum of a particle are

$$x^\mu = (t, \vec{x}) \quad , \quad p^\mu = (E, \vec{p}) \quad (\text{A-1})$$

and the four-vector derivative is

$$\partial_\mu = (\partial/\partial t, \vec{\nabla}) \quad (\text{A-2})$$

The spacetime metric is

$$\eta_{\mu\nu} = \begin{pmatrix} -1 & 0 & 0 & 0 \\ 0 & 1 & 0 & 0 \\ 0 & 0 & 1 & 0 \\ 0 & 0 & 0 & 1 \end{pmatrix} \quad (\text{A-3})$$

### A-1 Spinors and Dirac Algebra

Fermions can either be treated as two-component Weyl spinors or four-component Dirac or Majorana spinors. Since the Lagrangian of the Standard Model (and any supersymmetric extension of it) violates parity, each Dirac fermion has left- and right-handed parts with completely different electroweak interactions. If four-component Dirac notation is preferred then left- and right-handed projection operators must also be introduced

$$P_L = \frac{(1 - \gamma^5)}{2} \quad , \quad P_R = \frac{(1 + \gamma^5)}{2} \quad (\text{A-4})$$

The tools that are frequently used in Dirac algebra are  $4 \times 4$  gamma matrices which are constructed from  $2 \times 2$  sigma (Pauli spin) matrices in Weyl (or Chiral) basis

$$\gamma^\mu = \begin{pmatrix} 0 & \sigma^\mu \\ \bar{\sigma}^\mu & 0 \end{pmatrix}, \quad \gamma^5 = \begin{pmatrix} -1 & 0 \\ 0 & 1 \end{pmatrix} \quad (\text{A-5})$$

where

$$\sigma^\mu = (1, \boldsymbol{\sigma}) \quad , \quad \bar{\sigma}^\mu = (1, -\boldsymbol{\sigma}) \quad (\text{A-6})$$

$$\sigma^1 = \begin{pmatrix} 0 & 1 \\ 1 & 0 \end{pmatrix}, \quad \sigma^2 = \begin{pmatrix} 0 & -i \\ i & 0 \end{pmatrix}, \quad \sigma^3 = \begin{pmatrix} 1 & 0 \\ 0 & -1 \end{pmatrix} \quad (\text{A-7})$$

Some useful properties of gamma matrices

$$(\gamma^0)^\dagger = \gamma^0 \quad , \quad (\gamma^0)^2 = I \quad (\text{A-8})$$

$$(\gamma^k)^\dagger = -\gamma^k \quad , \quad (\gamma^k)^2 = -I \quad (\text{A-9})$$

$$(\gamma^5)^\dagger = \gamma^5 \quad , \quad (\gamma^5)^2 = I \quad (\text{A-10})$$

$$(\gamma^\mu)^\dagger = \gamma^0 \gamma^\mu \gamma^0 \quad (\text{A-11})$$

$$\{\gamma^5, \gamma^\mu\} = \gamma^5 \gamma^\mu + \gamma^\mu \gamma^5 = 0 \quad (\text{A-12})$$

these properties of gamma matrices also imply

$$(P_L)^2 = P_L \quad , \quad (P_R)^2 = P_R \quad , \quad P_L P_R = P_R P_L = 0 \quad (\text{A-13})$$

In Chiral representation, a four-component Dirac spinor is expressed in terms of 2 two-component, complex and anticommuting Weyl spinors  $\xi$  and  $\chi^\dagger$  with two distinct type of spinor indices  $\alpha = 1, 2$  and  $\dot{\alpha} = 1, 2$

$$\Psi_D = \begin{pmatrix} \xi_\alpha \\ \chi^{\dagger\dot{\alpha}} \end{pmatrix} \quad (\text{A-14})$$

and

$$\bar{\Psi}_D = \Psi_D^\dagger \gamma^0 = (\chi^\alpha \quad \xi_{\dot{\alpha}}^\dagger) \quad (\text{A-15})$$

where the field  $\xi$  is called a left-handed Weyl spinor and  $\chi^\dagger$  is a right-handed Weyl spinor because

$$P_L \Psi_D = \begin{pmatrix} \xi_\alpha \\ 0 \end{pmatrix}, \quad P_R \Psi_D = \begin{pmatrix} 0 \\ \chi^{\dagger\dot{\alpha}} \end{pmatrix} \quad (\text{A-16})$$

Some useful properties of Weyl spinors are

$$\boldsymbol{\xi}\boldsymbol{\chi} \equiv \xi^\alpha \chi_\alpha = \xi^\alpha \epsilon_{\alpha\beta} \chi^\beta = -\chi^\beta \epsilon_{\alpha\beta} \xi^\alpha = \chi^\beta \epsilon_{\beta\alpha} \xi^\alpha = \chi^\beta \xi_\beta \equiv \boldsymbol{\chi}\boldsymbol{\xi} \quad (\text{A-17})$$

$$\boldsymbol{\xi}^\dagger \boldsymbol{\chi}^\dagger \equiv \xi^{\dagger\dot{\alpha}} \chi_{\dot{\alpha}}^\dagger = \xi^{\dagger\dot{\alpha}} \epsilon_{\dot{\alpha}\dot{\beta}} \chi^{\dagger\dot{\beta}} = -\chi^{\dagger\dot{\beta}} \epsilon_{\dot{\alpha}\dot{\beta}} \xi^{\dagger\dot{\alpha}} = \chi^{\dagger\dot{\beta}} \epsilon_{\dot{\beta}\dot{\alpha}} \xi^{\dagger\dot{\alpha}} = \chi^{\dagger\dot{\beta}} \xi_{\dot{\beta}}^\dagger \equiv \boldsymbol{\chi}^\dagger \boldsymbol{\xi}^\dagger \quad (\text{A-18})$$

$$\begin{aligned} \boldsymbol{\xi}^\dagger \bar{\boldsymbol{\sigma}}^\mu \boldsymbol{\chi} &\equiv \xi_{\dot{\alpha}}^\dagger \bar{\sigma}^{\mu\dot{\alpha}\alpha} \chi_\alpha = \epsilon_{\dot{\alpha}\dot{\beta}} \xi^{\dagger\dot{\beta}} \bar{\sigma}^{\mu\dot{\alpha}\alpha} \epsilon_{\alpha\beta} \chi^\beta = -\chi^\beta \epsilon_{\alpha\beta} \epsilon_{\dot{\alpha}\dot{\beta}} \bar{\sigma}^{\mu\dot{\alpha}\alpha} \xi^{\dagger\dot{\beta}} \\ &= \frac{1}{2} \chi^\beta \sigma_{\alpha\dot{\alpha}}^\nu \sigma_{\nu\beta\dot{\beta}} \bar{\sigma}^{\mu\dot{\alpha}\alpha} \xi^{\dagger\dot{\beta}} = -\chi^\beta \sigma_{\alpha\dot{\alpha}}^\nu \delta_\nu^\mu \delta_\beta^\alpha \delta_{\dot{\beta}}^{\dot{\alpha}} \xi^{\dagger\dot{\beta}} = -\chi^\beta \sigma_{\beta\dot{\beta}}^\mu \xi^{\dagger\dot{\beta}} \\ &\equiv -\boldsymbol{\chi} \boldsymbol{\sigma}^\mu \boldsymbol{\xi}^\dagger \end{aligned} \quad (\text{A-19})$$

where the spinor indices are raised and lowered by using the antisymmetric tensor  $\epsilon^{\alpha\beta} = -\epsilon^{\beta\alpha} = \epsilon_{\beta\alpha} = -\epsilon_{\alpha\beta}$  and the reduction identities that are used in above equations are

$$\sigma_{\alpha\dot{\alpha}}^\mu \sigma_{\mu\beta\dot{\beta}} = -2 \epsilon_{\alpha\beta} \epsilon_{\dot{\alpha}\dot{\beta}} \quad (\text{A-20})$$

$$\sigma_{\nu\beta\dot{\beta}} \bar{\sigma}^{\mu\dot{\alpha}\alpha} = -2 \delta_\nu^\mu \delta_\beta^\alpha \delta_{\dot{\beta}}^{\dot{\alpha}} \quad (\text{A-21})$$

With all these properties and identities, it is possible to translate four-component Dirac language into two-component Weyl language (or vice versa) using the following dictionary

$$\bar{\Psi}_i P_L \Psi_j = \chi_i \xi_j \quad (\text{A-22})$$

$$\bar{\Psi}_i P_R \Psi_j = \xi_i^\dagger \chi_j^\dagger \quad (\text{A-23})$$

$$\bar{\Psi}_i \gamma^\mu P_L \Psi_j = \xi_i^\dagger \bar{\sigma}^\mu \xi_j \quad (\text{A-24})$$

$$\bar{\Psi}_i \gamma^\mu P_R \Psi_j = \chi_i \sigma^\mu \chi_j^\dagger \quad (\text{A-25})$$

where the spinor indices are suppressed and flavor or gauge indices  $(i, j)$  are introduced.

## A-2 Bidoublet-Triplet Conventions And Covariant Derivative

The nature of Left-Right symmetry leads us to use Higgs bidoublet and multiplets for fermionic mass generation and complete symmetry breaking. The conventions that



are used in this thesis are one Higgs bidoublet ( $\Phi$ ) and two Higgs triplets ( $\Delta_L, \Delta_R$ ). The covariant derivative of triplet fields can only be written in adjoint representation, thus for the sake of generalization all triplet fields are converted to their bidoublet equivalents allowing us to use only the fundamental representation for the covariant derivative for all fields.

- Triplet forms

$$\Delta = \begin{bmatrix} \Delta^1 \\ \Delta^2 \\ \Delta^3 \end{bmatrix} \implies D_\mu \Delta = (\partial_\mu - ig\epsilon^{ijk}W_\mu^j)\Delta^k \quad (\text{A-26})$$

where the covariant derivative is in adjoint representation.

- Bidoublet form

$$\Delta \rightarrow \frac{\sigma \cdot \Delta}{\sqrt{2}} = \begin{bmatrix} \frac{\Delta^+}{\sqrt{2}} & \Delta^{++} \\ \Delta^0 & -\frac{\Delta^+}{\sqrt{2}} \end{bmatrix} \quad (\text{A-27})$$

where the combinations of  $\Delta^1$  and  $\Delta^2$  form neutral  $\Delta^0$  and doubly charged  $\Delta^{++}$  fields while  $\Delta^3$  remains as singly charged  $\Delta^+$  field.

$$\frac{\Delta^1 + i\Delta^2}{\sqrt{2}} = \Delta^0, \quad \frac{\Delta^1 - i\Delta^2}{\sqrt{2}} = \Delta^{++}, \quad \Delta^3 = \Delta^+ \quad (\text{A-28})$$

and the covariant derivative in fundamental representation is

$$D_\mu \Delta = \partial_\mu \Delta - i\frac{g}{2}(\sigma \cdot W)\Delta + i\frac{g}{2}\Delta(\sigma \cdot W) \quad (\text{A-29})$$

The list of covariant derivatives of Higgs multiplets under  $SU(2)_L \times SU(2)_R \times U(1)_{B-L}$  symmetry

$$D_\mu \Phi = \partial_\mu \Phi - i\frac{g_L}{2}(\sigma \cdot W_{L\mu})\Phi + i\frac{g_R}{2}\Phi(\sigma \cdot W_{R\mu}) \quad (\text{A-30})$$

$$D_\mu \Delta_L = \partial_\mu \Delta_L - i\frac{g_L}{2}(\sigma \cdot W_{L\mu})\Delta_L + i\frac{g_L}{2}\Delta_L(\sigma \cdot W_{L\mu}) - ig_V \frac{B-L}{2}V_\mu \Delta_L \quad (\text{A-31})$$

$$D_\mu \Delta_R = \partial_\mu \Delta_R - i\frac{g_R}{2}(\sigma \cdot W_{R\mu})\Delta_R + i\frac{g_R}{2}\Delta_R(\sigma \cdot W_{R\mu}) - ig_V \frac{B-L}{2}V_\mu \Delta_R \quad (\text{A-32})$$

# Appendix B

## Feynman Rules in LRSM

Some basis and shorthand notations that are used in interaction vertices are;

- Vacuum expectation values:

$$v_i \equiv \{v_u, v_d, v_L, v_R\}$$

- Fermion masses:

$$D_i^\nu \equiv \{m_{\nu_e}, m_{\nu_\mu}, m_{\nu_\tau}\}$$

$$D_i^e \equiv \{m_e, m_\mu, m_\tau\}$$

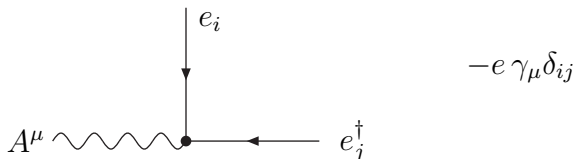
$$D_i^u \equiv \{m_u, m_c, m_t\}$$

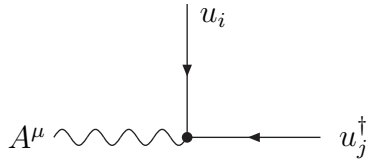
$$D_i^d \equiv \{m_d, m_s, m_b\}$$

- Higgs coefficient:

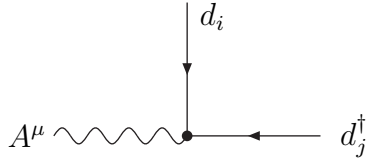
$$N_H = \left( v_u^2 + v_d^2 + \frac{(v_u^2 - v_d^2)^2}{2v_R^2} \right)^{-1/2}$$

### B-1 Fermion-Fermion-Gauge (FFV)

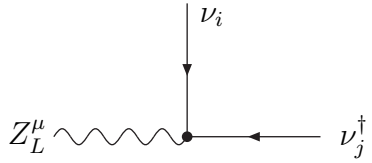




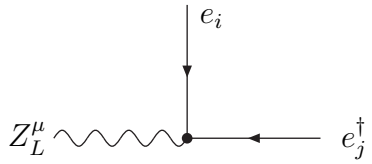
$$\frac{2e}{3} \gamma_\mu \delta_{ij}$$



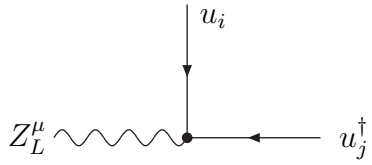
$$-\frac{e}{3} \gamma_\mu \delta_{ij}$$



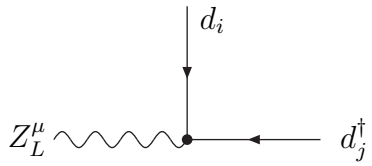
$$\frac{g_L}{\cos \theta_W} \frac{P_L}{2} \gamma_\mu \delta_{ij}$$



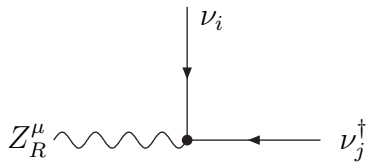
$$\frac{g_L}{\cos \theta_W} \left\{ -\frac{P_L}{2} + \sin^2 \theta_W \right\} \gamma_\mu \delta_{ij}$$



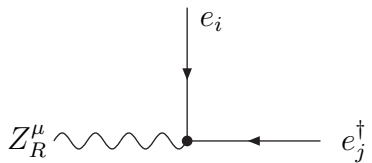
$$\frac{g_L}{\cos \theta_W} \left\{ \frac{P_L}{2} - \frac{2}{3} \sin^2 \theta_W \right\} \gamma_\mu \delta_{ij}$$



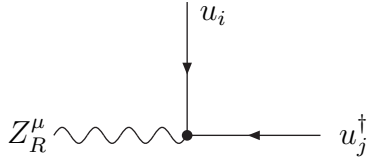
$$\frac{g_L}{\cos \theta_W} \left\{ -\frac{P_L}{2} + \frac{1}{3} \sin^2 \theta_W \right\} \gamma_\mu \delta_{ij}$$



$$\frac{g_Y}{\tan \varphi} \left\{ \frac{P_R}{2} + \frac{\tan^2 \varphi}{2} \right\} \gamma_\mu \delta_{ij}$$

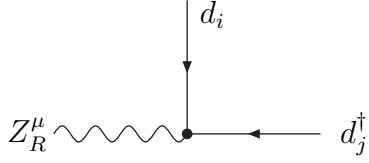


$$\frac{g_Y}{\tan \varphi} \left\{ -\frac{P_R}{2} + \frac{\tan^2 \varphi}{2} \right\} \gamma_\mu \delta_{ij}$$



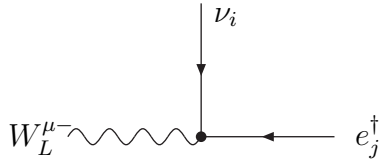
A Feynman diagram showing a vertex where a vertical line labeled  $u_i$  enters from the top, a horizontal line labeled  $u_j^\dagger$  enters from the right, and a wavy line labeled  $Z_R^\mu$  exits to the left.

$$\frac{g_Y}{\tan \varphi} \left\{ \frac{P_R}{2} - \frac{\tan^2 \varphi}{6} \right\} \gamma_\mu \delta_{ij}$$



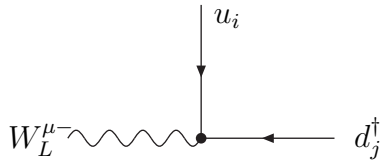
A Feynman diagram showing a vertex where a vertical line labeled  $d_i$  enters from the top, a horizontal line labeled  $d_j^\dagger$  enters from the right, and a wavy line labeled  $Z_R^\mu$  exits to the left.

$$\frac{g_Y}{\tan \varphi} \left\{ -\frac{P_R}{2} - \frac{\tan^2 \varphi}{6} \right\} \gamma_\mu \delta_{ij}$$



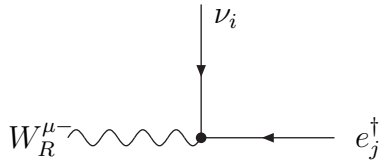
A Feynman diagram showing a vertex where a vertical line labeled  $\nu_i$  enters from the top, a horizontal line labeled  $e_j^\dagger$  enters from the right, and a wavy line labeled  $W_L^\mu$  exits to the left.

$$\frac{g_L}{\sqrt{2}} P_L \gamma_\mu U_{ij}^{L\dagger}$$



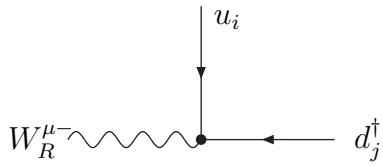
A Feynman diagram showing a vertex where a vertical line labeled  $u_i$  enters from the top, a horizontal line labeled  $d_j^\dagger$  enters from the right, and a wavy line labeled  $W_L^\mu$  exits to the left.

$$\frac{g_L}{\sqrt{2}} P_L \gamma_\mu V_{ij}^{L\dagger}$$



A Feynman diagram showing a vertex where a vertical line labeled  $\nu_i$  enters from the top, a horizontal line labeled  $e_j^\dagger$  enters from the right, and a wavy line labeled  $W_R^\mu$  exits to the left.

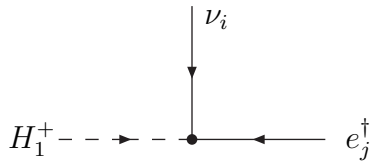
$$\frac{g_R}{\sqrt{2}} P_R \gamma_\mu U_{ij}^{R\dagger}$$



A Feynman diagram showing a vertex where a vertical line labeled  $u_i$  enters from the top, a horizontal line labeled  $d_j^\dagger$  enters from the right, and a wavy line labeled  $W_R^\mu$  exits to the left.

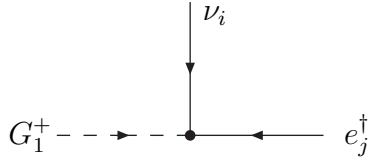
$$\frac{g_R}{\sqrt{2}} P_R \gamma_\mu V_{ij}^{R\dagger}$$

## B-2 Fermion-Fermion-Scalar (FFS)

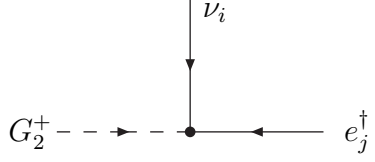


A Feynman diagram showing a vertex where a vertical line labeled  $\nu_i$  enters from the top, a horizontal line labeled  $e_j^\dagger$  enters from the right, and a dashed line labeled  $H_1^+$  enters from the left.

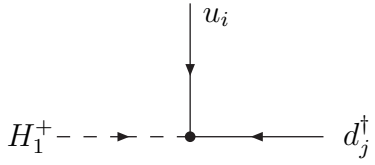
$$-i \frac{N_H}{\cos 2\beta} \left\{ \begin{aligned} & (\sin 2\beta D_i^\nu U_{ij}^L - U_{ij}^R D_j^e) P_L \\ & - (\sin 2\beta D_j^e U_{ij}^L - U_{ij}^R D_j^\nu) P_R \end{aligned} \right\}$$



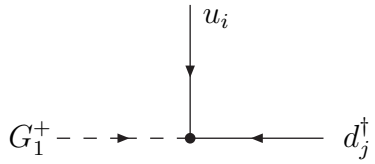
$$i \frac{g_L}{\sqrt{2}} \left\{ \frac{D_i^\nu}{m_{W_1}} U_{ij}^L P_L - \frac{D_j^e}{m_{W_1}} U_{ij}^R P_R \right\}$$



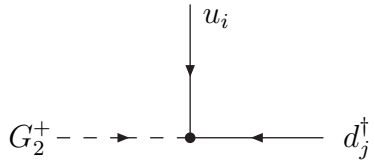
$$i \frac{g_R}{\sqrt{2}} \left\{ \frac{D_i^\nu}{m_{W_2}} U_{ij}^R P_R - \frac{D_j^e}{m_{W_2}} U_{ij}^L P_L \right\}$$



$$-i \frac{N_H}{\cos 2\beta} \left\{ (\sin 2\beta D_i^u V_{ij}^L - V_{ij}^R D_j^d) P_L - (\sin 2\beta D_j^d V_{ij}^L - V_{ij}^R D_j^u) P_R \right\}$$

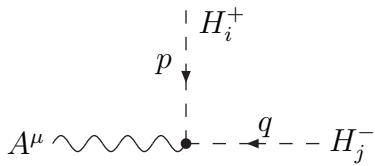


$$i \frac{g_L}{\sqrt{2}} \left\{ \frac{D_i^u}{m_{W_1}} V_{ij}^L P_L - \frac{D_j^d}{m_{W_1}} V_{ij}^R P_R \right\}$$

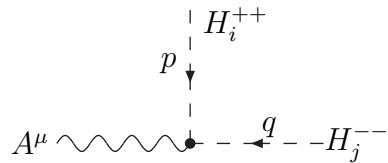


$$i \frac{g_R}{\sqrt{2}} \left\{ \frac{D_i^u}{m_{W_2}} V_{ij}^R P_R - \frac{D_j^d}{m_{W_2}} V_{ij}^L P_L \right\}$$

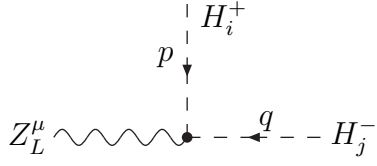
### B-3 Gauge-Scalar-Scalar (VSS)



$$ie \delta_{ij} (p - q)_\mu$$

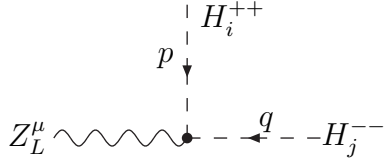


$$2ie \delta_{ij} (p - q)_\mu$$



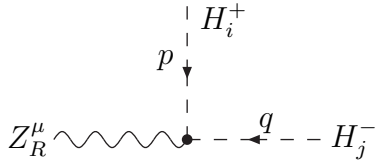
$$ie \frac{g_L^2 - g_Y^2}{2g_L g_Y} \left\{ \sum_{k=1}^2 (Z_C)_{ik} (Z_C)_{jk}^* \right\} (p - q)_\mu$$

$$- ie \frac{g_Y}{g_L} \left\{ \sum_{k=3}^4 (Z_C)_{ik} (Z_C)_{jk}^* \right\} (p - q)_\mu$$



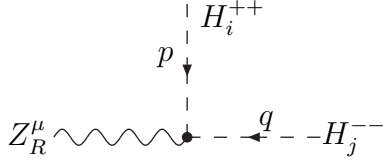
$$ie \frac{g_L^2 - g_Y^2}{g_L g_Y} \left\{ (Z_D)_{i1} (Z_D)_{j1}^* \right\} (p - q)_\mu$$

$$- 2ie \frac{g_Y}{g_L} \left\{ (Z_D)_{i2} (Z_D)_{j2}^* \right\} (p - q)_\mu$$



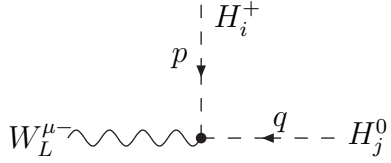
$$\frac{i\sqrt{g_R^2 - g_Y^2}}{2} \left\{ \sum_{k=1}^2 (Z_C)_{ik} (Z_C)_{jk}^* \right\} (p - q)_\mu$$

$$- \frac{i g_Y^2}{\sqrt{g_R^2 - g_Y^2}} \left\{ \sum_{k=3}^4 (Z_C)_{ik} (Z_C)_{jk}^* \right\} (p - q)_\mu$$



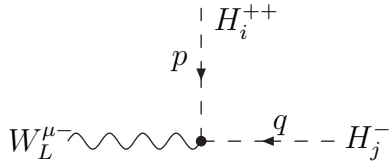
$$- \frac{i g_Y^2}{\sqrt{g_R^2 - g_Y^2}} \left\{ (Z_D)_{i1} (Z_D)_{j1}^* \right\} (p - q)_\mu$$

$$+ i \frac{g_R^2 - 2g_Y^2}{\sqrt{g_R^2 - g_Y^2}} \left\{ (Z_D)_{i2} (Z_D)_{j2}^* \right\} (p - q)_\mu$$

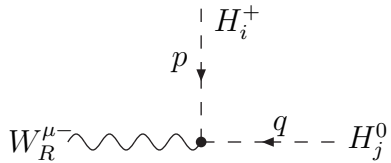


$$- \frac{i g_L}{\sqrt{2}} \left\{ \sum_{k,l=1}^2 \epsilon_{kl} (Z_C)_{ik} (Z_S)_{jl}^* \right\} (p - q)_\mu$$

$$+ i g_L \left\{ (Z_C)_{i3} (Z_S)_{j3}^* \right\} (p - q)_\mu$$



$$i g_L \left\{ (Z_D)_{i1} (Z_C)_{j3}^* \right\} (p - q)_\mu$$



$$- \frac{i g_R}{\sqrt{2}} \left\{ \sum_{k,l=1}^2 \epsilon_{kl} (Z_C)_{ik} (Z_S)_{jl}^* \right\} (p - q)_\mu$$

$$+ i g_R \left\{ (Z_C)_{i4} (Z_S)_{j4}^* \right\} (p - q)_\mu$$

A Feynman diagram showing a vertex where a wavy line labeled  $W_R^{\mu-}$  enters from the left, a dashed line labeled  $H_j^-$  enters from the right, and a dashed line labeled  $H_i^{++}$  exits upwards. A momentum vector  $p$  points downwards from the  $H_i^{++}$  line, and a momentum vector  $q$  points to the left from the  $H_j^-$  line.

$$i g_R \left\{ (Z_D)_{i2} (Z_C)_{j4}^* \right\} (p - q)_\mu$$

## B-4 Gauge-Gauge-Scalar (VVS)

A Feynman diagram showing a vertex where a wavy line labeled  $Z_L^\mu$  enters from the left, a dashed line labeled  $H_j^0$  enters from the right, and a wavy line labeled  $Z_L^\nu$  exits upwards.

$$\frac{g_L^2 + g_Y^2}{4} \left\{ \sum_{k=1}^2 (Z_S)_{jk}^* v_k + 8(Z_S)_{j3}^* v_3 \right\} g_{\mu\nu}$$

A Feynman diagram showing a vertex where a wavy line labeled  $Z_R^\mu$  enters from the left, a dashed line labeled  $H_j^0$  enters from the right, and a wavy line labeled  $Z_R^\nu$  exits upwards.

$$\frac{g_R^2 - g_Y^2}{4} \left\{ \sum_{k=1}^2 (Z_S)_{jk}^* v_k \right\} g_{\mu\nu} + \left\{ \frac{2g_Y^4}{g_R^2 - g_Y^2} (Z_S)_{j3}^* v_3 + \frac{2g_R^4}{g_R^2 - g_Y^2} (Z_S)_{j4}^* v_4 \right\} g_{\mu\nu}$$

A Feynman diagram showing a vertex where a wavy line labeled  $Z_L^\mu$  enters from the left, a dashed line labeled  $H_j^0$  enters from the right, and a wavy line labeled  $Z_R^\nu$  exits upwards.

$$-\frac{\sqrt{g_L^2 + g_Y^2} \sqrt{g_R^2 - g_Y^2}}{2} \left\{ \sum_{k=1}^2 (Z_S)_{jk}^* v_k \right\} g_{\mu\nu} + \left\{ \frac{4g_Y^2 \sqrt{g_L^2 + g_Y^2}}{\sqrt{g_R^2 - g_Y^2}} (Z_S)_{j3}^* v_3 \right\} g_{\mu\nu}$$

A Feynman diagram showing a vertex where a wavy line labeled  $A^\mu$  enters from the left, a dashed line labeled  $H_j^+$  enters from the right, and a wavy line labeled  $W_L^{\nu-}$  exits upwards.

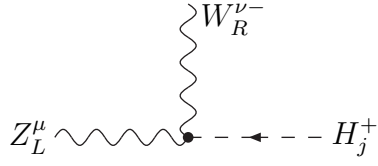
$$-\frac{e g_L}{\sqrt{2}} \left\{ \sum_{k,l=1}^2 \epsilon_{kl} (Z_C)_{jk}^* v_l - 2\sqrt{2} (Z_C)_{j3}^* v_3 \right\} g_{\mu\nu}$$

A Feynman diagram showing a vertex where a wavy line labeled  $A^\mu$  enters from the left, a dashed line labeled  $H_j^+$  enters from the right, and a wavy line labeled  $W_R^{\nu-}$  exits upwards.

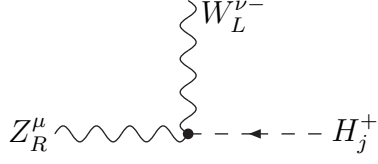
$$-\frac{e g_R}{\sqrt{2}} \left\{ \sum_{k=1}^2 (-1)^k (Z_C)_{jk}^* v_k - 2\sqrt{2} (Z_C)_{j4}^* v_4 \right\} g_{\mu\nu}$$

A Feynman diagram showing a vertex where a wavy line labeled  $Z_L^\mu$  enters from the left, a dashed line labeled  $H_j^+$  enters from the right, and a wavy line labeled  $W_L^{\nu-}$  exits upwards.

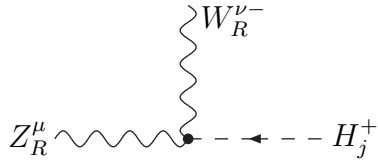
$$\frac{e g_Y}{\sqrt{2}} \left\{ \sum_{k,l=1}^2 \epsilon_{kl} (Z_C)_{jk}^* v_l - 2\sqrt{2} (Z_C)_{j3}^* v_3 \right\} g_{\mu\nu}$$



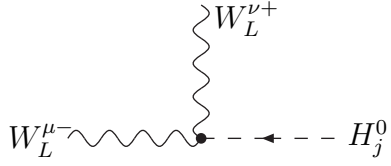
$$-\frac{eg_R}{\sqrt{2}} \left\{ \frac{g_L}{g_Y} \sum_{k=1}^2 (-1)^k (Z_C)_{jk}^* v_k + 2\sqrt{2} \frac{g_Y}{g_L} (Z_C)_{j4}^* v_4 \right\} g_{\mu\nu}$$



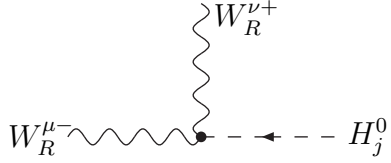
$$-\frac{g_L}{\sqrt{2}} \left\{ \sqrt{g_R^2 - g_Y^2} \sum_{k,l=1}^2 \epsilon_{kl} (Z_C)_{jk}^* v_l + \frac{2\sqrt{2}g_Y^2}{\sqrt{g_R^2 - g_Y^2}} (Z_C)_{j3}^* v_3 \right\} g_{\mu\nu}$$



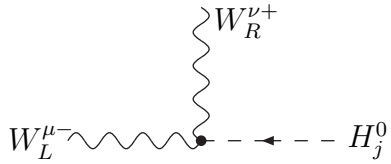
$$-\left\{ \frac{2g_R g_Y^2}{\sqrt{g_R^2 - g_Y^2}} (Z_C)_{j4}^* v_4 \right\} g_{\mu\nu}$$



$$g_L^2 \left\{ \sum_{k=1}^2 (Z_S)_{jk}^* v_k + 4(Z_S)_{j3}^* v_3 \right\} g_{\mu\nu}$$



$$g_R^2 \left\{ \sum_{k=1}^2 (Z_S)_{jk}^* v_k + 4(Z_S)_{j4}^* v_4 \right\} g_{\mu\nu}$$



$$-g_L g_R \left\{ \sum_{k,l=1}^2 (-1)^k \epsilon_{kl} (Z_S)_{jk}^* v_l \right\} g_{\mu\nu}$$



# Appendix C

## QCD Correction Factors for $B_{d,s}^0 - \bar{B}_{d,s}^0$ Mixing

We list here the coefficients used to calculate the NLO QCD corrections to  $B_{d,s}^0 - \bar{B}_{d,s}^0$  mixing in the left-right model, in eq. (3.21). The operators  $Q_4$  and  $Q_6$  mix under renormalization with an evolution matrix, and the respective Wilson coefficients are calculated in the following way,

$$\begin{pmatrix} C_4(m_b) \\ C_6(m_b) \end{pmatrix} = \begin{pmatrix} \eta_{LR}^{11} & \eta_{LR}^{12} \\ \eta_{LR}^{21} & \eta_{LR}^{22} \end{pmatrix} \begin{pmatrix} C_4(m_t) \\ C_6(m_t) \end{pmatrix} \quad (\text{C-1})$$

and the NLO QCD coefficients  $\eta_i(m_b)$  appear in Table 9.

	$\eta_1$	$\eta_2$	$\eta_3$	$\eta_5$	$\eta_{LR}^{11}$	$\eta_{LR}^{12}$	$\eta_{LR}^{21}$	$\eta_{LR}^{22}$
NLO	0.842	1.648	1.648	2.242	0.920	-0.039	-0.877	2.242

Table 9: The QCD correction parameters  $\eta_i(m_b)$  used in (3.21).

For a detailed analysis of QCD corrections we refer to [69].

# Appendix D

## 4-point Passarino-Veltman Integrals

The generic form of 4-point one-loop tensor integrals in 4d is

$$T^{\mu\nu\rho\sigma} = \frac{1}{i\pi^2} \int d^4k k^\mu k^\nu k^\rho k^\sigma \prod_{i=1}^4 \frac{1}{(k+r_i)^2 - m_i^2}, \quad (\text{D-1})$$

where we define the denominators with the conventions of Fig. 35. The internal

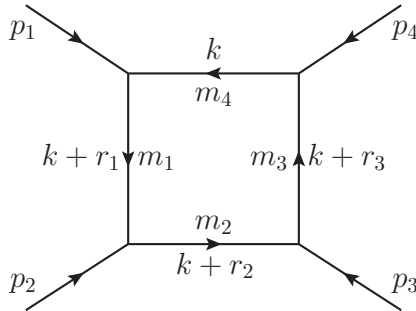


Figure 35: Momentum and mass conventions used in the Passarino-Veltman for evaluating the box diagrams.

momenta  $r_i$  are related to the external momenta through the relations,

$$\begin{aligned} r_i &= \sum_{j=1}^i p_j, \quad i = 1, 2, 3 \\ r_4 &= \sum_{j=1}^4 p_j = 0. \end{aligned} \quad (\text{D-2})$$

For  $B^0 - \bar{B}^0$  mixing we only needed the following scalar and tensor integrals

$$D_0 = \frac{1}{i\pi^2} \int d^4k \prod_{i=1}^4 \frac{1}{(k+r_i)^2 - m_i^2}, \quad (\text{D-3})$$

$$D^\mu = \frac{1}{i\pi^2} \int d^4k k^\mu \prod_{i=1}^4 \frac{1}{(k+r_i)^2 - m_i^2}, \quad (\text{D-4})$$

$$D^{\mu\nu} = \frac{1}{i\pi^2} \int d^4k k^\mu k^\nu \prod_{i=1}^4 \frac{1}{(k+r_i)^2 - m_i^2}, \quad (\text{D-5})$$

and the decomposition of tensor integrals in terms of reducible functions are;

$$D^\mu = \sum_{i=1}^3 r_i^\mu D_i, \quad (\text{D-6})$$

$$D^{\mu\nu} = g^{\mu\nu} D_{00} + \sum_{i,j=1}^3 r_i^\mu r_j^\nu D_{ij}. \quad (\text{D-7})$$

In `LoopTools`, these coefficient functions ( $D_0, D_i, D_{00}, D_{ij}$ ) are evaluated numerically, however at the vanishing external momenta limits these functions are not well defined. So at this point bypassing the `LoopTools`, we introduced the analytical expressions for those functions in the vanishing external momenta limit,

$$D(p_1^2, p_2^2, p_3^2, p_4^2, (p_1 + p_2)^2, (p_2 + p_3)^2, m_1^2, m_2^2, m_3^2, m_4^2), \quad (\text{D-8})$$

where  $p_i$ 's are external momenta and  $m_i$ 's are internal masses. Neglecting the external momenta, the structure of those functions might be represented as

$$D(0, 0, 0, 0, 0, 0, m_1^2, m_2^2, m_3^2, m_4^2), \quad (\text{D-9})$$

and we will call them for simplicity  $D(m_1^2, m_2^2, m_3^2, m_4^2)$ . Since we only consider the top quark contributions in the loop, those functions become  $D(m_i^2, m_j^2, m_i^2, m_i^2)$  in which  $m_i$  and  $m_j$  stand for the boson masses in the loop.

The relevant integrals for  $B^0 - \bar{B}^0$  mixing are the following:

$$D_0(m_i = m_j) = \frac{2(1-r) + (1+r) \ln r}{m_i^4 (r-1)^3}, \quad (\text{D-10})$$

$$D_0(m_i \neq m_j) = -\frac{s \ln s + [(s-r)(r-1) - (s-r^2) \ln r]}{m_i^4 (s-r)^2 (r-1)^2}, \quad (\text{D-11})$$

$$D_1(m_i = m_j) = -\frac{1 + (4-5r)r + 2(2+r)r \ln r}{4m_i^4 (r-1)^4}, \quad (\text{D-12})$$

$$\begin{aligned} D_1(m_i \neq m_j) &= \frac{(2r-1)s^2 - (2s-1)r^2}{2m_i^4 (s-1)(s-r)^3 (r-1)} \\ &+ \frac{(s-1)^2 [(r-2)s + r^2] r \ln r}{2m_i^4 (s-1)^2 (s-r)^3 (r-1)^2} \\ &- \frac{(r-1)^2 [(s-2)r + s^2] s \ln s}{2m_i^4 (s-1)^2 (s-r)^3 (r-1)^2}, \end{aligned} \quad (\text{D-13})$$

$$D_2(m_i = m_j) = -\frac{r^2 + 4r - 5 - 2(2r+1) \ln r}{4m_i^4 (r-1)^4}, \quad (\text{D-14})$$

$$\begin{aligned} D_2(m_i \neq m_j) &= -\frac{(r-3)s + r + r^2}{4m_i^4 (s-r)^2 (r-1)^2} \\ &+ \frac{s^2 (r-1)^3 \ln s}{2m_i^4 (s-1)(s-r)^3 (r-1)^3} \\ &- \frac{[s^2 + (r-3)sr^2 + r^3] \ln r}{2m_i^4 (s-r)^3 (r-1)^3}, \end{aligned} \quad (\text{D-15})$$

$$D_3(m_i = m_j) = -\frac{r^2 + 4r - 5 - 2(2r+1) \ln r}{4m_i^4 (r-1)^4}, \quad (\text{D-16})$$

$$\begin{aligned} D_3(m_i \neq m_j) &= -\frac{(r-3)s + r + r^2}{4m_i^4 (s-r)^2 (r-1)^2} \\ &+ \frac{s^2 (r-1)^3 \ln s}{2m_i^4 (s-1)(s-r)^3 (r-1)^3} \\ &- \frac{[s^2 + (r-3)sr^2 + r^3] \ln r}{2m_i^4 (s-r)^3 (r-1)^3}, \end{aligned} \quad (\text{D-17})$$

$$D_{00}(m_i = m_j) = -\frac{r^2 - 1 - 2r \ln r}{4m_i^2(r-1)^3}, \quad (\text{D-18})$$

$$D_{00}(m_i \neq m_j) = -\frac{(s-1)s^2 \ln s}{4m_i^2(s-r)^2(r-1)^2} - \frac{r\{(s-r)(r-1) + [(r-2)s+r] \ln r\}}{4m_i^2(s-r)^2(r-1)^2}, \quad (\text{D-19})$$

$$D_{11}(m_i = m_j) = \frac{-1+r[9-(17r-9)r] + 6(r+3)r^2 \ln r}{18m_i^4(r-1)^5}, \quad (\text{D-20})$$

$$D_{11}(m_i \neq m_j) = \frac{[r^2 + (2r-3)s]r^2 \ln r}{3m_i^4(s-r)^4(r-1)^2} - \frac{\{s^3 + 2(s-2)s^2r + [3+(s-3)s]r^2\}s \ln s}{3m_i^4(s-1)^3(s-r)^4} + \frac{-(s+1)s^2 + [5+(s-2)s]sr + [2+(5s-9)s]r^2}{6m_i^4(s-1)^2(s-r)^3(r-1)}, \quad (\text{D-21})$$

$$D_{12}(m_i = m_j) = \frac{(r-1)[1+(r+10)r] - 6(r+1)r \ln r}{12m_i^4(r-1)^5}, \quad (\text{D-22})$$

$$D_{12}(m_i \neq m_j) = \frac{2(s^2 - 3r + 2sr)s^2 \ln s}{12m_i^4(s-1)^2(s-r)^4} - \frac{r\{2(r-2)sr^2 + r^3 + [3+(r-3)r]s^2 \ln r\}}{6m_i^4(s-r)^4(r-1)^3} - \frac{-(r+1)r^2 + [5+(r-2)r]sr + [2+(5r-9)r]s^2}{12m_i^4(s-1)(s-r)^3(r-1)^2}, \quad (\text{D-23})$$

$$D_{13}(m_i = m_j) = \frac{(r-1)[1+(r+10)]r - 6(r+1)r \ln r}{12m_i^4(r-1)^5}, \quad (\text{D-24})$$

$$\begin{aligned}
D_{13}(m_i \neq m_j) &= \frac{2(s^2 - 3r + 2sr)s^2 \ln s}{12m_i^4(s-1)^2(s-r)^4} \\
&- \frac{r\{2(r-2)sr^2 + r^3 + [3 + (r-3)r]s^2 \ln r\}}{6m_i^4(s-r)^4(r-1)^3} \\
&- \frac{-(r+1)r^2 + [5 + (r-2)r]sr + [2 + (5r-9)r]s^2}{12m_i^4(s-1)(s-r)^3(r-1)^2}, \quad (D-25)
\end{aligned}$$

$$D_{22}(m_i = m_j) = \frac{17 - (r+1)9r + r^3 + 6(3r+1)\ln r}{18m_i^4(r-1)^5}, \quad (D-26)$$

$$\begin{aligned}
D_{22}(m_i \neq m_j) &= \frac{-s^3 \ln s}{3m_i^4(s-1)(s-r)^4} \\
&+ \frac{\{(r-4)sr^3 + [6 + (r-4)r]s^2r^2 - s^3 + r^4\} \ln r}{3m_i^4(s-r)^4(r-1)^4} \\
&+ \frac{11s^2 - 7(s+1)sr + 2[1 + (s-5)s]r^2}{18m_i^4(s-r)^3(r-1)^3} \\
&+ \frac{5(s+1)r^3 - r^4}{18m_i^4(s-r)^3(r-1)^3}, \quad (D-27)
\end{aligned}$$

$$D_{23}(m_i = m_j) = \frac{17 - (r+1)9r + r^3 + 6(3r+1)\ln r}{36m_i^4(r-1)^5}, \quad (D-28)$$

$$\begin{aligned}
D_{23}(m_i \neq m_j) &= \frac{-s^3 \ln s}{6m_i^4(s-1)(s-r)^4} \\
&+ \frac{\{(r-4)sr^3 + [6 + (r-4)r]s^2r^2 - s^3 + r^4\} \ln r}{6m_i^4(s-r)^4(r-1)^4} \\
&+ \frac{11s^2 - 7(s+1)sr + 2[1 + (s-5)s]r^2}{36m_i^4(s-r)^3(r-1)^3} \\
&+ \frac{5(s+1)r^3 - r^4}{36m_i^4(s-r)^3(r-1)^3}, \quad (D-29)
\end{aligned}$$

$$D_{33}(m_i = m_j) = \frac{17 - (r+1)9r + r^3 + 6(3r+1)\ln r}{18m_i^4(r-1)^5}, \quad (\text{D-30})$$

$$\begin{aligned} D_{33}(m_i \neq m_j) &= \frac{[(s-1)\ln r - (r-1)\ln s]s^3}{3m_i^4(s-1)(s-r)^4(r-1)} \\ &- \frac{\{(r-3)sr^2 + r^3 + [3 + (r-3)r]s^2r\}\ln r}{3m_i^4(s-r)^3(r-1)^4} \\ &+ \frac{11s^2 - 7(s+1)sr + 2[1 + (s-5)s]r^2}{18m_i^4(s-r)^3(r-1)^3} \\ &+ \frac{5(s+1)r^3 - r^4}{18m_i^4(s-r)^3(r-1)^3}, \end{aligned} \quad (\text{D-31})$$

where we define the parameters as

$$r = \left(\frac{m_t}{m_i}\right)^2 \quad \text{and} \quad s = \left(\frac{m_j}{m_i}\right)^2. \quad (\text{D-32})$$

# Bibliography

- [1] Becirevic, D. and Gimenez, V. and Martinelli, G. and Papinutto, M. and Reyes, J. B-Parameters Of The Complete Set Of Matrix Elements Of  $\Delta(B) = 2$  Operators From The Lattice. *JHEP*, **04**:025, 2002.
- [2] Senjanovic, G. and Mohapatra, R. N. Exact Left-Right Symmetry And Spontaneous Violation Of Parity. *Phys.Rev.*, **D12**(5):1502, 1975.
- [3] Pati, J. C. and Salam, A. Lepton Number As The Fourth Color. *Phys.Rev.*, **D10**(1):275, 1974.
- [4] Langacker, P. Bounds On Mixing Between Light And Heavy Gauge Bosons. *Phys.Rev.*, **D30**(9):2008, 1984.
- [5] Langacker, P. and Sankar, S. U. Bounds On The Mass Of  $W_R$  And The  $W_L - W_R$  Mixing Angle  $\zeta$  In General  $SU(2)_L \times SU(2)_R \times U(1)$  Models. *Phys.Rev.*, **D40**(5):1569, 1989.
- [6] Senjanovic, G. Spontaneous Breakdown Of Parity In A Class Of Gauge Theories. *Nucl.Phys.*, **B153**:334, 1978.
- [7] Harari, H. and Leurer, M. Left-Right Symmetry And The Mass Scale Of A Possible Right-Handed Weak Boson. *Nucl.Phys.*, **B233**:221, 1984.
- [8] Frank, M. and Hayreter, A. and Turan, I. B Decays In An Asymmetric Left-Right Model. *Phys.Rev.*, **D82**:033012, 2010.
- [9] Kiers, K. and Kolb, J. and Lee, J. and Soni, A. and Wu, G. H. Ubiquitous CP violation In A Top Inspired Left-Right Model. *Phys.Rev.*, **D66**:095002, 2002.



- [10] Barberio, E. and others (Heavy Flavor Averaging Group). Averages Of  $b$ -hadron And  $c$ -hadron Properties At The End Of 2007. *arXiv*, hep-ex/(0808.1297), 2008.
- [11] Abe, K. and others (Belle Collaboration). Measurements Of CP Violation Parameters In  $B^0 \rightarrow K_S \pi^0 \pi^0$  And  $B^0 \rightarrow K_S K_S$  Decays. *arXiv*, hep-ex/(0708.1845), 2007.
- [12] Abe, K. and others (Belle Collaboration). Measurements Of Time-Dependent CP Violation In  $B^0 \rightarrow \omega K_S^0$ ,  $f_0(980) K_S^0$ ,  $K_S^0 \pi^0$  And  $K^+ K^- K_S^0$  Decays. *Phys.Rev.*, **D76**:091103, 2007.
- [13] Adachi, I. and others (Belle Collaboration). Measurement Of The Differential Branching Fraction And Forward-Backward Asymmetry For  $B \rightarrow K^* l^+ l^-$ . *arXiv*, hep-ex/(0810.0335), 2008.
- [14] Lin, S.W. and others (Belle Collaboration). Difference In Direct Charge-Parity Violation Between Charged And Neutral B Meson Decays. *Nature*, **452**:332, 2008.
- [15] Adachi, I. and others (Belle Collaboration). Measurement Of  $B^- \rightarrow \tau^- \bar{\nu}_\tau$  Decay With A Semileptonic Tagging Method. *arXiv*, hep-ex/(0809.3834), 2008.
- [16] Widhalm, L. and others (Belle Collaboration). Measurement Of  $B(D_s^+ \rightarrow \mu^+ \nu_\mu)$ . *Phys.Rev.Lett.*, **100**:241801, 2008.
- [17] Amsler, C. and others (Particle Data Group). Review Of Particle Physics. *Phys.Lett.*, **B667**:1, 2008.
- [18] Abe, K. and others (Belle Collaboration). Observation Of Double  $c - \bar{c}$  Production In  $e^+ e^-$  Annihilation At  $\sqrt{s} \sim 10.6$ -GeV. *Phys.Rev.Lett.*, **89**:142001, 2002.
- [19] Aubert, B. and others (BABAR Collaboration). Measurement Of The  $B^\pm \rightarrow \rho^\pm \pi^0$  Branching Fraction And Direct CP Asymmetry. *Phys.Rev.*, **D75**:091103, 2007.
- [20] Bona, M. and others (UTfit Collaboration). First Evidence Of New Physics In  $b \longleftrightarrow s$  Transitions. *PMC Phys.*, **A3**:6, 2009.

- [21] Lenz, A. and Nierste, U. Theoretical Update Of  $B_s - \bar{B}_s$  Mixing. *JHEP*, **06**:072, 2007.
- [22] Abulencia, A. and others (CDF-Run II Collaboration). Measurement Of The  $B_s^0 - \bar{B}_s^0$  Oscillation Frequency. *Phys.Rev.Lett.*, **97**:062003, 2006.
- [23] Mohapatra, R. N. and Pati, J. C. Left-Right Gauge Symmetry And An Isoconjugate Model Of  $CP$  Violation. *Phys.Rev.*, **D11**(3):566, 1975.
- [24] Mohapatra, R. N. and Pati, J. C. A Natural Left-Right Symmetry. *Phys.Rev.*, **D11**(9):2558, 1975.
- [25] Mohapatra, R. N. and Paige, Frank E. and Sidhu, D. P. Symmetry Breaking And Naturalness Of Parity Conservation In Weak Neutral Currents In Left-Right Symmetric Gauge Theories. *Phys.Rev.*, **D17**(9):2462, 1978.
- [26] Beg, M. A. B. and Budny, R. V. and Mohapatra, R. N. and Sirlin, A. Manifest Left-Right Symmetry And Its Experimental Consequences. *Phys.Rev.Lett.*, **38**(22):1252, 1977.
- [27] Mohapatra, R. N. and Senjanovic, G. Neutrino Mass And Spontaneous Parity Nonconservation. *Phys.Rev.Lett.*, **44**:912, 1980.
- [28] Gunion, J. F. and Grifols, J. and Mendez, A. and Kayser, B. and Olness, F. Higgs Bosons In Left-Right Symmetric Models. *Phys.Rev.*, **D40**(5):1546, 1989.
- [29] Grifols, J. A. Higgs Bosons In A Left-Right Symmetric Gauge Model. *Phys.Rev.*, **D18**(7):2704, 1978.
- [30] Grifols, J. A. and Mendez, A. and Schuler, G.A. Production And Decay Of Doubly Charged Higgs Bosons Of Left-Right Symmetric Models. *Mod.Phys.Lett.*, **A4**(15):1485, 1989.
- [31] Deshpande, N. G. and Gunion, J. F. and Kayser, B. and Olness, F. Left-Right Symmetric Electroweak Models With Triplet Higgs Field. *Phys.Rev.*, **D44**(3):837, 1991.
- [32] Swartz, M. L. Limits On Doubly Charged Higgs Bosons And Lepton Flavor Violation. *Phys.Rev.*, **D40**(5):1521, 1989.

- [33] Vega, R. and Dicus, D.A. Doubly Charged Higgs And  $W^+W^+$  Production. *Nucl.Phys.*, **B329**(3):533, 1990.
- [34] Huitu, K. and Maalampi, J. and Pietila, A. and Raidal, M. Doubly Charged Higgs At LHC. *Nucl.Phys.*, **B487**:27, 1997.
- [35] Datta, A. and Raychaudhuri, A. Mass Bounds For Triplet Scalars Of The Left-Right Symmetric Model And Their Future Detection Prospects. *Phys.Rev.*, **D62**:055002, 2000.
- [36] Barenboim, G. and Gorbahn, M. and Nierste, U. and Raidal, M. Higgs Sector Of The Minimal Left-Right Symmetric Model. *Phys.Rev.*, **D65**:095003, 2002.
- [37] Kiers, K. and Assis, M. and Petrov, A. A. Higgs Sector Of The Left-Right Model With Explicit CP Violation. *Phys.Rev.*, **D71**:115015, 2005.
- [38] Akeroyd, A. G. and Aoki, M. Single And Pair Production Of Doubly Charged Higgs Bosons At Hadron Colliders. *Phys.Rev.*, **D72**:035011, 2005.
- [39] Gielen, S. CP Violation Makes Left-Right Symmetric Extensions With Non-Hermitian Mass Matrices Appear Unnatural. *Phys.Rev.*, **D81**:076003, 2010.
- [40] Rizzo, T. G. Constraints From  $b \rightarrow s\gamma$  On The Left-Right Symmetric Model. *Phys.Rev.*, **D50**:3303, 1994.
- [41] Cho, P. L. and Misiak, M.  $b \rightarrow s\gamma$  Decay In  $SU(2)_L \times SU(2)_R \times U(1)$  Extensions Of The Standard Model. *Phys.Rev.*, **D49**:5894, 1994.
- [42] Babu, K. S. and Fujikawa, K. and Yamada, A. Constraints On Left-Right Symmetric Models From The Process  $b \rightarrow s\gamma$ . *Phys.Lett.*, **B333**:196, 1994.
- [43] Bhattacharyya, G. and Raychaudhuri, A. Constraining The Charged Higgs Mass In The Left-Right Symmetric Model From  $b \rightarrow s\gamma$ . *Phys.Lett.*, **B357**:119, 1995.
- [44] Kim, C. S. and Kim, Y. G.  $b \rightarrow s\gamma$  Decays In The Left-Right Symmetric Model. *Phys.Rev.*, **D61**:054008, 2000.
- [45] Hou, W. S. and Soni, A. Gauge Invariance Of The  $K_L - K_S$  Mass Difference In Left-Right Symmetric Models. *Phys.Rev.*, **D32**(1):163, 1985.

- [46] L. Maharana. Left-Right Symmetry,  $K_L - K_S$  Mass Difference And Mass Of  $W_R$  Boson In A Field Theoretic Quark Model. *Phys.Lett.*, **B149**(4-5):399, 1984.
- [47] Frère, J. M. and Galand, J. and Le Yaouanc, A. and Oliver, L. and Pène, O. and Raynal, J. C.  $K^0 - \bar{K}^0$  In The  $SU(2)_L \times SU(2)_R \times U(1)$  Model Of  $CP$  Violation. *Phys.Rev.*, **D46**(1):337, 1992.
- [48] Chang, D. and Basecq, J. and Li, L.F. and Pal, P. B. Comment On The  $K_L - K_S$  Mass Difference In The Left-Right Model. *Phys.Rev.*, **D30**(7):1601, 1984.
- [49] Beall, G. and Bander, M. and Soni, A. Constraint On The Mass Scale Of A Left-Right Symmetric Electroweak Theory From The  $K_L - K_S$  Mass Difference. *Phys.Rev.Lett.*, **48**(13):848, 1982.
- [50] Mohapatra, R. N. and Senjanovic, G. and Tran, M. D. Strangeness-Changing Processes And The Limit On The Right-Handed Gauge Boson Mass. *Phys.Rev.*, **D28**(3):546, 1983.
- [51] Colangelo, P. and Nardulli, G. Improved Bound On  $W_R$  Mass In Left-Right Symmetric Models From  $K^0 - \bar{K}^0$  Mixing. *Phys.Lett.*, **B253**(1-2):154, 1991.
- [52] Pospelov, M. E. FCNC In Left-Right Symmetric Theories And Constraints On The Right-Handed Scale. *Phys.Rev.*, **D56**:259, 1997.
- [53] Aubert, B. and others (BABAR Collaboration). Measurements Of The  $B \rightarrow X_s \gamma$  Branching Fraction And Photon Spectrum From A Sum Of Exclusive Final States. *Phys.Rev.*, **D72**(5):052004, 2005.
- [54] Koppenburg, P. and others (Belle Collaboration). Inclusive Measurement Of The Photon Energy Spectrum In  $b \rightarrow s \gamma$  Decays. *Phys.Rev.Lett.*, **93**(6):061803, 2004.
- [55] Misiak, M. and Asatrian, H. M. and Bieri, K. and Czakon, M. and Czarnecki, A. and Ewerth, T. and Ferroglia, A. and Gambino, P. and Gorbahn, M. and Greub, C. and Haisch, U. and Hovhannisyan, A. and Hurth, T. and Mitov, A. and Poghosyan, V. and Ślusarczyk, M. and Steinhauser, M. Estimate Of  $B(\bar{B} \rightarrow X_s \gamma)$  At  $O(\alpha_s^2)$ . *Phys.Rev.Lett.*, **98**(2):022002, 2007.

- [56] Hahn, T. Generating Feynman Diagrams And Amplitudes With FeynArts 3. *Comput.Phys.Commun.*, **140**:418, 2001.
- [57] Hahn, T. and Schappacher, C. The Implementation Of The Minimal Supersymmetric Standard Model In FeynArts And FormCalc. *Comput.Phys.Commun.*, **143**:54, 2002.
- [58] Hahn, T. and Perez-Victoria, M. Automatized One Loop Calculations In Four-Dimensions And D-Dimensions. *Comput.Phys.Commun.*, **118**:153, 1999.
- [59] Hahn, T. Automatic Loop Calculations With FeynArts, FormCalc, And Loop-Tools. *Nucl.Phys.Proc.Suppl.*, **89**:231, 2000.
- [60] Bertolini, S. and Borzumati, F. and Masiero, A. QCD Enhancement Of Radiative B Decays. *Phys.Rev.Lett.*, **59**(2):180, 1987.
- [61] Mohapatra, D. and others (Belle Collaboration). Observation Of  $b \rightarrow d\gamma$  And Determination Of  $|V_{td}/V_{ts}|$ . *Phys.Rev.Lett.*, **96**(22):221601, 2006.
- [62] Aubert, B. and others (BABAR Collaboration). Study Of Time-Dependent CP-Violating Asymmetries And Flavor Oscillations In Neutral B Decays At The  $\Upsilon(4S)$ . *Phys.Rev.*, **D66**(3):032003, 2002.
- [63] Aubert, B. and others (BABAR Collaboration). Measurements Of Branching Fractions For  $B^+ \rightarrow \rho^+\gamma$ ,  $B^0 \rightarrow \rho^0\gamma$ , And  $B^0 \rightarrow \omega\gamma$ . *Phys.Rev.*, **D78**(11):112001, 2008.
- [64] Altarelli, G. and Franzini, P. J.  $B^0 - \bar{B}^0$  Mixing Within And Beyond The Standard Model. *Z.Phys.*, **C37**:271, 1988.
- [65] Ecker, G. and Grimus, W. Mass Mixing, CP Violation And Left-Right Symmetry For Heavy Neutral Mesons. *Z.Phys.*, **C30**:293, 1986.
- [66] Ecker, G. and Grimus, W. and Neufeld, H. Higgs Induced Flavour Changing Neutral Interactions In  $SU(2)_L \times SU(2)_R \times U(1)$ . *Phys.Lett.*, **B127**:365, 1983.
- [67] Gilman, F. J. and Reno, M. H. Restrictions From The Neutral  $K$  And  $B$  Meson Systems On Left-Right Symmetric Gauge Theories. *Phys.Rev.*, **D29**(5):937, 1984.

- [68] Maharana, L. and Nath, A. and Panda, A. R.  $K_L - K_S$ ,  $B_d^0 - \bar{B}_d^0$  Mass Differences And Top Quark And  $W_R$  Boson Masses In The Left-Right Symmetric Model. *Phys.Rev.*, **D47**(11):4998, 1993.
- [69] Buras, A. J. and Jager, S. and Urban, J. Master Formulae For  $\Delta(F) = 2$  NLO-QCD Factors In The Standard Model And Beyond. *Nucl.Phys.*, **B605**:600, 2001.
- [70] Abulencia, A. and others (CDF Collaboration). Observation Of  $B_s^0 - \bar{B}_s^0$  Oscillations. *Phys.Rev.Lett.*, **97**:242003, 2006.
- [71] Abazov, V. M. and others (DØ Collaboration). First Direct Two-Sided Bound On The  $B_s^0$  Oscillation Frequency. *Phys.Rev.Lett.*, **97**:021802, 2006.
- [72] Buras, A. J. and Jamin, M. and Weisz, P. H. Leading And Next-To-Leading QCD Corrections To  $\epsilon$  Parameter And  $B^0 - \bar{B}^0$  Mixing In The Presence Of A Heavy Top Quark. *Nucl.Phys.*, **B347**:491, 1990.
- [73] Mahmoudi, F. and Stal, O. Flavor Constraints On The Two-Higgs-Doublet Model With General Yukawa Couplings. *Phys.Rev.*, **D81**:035016, 2010.
- [74] Fukuda, Y. and others (Super-Kamiokande Collaboration). Evidence For Oscillation Of Atmospheric Neutrinos. *Phys.Rev.Lett.*, **81**:1562, 1998.
- [75] Abazov, V. M. and others (DØ Collaboration). Search For Doubly Charged Higgs Boson Pair Production In The Decay to  $\mu^+\mu^+\mu^-\mu^-$  in  $p\bar{p}$  Collisions At  $\sqrt{s} = 1.96$  TeV. *Phys.Rev.Lett.*, **93**(14):141801, 2004.
- [76] Acosta, D. and others (CDF Collaboration). Search For Doubly Charged Higgs Bosons Decaying To Dileptons In  $p\bar{p}$  Collisions At  $\sqrt{s} = 1.96$  TeV. *Phys.Rev.Lett.*, **93**(22):221802, 2004.
- [77] Acosta, D. and others (CDF Collaboration). Search For Long-Lived Doubly Charged Higgs Bosons In  $p\bar{p}$  Collisions At  $\sqrt{s} = 1.96$  TeV. *Phys.Rev.Lett.*, **95**(7):071801, 2005.
- [78] Agashe, K. and Delgado, A. and May, M. J. and Sundrum, R. RS1, Custodial Isospin And Precision Tests. *JHEP*, **08**:050, 2003.

- [79] Agashe, K. and Davoudiasl, H. and Gopalakrishna, S. and Han, T. and Huang, G.Y. and Perez, G. and Si, Z.G. and Soni, A. LHC Signals For Warped Electroweak Neutral Gauge Bosons. *Phys.Rev.*, **D76**:115015, 2007.
- [80] Agashe, K. and Gopalakrishna, S. and Han, T. and Huang, G. Y. and Soni, A. LHC Signals For Warped Electroweak Charged Gauge Bosons. *Phys.Rev.*, **D80**:075007, 2009.
- [81] Appelquist, T. and Cheng, H. C. and Dobrescu, B. A. Bounds On Universal Extra Dimensions. *Phys.Rev.*, **D64**:035002, 2001.
- [82] Cheng, H. C. and Matchev, K. T. and Schmaltz, M. Bosonic Supersymmetry? Getting Fooled At The CERN LHC. *Phys.Rev.*, **D66**:056006, 2002.
- [83] Arkani-Hamed, N. and Cohen, A. G. and Katz, E. and Nelson, A. E. The Littlest Higgs. *JHEP*, **07**:034, 2002.
- [84] Kaplan, D. E. and Schmaltz, M. The Little Higgs From A Simple Group. *JHEP*, **10**:039, 2003.
- [85] Han, T. and Logan, H. E. and McElrath, B. and Wang, L. T. Phenomenology Of The Little Higgs Model. *Phys.Rev.*, **D67**:095004, 2003.
- [86] Csaki, C. and Grojean, C. and Pilo, L. and Terning, J. Towards A Realistic Model Of Higgsless Electroweak Symmetry Breaking. *Phys.Rev.Lett.*, **92**:101802, 2004.
- [87] Chivukula, R. S. and Coleppa, B. and Chiara, S. D. and Simmons, E. H. and He, H.J. and Kurachi, M. and Tanabashi, M. A Three Site Higgsless Model. *Phys.Rev.*, **D74**:075011, 2006.
- [88] He, H.J. and Kuang, Y.P. and Qi, Y.H. and Zhang, B. and Belyaev, A. and Chivukula, R. S. and Christensen, N. D. and Pukhov, A. and Simmons, E. H. LHC Signatures Of New Gauge Bosons In Minimal Higgsless Model. *Phys.Rev.*, **D78**:031701, 2008.
- [89] Rizzo, T. G. Model Dependence Of  $W_R$  Searches At The Tevatron. *Phys.Rev.*, **D50**:325, 1994.

- [90] Gopalakrishna, S. and Han, T. and Lewis, I. and Si, Z. G. and Zhou, Y. F. Chiral Couplings Of  $W'$  And Top Quark Polarization At The LHC. *Phys.Rev.*, **D82**:115020, 2010.
- [91] Rizzo, T. G. The Determination Of The Helicity Of  $W'$  Boson Couplings At The LHC. *JHEP*, **05**:037, 2007.
- [92] Tait, T. M. P. and Yuan, C. P. Single Top Quark Production As A Window To Physics Beyond The Standard Model. *Phys.Rev.*, **D63**:014018, 2000.
- [93] Cao, Q. H. and Wudka, J. and Yuan, C. P. Search For New Physics Via Single Top Production At The LHC. *Phys.Lett.*, **B658**:50, 2007.
- [94] Abazov, V. M. and others (DØ Collaboration). Search For  $W'$  Bosons Decaying To An Electron And A Neutrino With The D0 Detector. *Phys.Rev.Lett.*, **100**:031804, 2008.
- [95] Abazov, V. M. and others (DØ Collaboration). Search For  $W'$  Boson Resonances Decaying To A Top Quark And A Bottom Quark. *Phys.Rev.Lett.*, **100**:211803, 2008.
- [96] Aaltonen, T. and others (CDF Collaboration). Search For New Particles Decaying Into Dijets In Proton-Antiproton Collisions At  $\sqrt{s} = 1.96 \text{ TeV}$ . *Phys.Rev.*, **D79**(11):112002, 2009.
- [97] Pukhov, A. Calchep 2.3: MSSM, Structure Functions, Event Generation, And Generation Of Matrix Elements For Other Packages. *arXiv*, hep-ph/(0412191), 2004.
- [98] Frank, M. and Hayreter, A. and Turan, I. Production And Decays Of  $W_R$  Bosons At The LHC. *Phys.Rev.*, **D83**:035001, 2011.
- [99] CDF Collaboration. Combination Of Top Quark Pair Production Cross Section Results. [http://www-cdf.fnal.gov/physics/new/top/2009/xsection/ttbar-combined\\_46invfb/](http://www-cdf.fnal.gov/physics/new/top/2009/xsection/ttbar-combined_46invfb/), 2009.
- [100] Aaltonen, T. and others (CDF Collaboration). First Measurement Of The  $t\bar{t}$  Differential Cross Section  $d\sigma/dM(t\bar{t})$  In  $p\bar{p}$  Collisions At  $\sqrt{s}=1.96\text{-TeV}$ . *Phys.Rev.Lett.*, **102**:222003, 2009.



- [101] Aaltonen, T. and others (CDF Collaboration). Limits On The production Of Narrow  $t\bar{t}$  Resonances In  $p\bar{p}$  Collisions At  $\sqrt{s}=1.96$ -TeV. *Phys.Rev.*, **D77**:051102, 2008.
- [102] Abazov, V.M. and others (DØ Collaboration). Combination Of  $t\bar{t}$  Cross Section Measurements And Constraints On The Mass Of The Top Quark And Its Decays Into Charged Higgs Bosons. *Phys.Rev.*, **D80**:071102, 2009.
- [103] Abazov, V.M. and others (DØ Collaboration). Search For  $t\bar{t}$  Resonances In The Lepton Plus Jets Final State In  $p\bar{p}$  Collisions At  $\sqrt{s}=1.96$ -TeV. *Phys.Lett.*, **B668**:98–104, 2008.
- [104] Aaltonen, T. and others (CDF Collaboration). Forward-Backward Asymmetry In Top Quark Production In  $p\bar{p}$  Collisions At  $\sqrt{s} = 1.96$  TeV. *Phys.Rev.Lett.*, **101**:202001, 2008.
- [105] Aaltonen, T. and others (CDF Collaboration). Evidence For A Mass Dependent Forward-Backward Asymmetry In Top Quark Pair Production. *Phys.Rev.*, **D83**:112003, 2011.
- [106] Aaltonen, T. and others (CDF Collaboration). Invariant Mass Distribution Of Jet Pairs Produced In Association With A  $W$  Boson In  $p\bar{p}$  Collisions At  $\sqrt{s} = 1.96$  TeV. *Phys.Rev.Lett.*, **106**:171801, 2011.
- [107] Abazov, V.M. and others (DØ Collaboration). First measurement Of The Forward-Backward Charge Asymmetry In Top Quark Pair Production. *Phys.Rev.Lett.*, **100**:142002, 2008.
- [108] Almeida, L.G. and Sterman, G.F. and Vogelsang, W. Threshold Resummation For The Top Quark Charge Asymmetry. *Phys.Rev.*, **D78**:014008, 2008.
- [109] Antunano, O. and Kuhn, J. H. and Rodrigo, G. Top Quarks, Axigluons And Charge Asymmetries At Hadron Colliders. *Phys.Rev.*, **D77**:014003, 2008.
- [110] Bowen, M.T. and Ellis, S.D. and Rainwater, D. Standard Model Top Quark Asymmetry At The Fermilab Tevatron. *Phys.Rev.*, **D73**:014008, 2006.
- [111] Kuhn, J.H. and Rodrigo, G. Charge Asymmetry Of Heavy Quarks At Hadron Colliders. *Phys.Rev.*, **D59**:054017, 1999.

- [112] Kuhn, J.H. and Rodrigo, G. Charge Asymmetry In Hadroproduction Of Heavy Quarks. *Phys.Rev.Lett.*, **81**:49–52, 1998.
- [113] Ahrens, V. and Ferroglia, A. and Neubert, M. and Pecjak, B.D. and Yang, L.L. The Top-Pair Forward-Backward Asymmetry Beyond NLO. *arXiv*, hep-ph/(1106.6051), 2011.
- [114] Hollik, W. and Pagani, D. The Electroweak Contribution To The Top Quark Forward-Backward Asymmetry At The Tevatron. *arXiv*, hep-ph/(1107.2606), 2011.
- [115] Jung, S. and Murayama, H. and Pierce, A. and Wells, J.D. Top Quark Forward-Backward Asymmetry From New t-channel Physics. *Phys.Rev.*, **D81**:015004, 2010.
- [116] Cheung, K. and Keung, W.Y. and Yuan, T.C. Top Quark Forward-Backward Asymmetry. *Phys.Lett.*, **B682**:287–290, 2009.
- [117] Shu, J. and Tait, T.M.P. and Wang, K. Explorations Of The Top Quark Forward-Backward Asymmetry At The Tevatron. *Phys.Rev.*, **D81**:034012, 2010.
- [118] Arhrib, A. and Benbrik, R. and Chen, C.H. Forward-Backward Asymmetry Of Top Quark In Diquark Models. *Phys.Rev.*, **D82**:034034, 2010.
- [119] Dorsner, I. and Fajfer, S. and Kamenik, J.F. and Kosnik, N. Light Colored Scalars From Grand Unification And The Forward-Backward Asymmetry In  $t\bar{t}$  Production. *Phys.Rev.*, **D81**:055009, 2010.
- [120] Barger, V. and Keung, W.Y. and Yu, C.T. Asymmetric Left-Right Model And The Top Pair Forward-Backward Asymmetry. *Phys.Rev.*, **D81**:113009, 2010.
- [121] Xiao, B. and Wang, Y.K. and Zhu, S.H. Forward-Backward Asymmetry And Differential Cross Section Of Top Quark In Flavor Violating  $Z'$  Model At  $\mathcal{O}(\alpha_s^2\alpha_X)$ . *Phys.Rev.*, **D82**:034026, 2010.
- [122] Cheung, K. and Yuan, T.C. Top Quark Forward-Backward Asymmetry In The Large Invariant Mass Region. *Phys.Rev.*, **D83**:074006, 2011.

- [123] Shelton, J. and Zurek, K. M. Maximal Flavor Violation From New Right-Handed Gauge Bosons. *Phys.Rev.*, **D83**:091701, 2011.
- [124] Berger, E.L. and Cao, Q.H. and Chen, C.R. and Li, C.S. and Zhang, H. Top Quark Forward-Backward Asymmetry And Same-Sign Top Quark Pairs. *Phys.Rev.Lett.*, **106**:201801, 2011.
- [125] Grinstein, B. and Kagan, A.L. and Trott, M. and Zupan, J. Forward-Backward Asymmetry In  $t\bar{t}$  Production From Flavour Symmetries. *Phys.Rev.Lett.*, **107**:012002, 2011.
- [126] Craig, N. and Kilic, C. and Strassler, M.J. LHC Charge Asymmetry As Constraint On Models For The Tevatron Top Anomaly. *arXiv*, hep-ph/(1103.2127), 2011.
- [127] Ligeti, Z. and Tavares, G.M. and Schmaltz, M. Explaining The  $t\bar{t}$  Forward-Backward Asymmetry Without Dijet Or Flavor Anomalies. *JHEP*, **1106**:109, 2011.
- [128] Jung, S. and Pierce, A. and Wells, J.D. Top Quark Asymmetry From A Non-Abelian Horizontal Symmetry. *Phys.Rev.*, **D83**:114039, 2011.
- [129] Nelson, A.E. and Okui, T. and Roy, T.S. A Unified, Flavor Symmetric Explanation For The  $t\bar{t}$  Asymmetry And  $W_{jj}$  Excess At CDF. *arXiv*, hep-ph/(1104.2030), 2011.
- [130] Babu, K.S. and Frank, M. and Rai, S.K. Top Quark Asymmetry And  $W_{jj}$  Excess At CDF From Gauged Flavor Symmetry. *Phys.Rev.Lett.*, **107**:061802, 2011.
- [131] Patel, K.M. and Sharma, P. Forward-Backward Asymmetry In Top Quark Production From Light Colored Scalars In SO(10) Model. *JHEP*, **1104**:085, 2011.
- [132] Duraisamy, M. and Rashed, A. and Datta, A. The Top Forward Backward Asymmetry With General  $Z'$  Couplings. *arXiv*, hep-ph/(1106.5982), 2011.
- [133] Sehgal, L.M. and Wanninger, M. Forward-Backward Asymmetry In Two Jet Events: Signature Of Axiguons In  $p\bar{p}$  Collisions. *Phys.Lett.*, **B200**:211, 1988.

- [134] Barcelo, R. and Carmona, A. and Masip, M. and Santiago, J. Gluon Excitations In  $t\bar{t}$  Production At Hadron Colliders. *Phys.Rev.*, **D84**:014024, 2011.
- [135] Barcelo, R. and Carmona, A. and Masip, M. and Santiago, J. Stealth Gluons At Hadron Colliders. *arXiv*, hep-ph/(1106.4054), 2011.
- [136] Bagger, J. and Schmidt, C. and King, S. Axigluon Production In Hadronic Collisions. *Phys.Rev.*, **D37**:1188, 1988.
- [137] Djouadi, A. and Moreau, G. and Richard, F. and Singh, R.K. The Forward-Backward Asymmetry Of Top Quark Production At The Tevatron In Warped Extra Dimensional Models. *Phys.Rev.*, **D82**:071702, 2010.
- [138] Ferrario, P. and Rodrigo, G. Constraining Heavy Colored Resonances From Top-Antitop Quark Events. *Phys.Rev.*, **D80**:051701, 2009.
- [139] Frampton, P.H. and Shu, J. and Wang, K. Axigluon As Possible Explanation For  $p\bar{p} \rightarrow t\bar{t}$  Forward-Backward Asymmetry. *Phys.Lett.*, **B683**:294–297, 2010.
- [140] Chivukula, R.S. and Simmons, E.H. and Yuan, C.P. Axigluons Cannot Explain The Observed Top Quark Forward-Backward Asymmetry. *Phys.Rev.*, **D82**:094009, 2010.
- [141] Bauer, M. and Goertz, F. and Haisch, U. and Pfoh, T. and Westhoff, S. Top-Quark Forward-Backward Asymmetry In Randall-Sundrum Models Beyond The Leading Order. *JHEP*, **1011**:039, 2010.
- [142] Chen, C.H. and Cvetic, G. and Kim, C.S. Forward-Backward Asymmetry Of Top Quark In Unparticle Physics. *Phys.Lett.*, **B694**:393–397, 2011.
- [143] Alvarez, E. and Da Rold, L. and Szyrkman, A. A Composite Higgs Model Analysis Of Forward-Backward Asymmetries In The Production Of Tops At Tevatron And Bottoms At LEP And SLC. *JHEP*, **1105**:070, 2011.
- [144] Delaunay, C. and Gedalia, O. and Lee, S.J. and Perez, G. and Ponton, E. Extraordinary Phenomenology From Warped Flavor Triviality. *arXiv*, hep-ph/(1101.2902), 2011.

- [145] Bai, Y. and Hewett, J.L. and Kaplan, J. and Rizzo, T.G. LHC Predictions From A Tevatron Anomaly In The Top Quark Forward-Backward Asymmetry. *JHEP*, **1103**:003, 2011.
- [146] Barreto, E.R. and Coutinho, Y.A. and Sa Borges, J. Top Quark Forward-Backward Asymmetry From The  $3 - 3 - 1$  Model. *Phys.Rev.*, **D83**:054006, 2011.
- [147] Foot, R. Top Quark Forward-Backward Asymmetry From  $SU(N_c)$  Color. *Phys.Rev.*, **D83**:114013, 2011.
- [148] Zerwekh, A.R. The Axigluon, A Four-Site Model And The Top Quark Forward-Backward Asymmetry At The Tevatron. *arXiv*, hep-ph/(1103.0956), 2011.
- [149] Shu, J. and Wang, K. and Zhu, G. A Revisit To Top Quark Forward-Backward Asymmetry. *arXiv*, hep-ph/(1104.0083), 2011.
- [150] Haisch, U. and Westhoff, S. Massive Color-Octet Bosons: Bounds On Effects In Top-Quark Pair Production. *arXiv*, hep-ph/(1106.0529), 2011.
- [151] Tavares, G.M. and Schmaltz, M. Explaining The  $t\bar{t}$  Asymmetry With A Light Axigluon. *arXiv*, hep-ph/(1107.0978), 2011.
- [152] Alvarez, E. and Da Rold, L. and Vietto, J.I.S. and Szykman, A. Phenomenology Of A Light Gluon Resonance In Top-Physics At Tevatron And LHC. *arXiv*, hep-ph/(1107.1473), 2011.
- [153] Aguilar-Saavedra, J.A. and Perez-Victoria, M. Shaping The Top Asymmetry. *arXiv*, hep-ph/(1107.2120), 2011.
- [154] Bauer, C.W. and Ligeti, Z. and Schmaltz, M. and Thaler, J. and Walker, D.G.E. Supermodels For Early LHC. *Phys.Lett.*, **B690**:280–288, 2010.
- [155] Arnold, J.M. and Pospelov, M. and Trott, M. and Wise, M.B. Scalar Representations And Minimal Flavor Violation. *JHEP*, **1001**:073, 2010.
- [156] Jung, D.W. and Ko, P. and Lee, J.S. and Nam, S.H. Model Independent Analysis Of The Forward-Backward Asymmetry Of Top Quark Production At The Tevatron. *Phys.Lett.*, **B691**:238–242, 2010.

- [157] Cao, J. and Heng, Z. and Wu, L. and Yang, J.M. Top Quark Forward-Backward Asymmetry At The Tevatron: A Comparative Study In Different New Physics Models. *Phys.Rev.*, **D81**:014016, 2010.
- [158] Cao, Q.H. and McKeen, D. and Rosner, J.L. and Shaughnessy, G. and Wagner, C.E.M. Forward-Backward Asymmetry Of Top Quark Pair Production. *Phys.Rev.*, **D81**:114004, 2010.
- [159] Jung, D.W. and Ko, P. and Lee, J.S. Longitudinal Top Polarization As A Probe Of A Possible Origin Of Forward-Backward Asymmetry Of The Top Quark At The Tevatron. *Phys.Lett.*, **B701**:248–254, 2011.
- [160] Choudhury, D. and Godbole, R.M. and Rindani, S.D. and Saha, P. Top Polarization, Forward-Backward Asymmetry And New Physics. *Phys.Rev.*, **D84**:014023, 2011.
- [161] Jung, D.W. and Ko, P. and Lee, J.S. and Nam, S.H. Model-Independent Analysis Of Forward-Backward Asymmetry Of Top Quark Production At The Tevatron. *arXiv*, hep-ph/(1012.0102), 2010.
- [162] Blum, K. and Delaunay, C. and Gedalia, O. and Hochberg, Y. and Lee, S.J. and Nir, Y. and Perez, G. and Soreq, Y. Implications Of The CDF  $t\bar{t}$  Forward-Backward Asymmetry For Boosted Top Physics. *Phys.Lett.*, **B702**:364–369, 2011.
- [163] Ahrens, V. and Ferroglia, A. and Neubert, M. and Pecjak, B.D. and Yang, L.L. RG-Improved Single-Particle Inclusive Cross Sections And Forward-Backward Asymmetry In  $t\bar{t}$  Production At Hadron Colliders. *arXiv*, hep-ph/(1103.0550), 2011.
- [164] Degrande, C. and Gerard, J.M. and Grojean, C. and Maltoni, F. and Servant, G. Non-Resonant New Physics In Top Pair Production At Hadron Colliders. *JHEP*, **1103**:125, 2011.
- [165] Degrande, C. and Gerard, J.M. and Grojean, C. and Maltoni, F. and Servant, G. An Effective Approach To Same Sign Top Pair Production At The LHC And The Forward-Backward Asymmetry At The Tevatron. *arXiv*, hep-ph/(1104.1798), 2011.

- [166] Delaunay, C. and Gedalia, O. and Hochberg, Y. and Perez, G. and Soreq, Y. Implications Of The CDF  $t\bar{t}$  Forward-Backward Asymmetry For Hard Top Physics. *JHEP*, **1108**:031, 2011.
- [167] Gresham, M.I. and Kim, I.W. and Zurek, K.M. On Models Of New Physics For The Tevatron Top  $A_{FB}$ . *Phys.Rev.*, **D83**:114027, 2011.
- [168] Diener, R. and Godfrey, S. and Martin, T.A.W. Unravelling An Extra Neutral Gauge Boson At The LHC Using Third Generation Fermions. *Phys.Rev.*, **D83**:115008, 2011.
- [169] Diener, R. and Godfrey, S. and Martin, T.A.W. Discovery And Identification Of Extra Neutral Gauge Bosons At The LHC. *arXiv*, hep-ph/(0910.1334), 2009.
- [170] Hewett, J.L. and Shelton, J. and Spannowsky, M. and Tait, T.M.P. and Takeuchi, M.  $A_{FB}^t$  Meets LHC. *arXiv*, hep-ph/(1103.4618), 2011.
- [171] Gresham, M.I. and Kim, I.W. and Zurek, K.M. Searching For Top Flavor Violating Resonances. *arXiv*, hep-ph/(1102.0018), 2011.
- [172] Aguilar-Saavedra, J.A. and Perez-Victoria, M. Probing The Tevatron  $t\bar{t}$  Asymmetry At LHC. *JHEP*, **1105**:034, 2011.
- [173] Aguilar-Saavedra, J.A. and Perez-Victoria, M. Asymmetries In  $t\bar{t}$  Production: LHC Versus Tevatron. *arXiv*, hep-ph/(1105.4606), 2011.
- [174] Ko, P. and Omura, Y. and Yu, C. Top Forward-Backward Asymmetry And The CDF  $W_{jj}$  Excess In Leptophobic  $U(1)'$  Flavor Models. *arXiv*, hep-ph/(1108.0350), 2011.
- [175] Gabrielli, E. and Raidal, M. Effective Axial-Vector Coupling Of Gluon As An Eexplanation To The Top Quark Asymmetry. *arXiv*, hep-ph/(1106.4553), 2011.
- [176] Blum, K. and Hochberg, Y. and Nir, Y. Scalar-Mediated  $t\bar{t}$  Forward-Backward Asymmetry. *arXiv*, hep-ph/(1107.4350), 2011.
- [177] Aad, G. and others (ATLAS Collaboration). Search For High Mass Dilepton Resonances In  $pp$  Collisions At  $\sqrt{s} = 7$  TeV With The ATLAS Experiment. *Phys.Lett.*, **B700**:163–180, 2011.

- [178] ATLAS Collaboration. Exotics Searches In Photon And Lepton Final States With The ATLAS Detector. <http://indico.in2p3.fr/contributionDisplay.py?contribId=846&sessionId=6&confId=5116>, 2011.
- [179] CMS Collaboration. Search For Resonances In The Dilepton Mass Distribution In  $pp$  Collisions At  $\sqrt{s} = 7$  TeV. <https://twiki.cern.ch/twiki/bin/view/CMSPublic/PhysicsResultsEXO/>, 2011.
- [180] Abazov, V.M. and others (DØ Collaboration). Search For A Heavy Neutral Gauge Boson In The Dielectron Channel With  $5.4 \text{ fb}^{-1}$  Of  $p\bar{p}$  Collisions At  $\sqrt{s} = 1.96$  TeV. *Phys.Lett.*, **B695**:88–94, 2011.
- [181] Nemevsek, M. and Nesti, F. and Senjanovic, G. and Zhang, Y. First Limits On Left-Right Symmetry Scale From LHC Data. *Phys.Rev.*, **D83**:115014, 2011.
- [182] Maiezza, A. and Nemevsek, M. and Nesti, F. and Senjanovic, G. Left-Right Symmetry At LHC. *Phys.Rev.*, **D82**:055022, 2010.
- [183] Tello, V. and Nemevsek, M. and Nesti, F. and Senjanovic, G. and Vissani, F. Left-Right Symmetry: From LHC To Neutrinoless Double Beta Decay. *Phys.Rev.Lett.*, **106**:151801, 2011.
- [184] Cacciari, M. and Frixione, S. and Mangano, M.L. and Nason, P. and Ridolfi, G. Updated Predictions For The Total Production Cross Sections Of Top And Of Heavier Quark Pairs At The Tevatron And At The LHC. *JHEP*, **0809**:127, 2008.
- [185] Kidonakis, N. and Vogt, R. The Theoretical Top Quark Cross Section At The Tevatron And The LHC. *Phys.Rev.*, **D78**:074005, 2008.
- [186] Moch, S. and Uwer, P. Heavy-Quark Pair Production At Two Loops In QCD. *Nucl.Phys.Proc.Suppl.*, **183**:75–80, 2008.
- [187] Gresham, M.I. and Kim, I.W. and Zurek, K.M. Tevatron Top  $A_{FB}$  vs LHC Top Physics. *arXiv*, hep-ph/(1107.4364), 2011.
- [188] Sjöstrand, T. and Mrenna, S. and Skands, P.Z. PYTHIA 6.4 Physics And Manual. *JHEP*, **0605**:026, 2006.



- [189] Conway, J. and Culbertson, R. and Demina, R. and Kilminster, B. and Kruse, M. and Mrenna, S. and Nielsen, J. and Roco, M. and Pierce, A. and Thaler, J and Wizansky, T. PGS4: Pretty Good Simulation Of High Energy Collisions. <http://physics.ucdavis.edu/~conway/research/software/pgs/pgs4-general.htm>, 2009.
- [190] CMS Collaboration. Measurement Of The Charge Asymmetry In Top Quark Pair Production With The CMS Experiment. <http://cdsweb.cern.ch/record/1335714/files/TOP-10-010-pas.pdf>, 2011.
- [191] ATLAS Collaboration. Measurement Of The Charge Asymmetry In Top Quark Pair Production In  $pp$  Collisions At  $\sqrt{s}=7$  TeV Using The ATLAS Detector. <http://cdsweb.cern.ch/record/1372916/files/ATLAS-CONF-2011-106.pdf>, 2011.
- [192] Zhou, Z.Q. and Xiao, B. and Wang, Y.K. and Zhu, S.H. Discriminating Different  $Z$ 's Via Asymmetries At The LHC. *Phys.Rev.*, **D83**:094022, 2011.
- [193] Aad, Georges and others (ATLAS Collaboration). Measurement Of The Top Quark Pair Production Cross Section With ATLAS In  $pp$  Collisions At  $\sqrt{s} = 7$  TeV. *Eur.Phys.J.*, **C71**:1577, 2011.
- [194] Altunkaynak, B. and Holmes, M. and Nath, P. and Nelson, B.D. and Peim, G. SUSY Discovery Potential And Benchmarks For Early Runs At  $\sqrt{s} = 7$  TeV At The LHC. *Phys.Rev.*, **D82**:115001, 2010.
- [195] Aguilar-Saavedra, J.A. and Perez-Victoria, M. Simple Models For The Top Asymmetry: Constraints And Predictions. *arXiv*, hep-ph/(1107.0841), 2011.
- [196] Frank, M. and Hayreter, A. and Turan, I. Top Quark Pair Production And Asymmetry At The Tevatron And LHC In Left-Right Models. *arXiv*, hep-ph/(1108.0998), 2011.